

# Sensor Array Processing with Manifold Uncertainty

by

Jonathan L. Odom

Department of Electrical and Computer Engineering  
Duke University

Date: \_\_\_\_\_

Approved:

\_\_\_\_\_  
Jeffrey Krolik, Supervisor

\_\_\_\_\_  
Loren Nolte

\_\_\_\_\_  
Matthew Reynolds

\_\_\_\_\_  
Rebecca Willett

\_\_\_\_\_  
Donald Bliss

\_\_\_\_\_  
Galen Reeves

Dissertation submitted in partial fulfillment of the requirements for the degree of  
Doctor of Philosophy in the Department of Electrical and Computer Engineering  
in the Graduate School of Duke University

2013

ABSTRACT

Sensor Array Processing with Manifold Uncertainty

by

Jonathan L. Odom

Department of Electrical and Computer Engineering  
Duke University

Date: \_\_\_\_\_

Approved:

\_\_\_\_\_  
Jeffrey Krolik, Supervisor

\_\_\_\_\_  
Loren Nolte

\_\_\_\_\_  
Matthew Reynolds

\_\_\_\_\_  
Rebecca Willett

\_\_\_\_\_  
Donald Bliss

\_\_\_\_\_  
Galen Reeves

An abstract of a dissertation submitted in partial fulfillment of the requirements for  
the degree of Doctor of Philosophy in the Department of Electrical and Computer  
Engineering  
in the Graduate School of Duke University  
2013

Copyright © 2013 by Jonathan L. Odom  
All rights reserved except the rights granted by the  
Creative Commons Attribution-Noncommercial Licence

# Abstract

The spatial spectrum, also known as a field directionality map, is a description of the spatial distribution of energy in a wavefield. By sampling the wavefield at discrete locations in space, an estimate of the spatial spectrum can be derived using basic wave propagation models. The observable data space corresponding to physically realizable source locations for a given array configuration is referred to as the array manifold. In this thesis, array manifold ambiguities for linear arrays of omni-directional sensors in non-dispersive fields are considered.

First, the problem of underwater a hydrophone array towed behind a maneuvering platform is considered. The array consists of many hydrophones mounted to a flexible cable that is pulled behind a ship. The towed cable will bend or distort as the ship performs maneuvers. The motion of the cable through the turn can be used to resolve ambiguities that are inherent to nominally linear arrays. The first significant contribution is a method to estimate the spatial spectrum using a time-varying array shape in a dynamic field and broadband temporal data. Knowledge of the temporal spectral shape is shown to enhance detection performance. The field is approximated as a sum of uncorrelated planewaves located at uniform locations in angle, forming a gridded map on which a maximum likelihood estimate for broadband source power is derived. Uniform linear arrays also suffer from spatial aliasing when the inter-element spacing exceeds a half-wavelength. Broadband temporal knowledge is shown to significantly reduce aliasing and thus, in simulation, enhance target detection in

interference dominated environments.

As an extension, the problem of towed array shape estimation is considered when the number and location of sources are unknown. A maximum likelihood estimate of the array shape using the field directionality map is derived. An acoustic-based array shape estimate that exploits the full  $360^\circ$  field via field directionality mapping is the second significant contribution. Towed hydrophone arrays have heading sensors in order to estimate array shape, but these sensors can malfunction during sharp turns. An array shape model is described that allows the heading sensor data to be statistically fused with heading sensor. The third significant contribution is method to exploit dynamical motion models for sharp turns for a robust array shape estimate that combines acoustic and heading data. The proposed array shape model works well for both acoustic and heading data and is valid for arbitrary continuous array shapes.

Finally, the problem of array manifold ambiguities for static under-sampled linear arrays is considered. Under-sampled arrays are non-uniformly sampled with average spacing greater than a half-wavelength. While spatial aliasing only occurs in uniformly sampled arrays with spacing greater than a half-wavelength, under-sampled arrays have increased spatial resolution at the cost of high sidelobes compared to half-wavelength sampled arrays with the same number of sensors. Additionally, non-uniformly sampled arrays suffer from rank deficient array manifolds that cause traditional subspace based techniques to fail. A class of fully augmentable arrays, minimally redundant linear arrays, is considered where the received data statistics of a uniformly spaced array of the same length can be reconstructed in wide sense stationary fields at the cost of increased variance. The fourth significant contribution is a reduced rank processing method for fully augmentable arrays to reduce the variance from augmentation with limited snapshots. Array gain for reduced rank adaptive processing with diagonal loading for snapshot deficient scenarios is analytically de-

rived using asymptotic results from random matrix theory for a set ratio of sensors to snapshots. Additionally, the problem of near-field sources is considered and a method to reduce the variance from augmentation is proposed. In simulation, these methods result in significant average and median array gains with limited snapshots.

to Ashley

# Contents

<b>Abstract</b>	<b>iv</b>
<b>List of Figures</b>	<b>xi</b>
<b>List of Abbreviations and Symbols</b>	<b>xiv</b>
<b>Acknowledgements</b>	<b>xvii</b>
<b>1 Introduction</b>	<b>1</b>
<b>2 Passive Array Processing with Dynamic Arrays</b>	<b>5</b>
2.1 Source Parameter Estimation . . . . .	6
2.1.1 Synthetic Aperture Sonar . . . . .	8
2.1.2 Adaptive Beamforming . . . . .	9
2.1.3 Statistical Estimation Techniques . . . . .	11
2.2 Towed Array Shape Estimation . . . . .	14
2.3 Horizontal Ambient Ocean Noise . . . . .	17
2.4 Joint Array/Source Parameter Estimation . . . . .	18
2.4.1 Conditional Maximum Likelihood . . . . .	19
2.4.2 Unconditional Maximum Likelihood . . . . .	21
<b>3 Data Model</b>	<b>23</b>
3.1 Signal Model . . . . .	24
3.2 Water Pulley Array Shape Model . . . . .	26
3.3 Non-linear Array Shape Model . . . . .	29

<b>4</b>	<b>Spatial Spectrum and Array Parameter Estimators</b>	<b>33</b>
4.1	Narrowband Spatial Spectrum Estimators . . . . .	34
4.1.1	Derivative Based Maximum Likelihood: DBML . . . . .	35
4.1.2	Recursive Bayes Maximum Likelihood: RBML . . . . .	38
4.2	Narrowband Simulation . . . . .	42
4.3	Broadband Spatial Spectrum Estimator with Parameter Reduction . . . . .	46
4.4	Broadband Simulation with Under-sampled Array . . . . .	51
4.5	Water Pulley Model with Heading Sensor Constraints . . . . .	56
4.5.1	Water Pulley Model Acoustic Estimate . . . . .	57
4.5.2	Non-statistical Acoustic and Heading Sensor Fusion . . . . .	60
4.6	Non-linear Model with Statistical Heading Sensor Fusion . . . . .	64
4.6.1	Parametric Array Shape Approximation . . . . .	65
4.6.2	Acoustic Based Array Shape Estimate . . . . .	67
4.6.3	Performance Bounds . . . . .	71
4.6.4	Simulation Results . . . . .	74
4.7	Conclusion . . . . .	80
<b>5</b>	<b>Under-sampled Arrays with Limited Data</b>	<b>82</b>
5.1	Mathematical Background . . . . .	83
5.1.1	Uniform Linear Arrays . . . . .	84
5.1.2	Non-uniform Linear Arrays . . . . .	86
5.1.3	Array Manifold Ambiguity and Identifiability . . . . .	88
5.1.4	Exploiting the Co-array . . . . .	90
5.1.5	Source Detection with a NLA . . . . .	93
5.2	Geometric Interpretation . . . . .	95
5.3	Near-field Sources and Snapshot Deficient Processing . . . . .	97

5.4	Far-field and Near-field Received Signal Model . . . . .	99
5.5	Covariance Matrix Augmentation . . . . .	100
5.6	Reduced Rank Adaptive Beamforming . . . . .	104
5.7	Simulation Results . . . . .	110
5.8	Conclusion . . . . .	118
<b>6</b>	<b>Concluding Remarks</b>	<b>120</b>
<b>A</b>	<b>Second Order Expectation Approximation</b>	<b>126</b>
<b>B</b>	<b>Cramér-Rao Bounds</b>	<b>128</b>
<b>C</b>	<b>Derivations for Asymptotic Performance Results</b>	<b>130</b>
C.1	Relevant Results from Random Matrix Theory . . . . .	130
C.2	Simplification of (5.49) and (5.52) . . . . .	131
	<b>Bibliography</b>	<b>132</b>
	<b>Biography</b>	<b>142</b>

# List of Figures

2.1	Wavenumber and sensor vectors . . . . .	6
2.2	Conical angle . . . . .	8
2.3	Traditional physical model of towed array . . . . .	15
3.1	Polar coordinate system . . . . .	24
3.2	Singular value spectrum of array heading . . . . .	28
3.3	Array heading modes . . . . .	29
3.4	Arbitrary array shape parameterization . . . . .	30
4.1	Illustrative BTR . . . . .	43
4.2	BTR showing power estimates, in dB, from narrowband conventional beamformer output for clairvoyant circular array. . . . .	44
4.3	BTR showing narrowband power estimates, in dB, with a maneuvering short array using (a) conventional beamforming, (b) DBML estimate, and (c) RBML estimate. . . . .	46
4.4	Cramér-Rao bounds of power estimate . . . . .	49
4.5	Cramér-Rao bounds of power estimate with aliasing . . . . .	49
4.6	BTR showing power estimates, in dB, from broadband conventional beamformer output for under-sampled clairvoyant circular array. . . . .	52
4.7	BTRs showing broadband power estimates, in dB, with an under-sampled maneuvering short array using (a) conventional beamforming, (b) full ML, and (c) reduced ML. . . . .	53
4.8	Broadband BTR demonstrating the performance of the reduced ML technique in the presence of surface wave noise. . . . .	54

4.9	Broadband BTR using the reduced ML method with mismatched source signals. True source bandwidth 20% of assumed band. . . . .	55
4.10	ROC curve with target SNR -25 dB using $\tilde{M}$ -of- $\tilde{N}$ detector for under-sampled array . . . . .	56
4.11	Source and array track for simulation . . . . .	59
4.12	Sensor heading estimate with known source directions . . . . .	59
4.13	ME for array position estimate with known source directions . . . . .	60
4.14	Block diagram of ML-FDM array shape estimate . . . . .	60
4.15	Block diagram of ML-DOA algorithm . . . . .	61
4.16	ME for array position estimate with unknown source directions . . . . .	62
4.17	Source and array track for second simulation . . . . .	63
4.18	Array heading estimate for sensor 15 . . . . .	64
4.19	Empirical cumulative distribution function of RMSE of array shape . . . . .	64
4.20	Block diagram of acoustic and heading data fusion . . . . .	68
4.21	CRLB of array curvature for a small number of sources . . . . .	73
4.22	CRLB of array curvature for many sources . . . . .	74
4.23	Headings at head and tail of the tow cable during maneuver . . . . .	75
4.24	Acoustic based array shape estimates . . . . .	76
4.25	Filtered array shape estimates . . . . .	77
4.26	RMSE of hydrophone heading with four sources . . . . .	78
4.27	CDF of array position error . . . . .	79
4.28	RMSE of hydrophone headings along array . . . . .	80
5.1	Relationship between physical vectors and array manifold vectors . . . . .	96
5.2	Illustrative examples of array manifold ambiguities . . . . .	96
5.3	Example scenario of near-field target in far-field interference . . . . .	99
5.4	Array element positions for the MRLA and equivalent ULA . . . . .	110

5.5	Co-array for 20 element MRLA . . . . .	110
5.6	Near-field beamforming output with known covariance . . . . .	111
5.7	Average array gain with single far-field interferer and far-field source .	113
5.8	Average array gain with 30 far-field interferers and far-field source . .	114
5.9	Average array gain with single far-field interferer and near-field source	115
5.10	Average array gain with 30 far-field interferers and near-field source .	116
5.11	CDF of array gain with 1 far-field interferer and near-field source . .	117
5.12	CDF of array gain with 30 far-field interferers and near-field source .	118

# List of Abbreviations and Symbols

## Symbols

In mathematical notation, a scalar will be denoted by italics,  $x$ . Special scalars that denote dimension sizes are often given by capital letters,  $X$  and indexed by  $x$ . Column vectors are given in lower-case bold,  $\mathbf{x}$ . Matrices are given by capital, bold letters,  $\mathbf{X}$ . Indices are given outside of brackets such that the  $2 \times 1$  vector is given by  $\mathbf{x} = [x_1 \ x_2]^T$  and  $[\mathbf{x}]_1 = x_1$ . Matrix or vector transposes are given by  $^T$  and conjugate (\*) transpose is denoted by  $^H$ . Statistical distributions and sets are given by calligraphic letters;  $\mathcal{CN}$  is the complex normal distribution, often assumed to be circularly symmetric. The following symbols are used throughout the document and are given alphabetically in English then Greek.

$\mathcal{A}$	Array manifold, curve in $M$ dimensional complex space
$\mathbf{A}(n, \omega)$	Acoustic array manifold matrix of size number of acoustic sensors ( $M$ ) by sources
$\mathbf{B}$	Basis set for water pulley approximation
$\mathfrak{C}^M$	$M$ dimensional complex space
$c$	Speed of propagation
$d$	Arc length along array
$\mathbf{d}$	Vector of locations along $d$
$\mathbf{D}_s$	Spatial derivative
$e, \exp$	Exponential function

$\mathbf{F}$	Kalman filter state transition matrix
$\mathbf{I}_x$	Identity matrix (of size $x$ when not implied)
$\mathcal{I}(x)$	Imaginary component of $x$
$j$	Imaginary number, $\sqrt{-1}$
$\mathbf{k}$	Wavenumber vector of size $3 \times 1$
$L$	Length of the array
$M$	Number of acoustic sensors of an array
$N$	Number of acoustic snapshots
$Q$	Number of grid points (or true sources) in bearing
$\mathcal{R}(x)$	Real component of $x$
$\mathbf{R}$	Received acoustic data covariance matrix
$\mathbf{s}$	Source acoustic signal
$t$	Time
$v$	Velocity
$\mathbf{u}$	Tow ship forcing function for linear water pulley model
$\mathbf{V}(n, \omega)$	Steering matrix of size $M \times Q$ .
$\mathbf{x}(n, \omega)$	Acoustic data of size $M \times 1$ from time $n$ and frequency $\omega$
$x, y, z$	Spatial dimensions
$\psi$	Array heading in bearing
$\gamma$	Basis parameters for water pulley approximation
$\delta(a, b)$	Delta function where $\delta(a, b) = 1$ when $a = b$ else $\delta(a, b) = 0$
$\Delta$	Generic discretization
$\Delta_t, \Delta_d$	Temporal discretization and spatial discretization respectively
$\boldsymbol{\eta}$	Acoustic non-directional noise vector of size $M \times 1$
$\boldsymbol{\epsilon}$	Array heading noise
$\theta$	Bearing angle of a source

$\rho$	Stiffness of array for water-pulley model
$\Sigma$	Acoustic source signal covariance matrix where the diagonal terms are source signal power as received by a single element
$\sigma^2$	Variance
$\phi$	Elevation angle
$\omega$	Temporal frequency

## Abbreviations

CML	Conditional Maximum Likelihood
CSM	Coherent Subspace Method
DMR	Dominate Mode Rejection
EM	Expectation Maximization
FFT	Fast Fourier Transform
MAP	Maximum A Posteriori
ML	Maximum Likelihood
MRLA	Minimally Redundant Linear Array
MVDR	Minimum Variance Distortionless Response
NLA	Non-uniform Linear Array
STCM	Steered Covariance Matrix
ULA	Uniform Linear Array
UML	Unconditional Maximum Likelihood

# Acknowledgements

I'd like to acknowledge the entire Electrical and Computer Engineering Department at Duke. This document ends my third degree in a department full of faculty and staff members that have consistently pushed me beyond my own expectations. Specifically, I'd like to thank Jeff Krolik, who introduced me to array signal processing and has been advising my research for the past six years. Thanks to my committee members for suffering through my exams, some of them for multiple degrees, and providing insightful feedback each time. Matt Reynolds and Loren Nolte have been immensely helpful and served on all three of my committees. I'd also like to thank Lisa Huettel who introduced me to the world of digital signal processing and, together with Kip Coonley, made the problems interesting. All of my research has been funded through numerous grants from ONR Code 321 under the direction of John Tague. Also, thanks to Bruce Newhall and various members of The Johns Hopkins Applied Physics Laboratory who helped me understand modern problems in underwater acoustics. Partial funding for travel was also provided by the IEEE Oceanic Engineering Society, Duke Graduate School, and Duke ECE Department.

The various members of Jeff Krolik's SAM lab at Duke that have helped me significantly along the way are: Vito, Ryan, Jeff, William, Jason, and Li. While only Jeff Rogers appeared as a collaborator on any of my papers, all of these previous students taught me the ideas you can't find in a book (or lent me the book when you can) and showed me how to survive graduate school.

Of course, I would have never ended up at Duke without the support of my family. Thanks to my parents for ensuring I understood the importance of education. Finally, special thanks to my wife, Ashley, for supporting me during my never-ending time at Duke. She has proofread and listened to so many of my introductions that she recognizes the names of all of the *important* array processing authors.

# 1

## Introduction

Sensor array processing refers to the use of a multichannel sampling scheme where data is statistically correlated between sampling channels. The broad range of applications includes sonar, radar, radio astronomy, and medical diagnosis. The common goal is to extract useful information by exploiting correlation between channels. The focus of the work presented here is to apply physical knowledge of the environment to detect remote objects and estimate relevant properties, such as location. In some scenarios, due to tactical requirements or power-constraints, detection and estimation must be performed without transmitting signals into the environment. In this case, signals generated by objects already in the environment can be exploited. Passive sonar is the primary application considered in this work; however, some techniques developed for passive processing can be applied to the active case. For passive sonar, common underwater acoustic sources are calls from marine mammals or the mechanical noise generated from the engine or propulsion system in a naval vessel. A tool used for situational awareness in underwater environments is a map of sources as a function of direction, referred to as the spatial spectrum.

Similar to a temporal spectrum that provides a depiction of temporal frequency

content, the spatial spectrum describes spatial frequency content. In simple propagation environments, the spatial frequency is directly related to the direction of the emitting source. Spatial spectrum estimation is used to determine received source power as a function of arrival direction; it is also referred to as field directionality mapping in acoustics. This estimate is used for detection, localization and classification of objects and may be used as the input for other algorithms. Here the spatial spectrum is estimated using signals collected by an array, where an array refers to a set of sensors with a common phase reference. In this work, each sensor is assumed to have identical omni-directional characteristics and located at unique points in space. Spatial spectrum estimates can sometimes be improved by using several distributed arrays, without a common phase reference between arrays.

Traditionally, array processing methods assume array parameters are known and estimate source parameters, such as location. Assuming sources are in the far-field, source location is modeled through direction of arrival, or source bearing. At first, a free-space model is considered where the signal from a particular source depends on the location of source and array sensors, assuming the local environment is homogeneous and non-dispersive. The vector describing propagation across the array is referred to as the array manifold vector, where the array manifold is the set all possible array manifold vectors. Array manifolds for linear arrays with omni-directional sensors have an ambiguity that occurs at all bearings  $\pm 180^\circ$  in the 2-D plane over  $360^\circ$ , known as the left/right ambiguity. The perceived source direction may also be uncertain for other reasons, such as unknown array shape or spatial aliasing. For example, towed sonar arrays are built from long flexible cables and pulled underwater behind a tow platform. Because the exact motion of the cable is unknown, the array shape must be estimated. Since the source locations and array shape are both unknown, a joint estimation problem is formed. Note that non-physics based approaches (e.g. blind beamforming) offer a solution to this problem by avoiding

array shape estimation and source localization in favor of source signal separation without direction of arrival estimation. A physics based approach is used in this work because the array shape estimate alone is of interest for many subsequent processing techniques, such as beamforming and location-aided source classification. Unknown array shape is the second type of manifold uncertainty considered. Another instance of uncertainty is caused by spatial aliasing, which is analogous to temporal aliasing. When omni-directional sensors are uniformly spaced with an inter-element spacing greater than a half wavelength, several different locations have identical propagation vectors across the array. The ambiguity can be reduced by using multiple array orientations or knowledge of the temporal spectrum. A towed array will change orientations as the platform makes turns allowing disambiguation over  $360^\circ$ .

Towed array platforms have on-board positioning systems to account for small variations of a nominally linear shape as well as provide global reference points. Heading sensors provide raw data for these systems by determining the global (i.e. from North) heading of segments along the array. While significant work has been published on exploiting dynamical motion models with heading sensors, little research has focused on fusing towed array data with heading sensors. Heading sensors provide accurate, reliable shape data under straight towing conditions but suffer major performance degradation during sharp turns or other fast maneuvers. The fusion of acoustic and heading data can improve shape estimation performance in these conditions, allowing traditional physics based array processing techniques to be subsequently used. Unfortunately, an additional problem for adaptive processing techniques occurs due to the changing array shape. During maneuvers, the amount of data where the field appears to be relatively static is limited. This also holds for static arrays in a time-varying environment. Data dependent, or adaptive, array processing traditionally assumes the data is independent and identically distributed across time. The algorithms in the first half of this document consider the case where

the array changes shape and sources move.

The second half of the document addresses the case of known non-uniformly spaced linear arrays with limited data. The number of data samples that are identically distributed is assumed to be limited by source motion. In this case, the array is assumed known but array manifold uncertainty exists through spatial under-sampling. This is a generalization of aliasing, which requires uniform sampling, where the array is non-uniformly spaced such that the average spacing exceeds half of a wavelength. Using the spatial invariance of homogeneous or wide sense stationary fields, fully augmentable arrays guarantee an array manifold can be formed using covariance matrix augmentation. However, this operation results in increased variance of spatial spectrum estimates. Methods to reduce the variance are proposed and the case of a near-field source, which is not wide sense stationary, is considered.

An outline of the rest of the document is given as follows. First, spatial spectrum estimation in the context of towed arrays is described. The literature on array processing for towed arrays is discussed in Chapter 2, including the problem of jointly estimating the array shape and spatial spectrum. The received data model for frequency domain signals is given in Chapter 3. Towed array shape estimation using spatial spectrum estimation is presented in Chapter 4. Fully augmentable arrays with limited snapshot support is considered in Chapter 5. A final discussion of completed and future work is given in Chapter 6

## Passive Array Processing with Dynamic Arrays

In passive sonar, spatial spectrum estimation and source localization are used for situational awareness. The spatial spectrum, or field directionality map, describes received signal power as a function of arrival direction. A typical sonar representation of the environment is a bearing-time-record (BTR) plot, where power as function of bearing is recorded over time. This map is often used for tactical decisions or as the input to target tracking algorithms. This section provides an overview of source and array parameters that can be estimated using physics-based models.

Historically, array processing literature has focused on estimating source parameters, such as location and frequency, assuming the array parameters are known. Following a review of these fundamental array processing concepts, the case of a maneuvering array (or equivalently multiple arrays with different orientations) is considered. The uncertainty of array parameters is studied through sensitivity analysis [1], and the underwater array literature focuses on parametric forms of nominally linear arrays [2]. Consider the wave propagation model for a single source given by (2.1) as a function of frequency  $\omega$ , wavenumber  $\mathbf{k}$ , and sensor location  $\mathbf{r}$ . Vectors are denoted in bold and transpose is given by  $^T$ . In this model, the phase delay between sensors

is a function of source/sensor location. A physical representation of the vectors is shown in Figure 2.1. Sensors and sources are assumed to be omnidirectional.

$$x(\mathbf{r}, t) = se^{j(\omega t - \mathbf{k}^T(t)\mathbf{r}(t))} \quad (2.1)$$

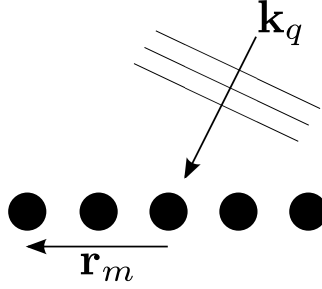


FIGURE 2.1: Wavenumber and sensor vectors

## 2.1 Source Parameter Estimation

A straight forward approach to spatial spectrum estimation is conventional, or delay-and-sum, beamforming. In sonar literature this is also referred to as Bartlett beamforming. Beamforming is a spatial filter analogous to FIR temporal filtering [3], which defined as a weighted summation of the input with weights  $\mathbf{w}$  and received data  $\mathbf{x}$ , as shown by

$$y = \mathbf{w}^H \mathbf{x}. \quad (2.2)$$

The far-field assumption used in (2.1) implies that the range from the source to the receiver is much larger than the total length of an array aperture. This results in a planewave where the wavefront is perpendicular to the source direction, as can be seen in Figure 2.1. The environment is assumed to be static over an observation period  $T$ , known as a snapshot and indexed by time frame  $n$ . This approximates source parameters,  $\mathbf{k}(t) \approx \mathbf{k}(n)$ , and receiver parameters,  $\mathbf{r}(t) \approx \mathbf{r}(n)$ . The time-domain received data is assumed to be converted to baseband frequency domain data. When

the time-bandwidth product,  $T \times BW$ , is larger than 16 [4], each frequency bin can be processed (statistically) independently. Note that  $T$  must also be longer than the maximum time it takes for the wavefront to travel across the array. The alternative narrowband assumption is  $T \times BW \ll 1$  and results in a similar narrowband model (see [5, pp. 332–369]). Note that in general, motion causes a Doppler shift in the received data but is ignored in passive processing when the source signal is an unknown waveform, e.g.  $s$  is zero mean and normally distributed.

The signal vector for a sequence of array locations,  $[\mathbf{r}_1 \ \mathbf{r}_2 \ \cdots \ \mathbf{r}_M]$ , is a function of  $\mathbf{k}$  where each element of the vector is given by (2.1). The source signal,  $s$ , is a function of the source level and is assumed unknown. In the absence of source level knowledge in a far-field environment, phase across the array is used to discriminate sources at different locations. This vector of phases forms an array manifold vector. The locus of all possible vectors, or points in  $M$  dimensional space, is referred to as the array manifold, which is the focus of Chapter 5. Linear arrays with constant inter-element spacing, known as uniform linear arrays (ULAs), are common because conventional beamforming can be implemented with a FFT when all sources are in the far-field. In general however, linear arrays have array manifold ambiguities due to the physical array geometry and are unable to differentiate between sources at locations symmetric across the array. With a towed array in the x-y plane, this is called left/right ambiguity. In three dimensions, this is a conical angle where the ambiguity forms a cone with constant angle measured from the array, shown in Figure 2.2. For linear arrays, the array manifold vectors are equal for all locations on the boundary of the cone. This occurs for omni-directional sensors in a far-field environment with no prior knowledge on source bearing.

Maneuvering the array by turning the tow platform is used to disambiguate sources on the cone. Wagstaff demonstrated the ability of a towed array to reduce ambiguities in a spatial spectrum estimate by maneuvering the array in a static

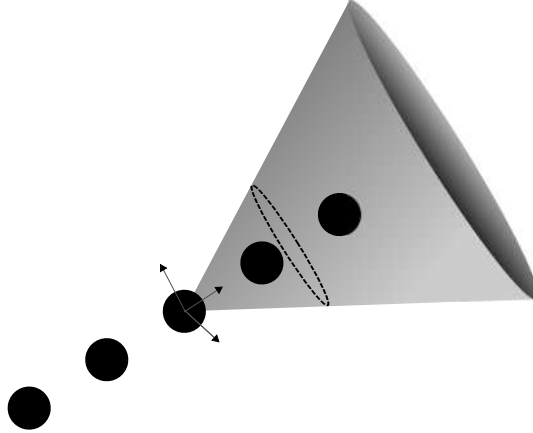


FIGURE 2.2: Conical angle

environment. A key insight by Wagstaff was the inclusion of the array beam pattern in the estimate [6]. When an array maneuvers faster than a source bearing changes, the ambiguous source locations vary while the true source bearing remains constant. Several methods to utilize a moving array are given in the following sections.

### 2.1.1 Synthetic Aperture Sonar

When the received source signal is coherent for multiple snapshots across time, a large virtual array can be formed. Coherency requires a stable phase between measurements, which is statistically interpreted as non-zero covariance between signals received at different locations. This is shown in (2.3), where each  $\mathbf{R}_{ab}$  refers to the expectation of the outer product of the data received at location  $a$  and  $b$ . Synthetic aperture sonar forms a virtual array for increased bearing resolution, original proposed by Yen and Carey to increase bearing resolution [7]. Creating the virtual array populates the covariance  $\mathbf{R}$ . The Doppler shift from source motion as well as the phase shift from array motion are used for beamforming in this case. The parameters can be estimated using data alone for linear motion [8]. The work has been extended to the broadband case for short arrays [9]. The size of the synthetic aperture is limited by the total distance over which a coherent virtual array can be formed. By

the nature of using a virtual array, the dimensionality of the data is increased. However, the total number of data points available in the larger space is reduced given the same sampling rate of a larger array with the same observation time. Synthetic aperture sonar is limited by model mismatch because the source is assumed to have a constant phase across space/time during the observation. Conventional techniques are used in this case as adaptive techniques are sensitive to model mismatch and require more snapshots [10]. Therefore, a synthetic aperture can be used to extend the localization accuracy and resolution of non-adaptive methods.

$$\mathbf{R} = \begin{bmatrix} \mathbf{R}_{11} & \mathbf{R}_{12} \\ \mathbf{R}_{21} & \mathbf{R}_{22} \end{bmatrix} \quad (2.3)$$

### 2.1.2 Adaptive Beamforming

In the presence of loud interfering sources and a weak target source, detection and estimation performance is limited by interference suppression. Interference is defined as undesirable signals from point or distributed sources. Capon developed an adaptive, or data-dependent, beamforming method known as minimum variance distortionless response (MVDR) beamforming [11]. The weights ensure unity gain in the steering direction and minimum power from other directions,

$$\mathbf{w} = \frac{\mathbf{R}^{-1}\mathbf{a}}{\mathbf{a}^H\mathbf{R}^{-1}\mathbf{a}} \quad (2.4)$$

where the covariance of the received data is  $\mathbf{R} = E[\mathbf{x}\mathbf{x}^H]$  assuming  $\mathbf{x}$  is zero mean and  $\mathbf{a}$  is a function of direction. MVDR beamformer weights for a signal in a given direction have been derived using mean square error, signal-to-noise ratio, and maximum likelihood; each solution differs by only a scaling factor [12, p. 89]. This formulation assumes the received data is (for a given time frame) wide sense stationary, but this not true over the course of an entire maneuver such as a turn. The assumption also does not hold as sources move in bearing. The spatial method devel-

oped by Wagstaff combines data incoherently from different directions and reduces non-stationary signals via averaging [6]. The method estimates the stationary field using the beampattern of the array at each location. Phase information between array locations is not used.

Several methods have been developed that preserve phase information but do not increase the data dimensionality. Wagstaff’s ad-hoc method demonstrated the possibility of improvement using beampattern knowledge. The Cramér-Rao bound for this problem was derived by Zeira and Friedlander [13]. The bound on source parameters, such as location, can be lowered by the changing array shape and orientation. In subsequent work, an eigenstructure-based technique was introduced using focusing matrices to form a time-invariant covariance matrix estimate [14]. This work was based on frequency domain focusing matrices by Wang and Kaveh [15], known as coherent signal-subspace methods (CSM). A linear transformation matrix,  $\mathbf{T}$ , is used to align the covariance matrix given by

$$\mathbf{R}_{\text{CSM}} = \sum_{b=1}^B \mathbf{T}(\omega_b) \mathbf{R}(\omega_b) \mathbf{T}^H(\omega_b). \quad (2.5)$$

The choice of  $\mathbf{T}$  requires source location estimates and is only valid near the estimates. A more computationally intensive method developed by Krolik and Swingler uses source bearing as a parameter [16]. This approach, shown in (2.6), steers to each direction instead of assuming all directions can be captured by the same transformation.

$$\mathbf{R}_{\text{STCM}}(\theta) = \sum_{b=1}^B \mathbf{T}(\omega_b, \theta) \mathbf{R}(\omega_b) \mathbf{T}^H(\omega_b, \theta) \quad (2.6)$$

This solution was extended for towed arrays by Zeira and Friedlander, with a summation over array position instead of frequency [14]. Adaptive methods, such as MVDR, are applied using the time-invariant covariance matrix estimate.

Historically, towed array data collected during sharp turns has not been used for beamforming. This is because the array shape is unknown and assuming a linear shape reduces performance [2]. More recent work using tow ship GPS data and tow heading sensors for array shape estimation in order to form adaptive beamforming weights during a turn. Gerstoft *et al.* demonstrated MVDR beamforming weights with experimental data [17]. In order to have enough snapshots for covariance matrix inversion, neighboring frequency bins were used. Greening and Perkins [18] implemented an algorithm highly related to Zeira and Friedlander’s work [14], but provided experimental results. The preliminary results using an MVDR beamformer showed the ability of focusing matrices to work with real data. Additionally, it has been shown to be beneficial to break the array into sub-arrays during turns [19] when the full array shape is unknown. The problems that limit adaptive beamforming are the unknown array shape and the limited number of snapshots for identically distributed data.

### 2.1.3 Statistical Estimation Techniques

Instead of beamforming, the spatial spectrum can be estimated directly using statistical estimation techniques. The two types of estimators considered are maximum likelihood (ML) and maximum a posterior (MAP). Each method requires finding the maximum of a probability density function (pdf) using a parametric signal model and received data. The ML estimate uses no a priori knowledge of the density parameters while the MAP estimate uses a density for each parameter. Note that ML estimate of source power (or waveform) when the array manifold vector is known is given by the output of the MVDR beamformer, with weights (2.4) [5, p. 443].

Assuming a narrowband, far-field propagation model, the unknown source parameters are source power level and direction of arrival. The problem can be formulated as a covariance matrix estimation problem, since all sources are assumed to be zero

mean, where the direction of arrival for all sources must also be jointly estimated. The spatial spectrum can be defined as the covariance matrix of the source signals across bearing [20], where the diagonal of the covariance matrix represents the power of each source. Additionally, the received data covariance matrix is a function of the spatial spectrum. Limiting the covariance matrix to a particular structure is a powerful concept. Structured covariance estimation is typically attributed to Burg *et. al.* [21], while the array processing ML formulation is credited to Böhme [22]. Closed-form solutions for source power levels, or direction of arrival, are not available given only received array data for arbitrary array shapes. Numerical techniques were first solved for small, known number of sources using an expectation-maximization (EM) approach. The EM algorithm is used for ML estimates when the parameters can be separated into incomplete (observable) data and complete (unobservable) data [23]. The complete data must be a function of the incomplete data. Feder and Weinstein were the first to propose an EM algorithm for parametrized array signal models [24]. Miller and Fuhrmann extended the work to include stochastic narrowband signals and jointly estimated the direction of arrival and source signal [25]. The broadband case was considered by Chung and Böhme for direction of arrival [26].

An alternative approach that does not require knowledge of the number of sources was introduced by discretizing the field into a set of effective sources. Estimation of the number of sources is avoided by assuming a source exists at every grid point, corresponding to bearing. This approach was originally proposed for radio astronomy [27, 28] but has been shown to be particularly useful in dynamic environments. When sources have high bearing rates relative to the array’s resolution, the number of snapshots is limited to instances when the received data has a nearly constant covariance matrix [29]. This reduces performance for data dependent processing techniques, especially in the limiting cases where a single snapshot exists per array location. For the towed array case, the array shape change will be limited by tow-

ship movement. Covariance matrix inversion requires at least  $2M$  (twice the number of sensors) snapshots to have array gain within 3dB of maximum performance [30]. The number of snapshots required can be reduced when sources reside in a low rank subspace via eigenvector decomposition, known in acoustics as Dominate Mode Rejection (DMR) beamforming [31]. Also, the signal subspace can be physically constrained using knowledge of the environment [20, 32]. One straight forward method is to limit the set of signal vectors to the locations of physically propagating waves, which was implicitly implemented in early numerical EM solutions by Miller and Fuhrmann [25].

Lanterman, in the field of astronomy, mapped field intensity using a complex normal signal model for stationary fields and uncorrelated sources. The iterative solution for the spatial spectrum, denoted  $\Sigma$ , is given by

$$\Sigma^{\text{new}} = \Sigma^{\text{old}} - \frac{1}{N} (\Sigma^{\text{old}})^2 \sum_{n=1}^N \left( \mathbf{V}^{\text{H}}(n) \mathbf{K}^{-1}(n) \mathbf{V}(n) - \mathbf{V}^{\text{H}}(n) \mathbf{K}^{-1}(n) \hat{\mathbf{R}}(n) \mathbf{K}^{-1}(n) \mathbf{V}(n) \right) \quad (2.7)$$

where  $\mathbf{K}(n) = \mathbf{V}(n) \Sigma^{\text{old}} \mathbf{V}^{\text{H}}(n) + \sigma_{\eta}^2 \mathbf{I}$  and  $\hat{\mathbf{R}} = \frac{1}{N} \sum_{n=1}^N \mathbf{x}(n) \mathbf{x}^{\text{H}}(n)$ . The variance of the noise is given by  $\sigma_{\eta}^2$ . This work was extended to towed arrays by Rogers and Krolik using a pseudo-stationary assumption described by

$$f(\Sigma(n) | \Sigma(n-1)) = \delta(\Sigma(n) - \Sigma(n-1)). \quad (2.8)$$

This allows for a slowly time-varying estimate of the field through a sliding window of length  $N$ , where the field can vary between windows [33]. An online estimate has been formulated that initializes the EM algorithm with the estimate from the previous time interval [34]. The broadband case is formulated by averaging the narrowband estimates. The beginning of Chapter 4 is an extension of this work. However, this method requires knowledge of the array shape.

## 2.2 Towed Array Shape Estimation

Towed underwater arrays that process data below 1000 Hz have large apertures due to the increasingly larger wavelengths at low frequencies. Deploying systems of such size requires the array to be constructed using a flexible cable. The problem with these systems is that the shape of a cable underwater is unknown. For example, ocean currents and the effects of hydrodynamics can cause the array to delineate from the tow path [35]. Additionally, during sharp turns the array shape will become distorted, and the global orientation of the array will change over time. Since the ocean is a large place, the array shape with respect to a moving reference frame is important and translations of the reference frame itself are fairly unimportant. Said another way, an unknown bend in the array will degrade performance but moving a full array length forward will not change the bearing of a far-field source [2]. Synthetic aperture techniques discussed in the previous section exploit this movement but is not commonly used with low frequency noise. Therefore the array shape is parameterized in a way analogous to the signal wavefront direction of arrival [36]. The array shape can be found using external systems, such as high frequency acoustic transponders [37] or heading sensors [38]. Estimating array parameters using in-band acoustic data is often referred to as array shape calibration. For arbitrary stationary array shapes, the parameters are not always observable. Rockah and Schultheiss provided 2-D observability guarantees when the location of a single sensor and direction to a second sensor are known or the location of one sensor was known and at least 3 disjoint sources are present [39]. This motivates using GPS data for tow-ships and tow-point indicators for an array, provided direction to a sensor. The traditional ML function considers local perturbations of the array shape [39], as the ML estimate is a local approximation [22]. This allows normally distributed priors on the arbitrary array shapes to form MAP estimates of the  $x$ - $y$  sensor positions [40].

However, towed-arrays do not have arbitrary shapes but can be described using mechanical models. The seminal paper by Paidoussis models the array as a thin cylinder with uniform mass that is pulled through the water [41]. An approximation to the Paidoussis equation was introduced using a low-order mechanical model of the array, similar to a string, that accurately matched towed array data [42] is given by

$$(\rho - 1)(\xi - 1) \frac{\partial^2 \psi}{\partial \xi^2} + \rho \frac{\partial \psi}{\partial \xi} + \frac{\partial \psi}{\partial \tau} = 0, \quad (2.9)$$

where  $\xi$  is the spatial dimension,  $\psi$  is bearing, and  $\tau$  is time. For discretized solutions,  $\rho$  is the fraction of a spatial discretization the tow motion travels down the array and is bounded such that  $0 < \rho \leq 1$ . The physical model is often discretized in a fashion resembling a chain link, shown in Figure 2.3, where the inter-element spacing is known but the heading between segments is unknown. An alternative derivation uses  $x$ - $y$  positions instead of headings [38]. Sensor element locations are often used for spatial discretization. This technique is referred to as the water-pulley model, where the tow cable follows the tow ship through the water. However, mechanical models are unable to easily incorporate ocean currents [43]; thus sensors along the array are used to estimate the true shape. Traditionally, acoustic data from reference sources at

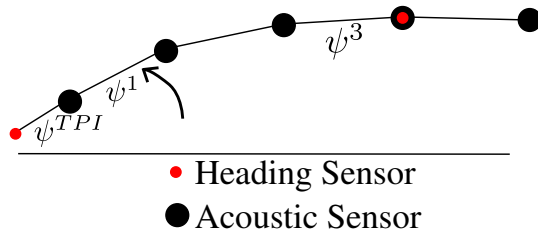


FIGURE 2.3: Traditional physical model of towed array

known locations have been used to estimate the array shape. Unlike the observability requirements for arbitrary arrays, towed array parameters are observable when the array is nominally linear and a single source over  $180^\circ$ , excluding endfire (e.g. not

co-linear with the array) [44]. More recent work has focused on using reduced signal subspace techniques to increase spatial resolution, e.g. Park *et. al* [45, 46]. However, Park’s work assumes a large number of snapshots, i.e. 1000 snapshot for 10 sensors elements. An estimate must account for the time-varying nature of the array, and thus consider a more limited number of snapshots.

One method of decreasing sensitivity to snapshot support is parameter reduction, analogous to model bias/variance tradeoffs. For active sonar, Varadarajan and Krolik derived a reduced basis solution using principle component analysis (PCA) on array headings [47]. A linear basis was incorporated into the Kalman filter formulation and verified experimentally with towed array heading data. This concept is discussed in detail in Section 3.2 and proposed for passive sonar.

The more classical approach uses tools from numerical analysis: polynomial approximation and interpolation. Credit is typically given to Owsley for first proposing polynomial approximation for towed array shape estimation. Since towed array cables are continuous, polynomial models guarantee a continuous function as well as continuous derivatives that naturally correspond to tow cables [48]. The 3D case was considered and a low order model was suggested by Howard and Syck that explicitly considers boundary conditions [49]. One of the major contributions was to note the importance of curvature as the second derivative of  $x, y, z$  spatial dimensions, where the independent parameter of interest was arc length down the array. More recently, array shape dynamical models based on Howard and Syck’s formulation have been suggested that include the inertia due to the mass of the tow platform and cable. These effects were ignored in previous literature and do not appear in (2.9). The formulation including drag normal to the array was proposed as part of a Kalman filter by Newhall *et al.* [50], where non-linear effects were modeled through an extended Kalman filter. The Kalman filter for the water pulley model was proposed by Gray *et al.*, who also showed the equivalent forms of an array parameterized in Cartesian

coordinates or in heading. However, Newhall *et al.* extended the non-linear model proposed by Howard and Syck to include tow platform mass as well as parameterizing the array shape in terms of heading in order to easily form the Kalman filter for heading data. The same formulation is used in the work proposed here. The dynamical model, based on [50], is provided in detail in Section 3.3. Since the work was originally published in short conference proceedings, the work here provides an expanded description of the model. Alternatively, other models have been considered by Tichavsky and Wong, which shows the equivalency of the 2D and 3D case but focuses on ocean currents [43].

### 2.3 Horizontal Ambient Ocean Noise

Before continuing with a review of general array calibration techniques, the specific problem of ocean ambient noise is considered. There are many sources of ambient noise in the ocean, and the following summary is from the seminal work by Wenz [51]. At low frequencies, below 1kHz, the prevailing sources are local ships and global shipping lanes. At middle frequencies, 1's kHz, shipping traffic begins to be dominated by surface waves and wind noise depending on current weather conditions. These effects are more prominent closer to the surface. Higher frequencies, 10's kHz, are dominated by local effects such as marine biology and surface changes such as rain or spray. A thorough review of past and current studies of ambient ocean noise can be found in the 2011 book by Carey and Evans [52]. The full 360° horizontal field has been heavily studied by Wagstaff, with early work found in [6]. More recently in 2005, Wagstaff studied a basin in the Pacific and showed that the ambient ocean noise from shipping traffic appeared as many point sources in bearing. The field directionality map had many sharp peaks in horizontal bearing but power was concentrated vertically within 12° of the horizon [53]. The vertical components were measured with a vertical array. Wagstaff's work showed that horizontal arrays can

measure shipping traffic from long distances where ship noises near continental slopes and shelves propagated through deep ocean channels that continuously refract the sounds. For low frequencies, the noise from shipping traffic at the edge of the ocean basin can dominate the noise field throughout the ocean basin. This concept is crucial to the array shape algorithms proposed in the work here. The following section describes joint array and source parameter estimation algorithms for both generic arrays and towed sonar arrays. However, the previous work in this area assumes that reference sources in the field are placed for array shape calibration or loud sources of opportunity are exploited. Loud sources from nearby positions provide convenient sources but can quickly change bearings. A key feature of the idea introduced here is that sources that are far away, e.g. shipping traffic near ports on the edge of ocean basins, can be exploited as nearly static sources of opportunity. Unfortunately due to the complicated and long channels in which these sources propagate, approximating each source as a single point target can be inaccurate. For this reason, a different model is used, similar to the original one used by Wagstaff's early work [6]. The differences between the statistical source models in literature are discussed in the following section.

## 2.4 Joint Array/Source Parameter Estimation

In passive sonar where the array shape is uncertain, the source locations are unknown and therefore the source and array parameters must be jointly estimated. This section reviews work that assumes the number of sources is known and performs the joint optimization. The traditional approach is to combine solutions derived independently for source and array parameter estimation. This process is often referred to as self-calibration to emphasize the lack of external calibration/reference information. There are two signal models considered, a stochastic and deterministic signal. A timeline of work based on the deterministic, also referred to as conditional,

signal model is discussed first.

#### *2.4.1 Conditional Maximum Likelihood*

The conditional ML estimate for the joint estimation problem was first proposed by Weiss and Friedlander [54]. The numerical solution requires alternating between solving for source parameters and array parameters until the solution converges. The algorithm was proposed for arbitrary array shapes and has been refined to estimate the number of sources and reduce numerical complexity [55]. An alternative approach was proposed by aligning frequency-wavenumber data such that the peaks match point sources [56] or form shapes of peaks [57]. This requires pre-processing the data by beamforming the data and operating in the spatial domain. The method developed in [54, 55] is the most commonly used and considered the standard for performance comparison [58, 59].

The combination of Weiss and Friedlander’s acoustic based work and Gray’s Kalman filter for towed array heading sensors leads to an alternating iterative solution for moving arrays. Goldberg’s work provides a Kalman filter on array element heading as well as source direction of arrival, which allows source tracking for multiple targets [60]. Goldberg’s algorithm distinguishes between sources with intersecting bearings by assuming sources maintain constant velocity. However, the number of sources must be known and tracking is considered only over an unambiguous section of the bearing space, at most  $180^\circ$ . One problem that arises when using source bearing as input data for a Kalman filter is data association. For successive measurements, a bearing estimate may correspond to a different source and must be associated with a source through motion models, such as constant velocity or stationary bearings. The former assumption of constant velocity can be generalized to constant acceleration but requires more parameters. The latter assumption on stationary bearing is valid for an ML estimate over short time intervals since the

estimate converges to a local solution, which can be initialized by the previous solution. The problem of finding a global solution or finding a good initial condition, even for a static array, is a difficult problem and several non-parametric solutions have been proposed [59, 61]. Additionally, the problem of assuming an unambiguous environment does not appear to be addressed in previous literature since linear arrays allow for only an unambiguous  $180^\circ$ .

Instead of using a using the ML estimate by Weiss and Friedlander, Chung and Wan derived an EM solution for the joint problem [62]. Again alternating between source and array parameters, the solution formed a Space Alternating Generalized EM (SAGE) algorithm [26, 63, 64]. This performs an ML estimate on each parameter, and a claim in [62] is that the SAGE solution is less sensitive to the initial conditions.

A fundamental assumption in the solution proposed by Weiss and Friedlander, and subsequent work, can be described as the least squares estimate on the underlying source signal. Assume a linear model  $\mathbf{x} = \mathbf{A}\mathbf{s} + \boldsymbol{\eta}$  with white circularly symmetric complex normally distributed noise,  $\boldsymbol{\eta}$ . The least squares solution for the source signal, when the steering matrix  $\mathbf{A}$  is known, is  $\mathbf{s} = (\mathbf{A}^H \mathbf{A})^{-1} \mathbf{A}^H \mathbf{x}$ . This is also the ML solution for a *deterministic* signal model. A second signal model considered assumes the source signal is circularly symmetric complex normally distributed with zero mean and variance representing source power. Stoica and Nehorai showed the stochastic ML estimate has lower variance and derived a detailed comparison, assuming known array parameters [65]. Their work showed that the deterministic model results in an estimate that is less efficient than the stochastic signal model. The divergence of the likelihoods is described by Van Trees and is most pronounced with when sources are closely spaced, highly correlated, or vary in SNR levels [5, p. 1008].

#### 2.4.2 *Unconditional Maximum Likelihood*

The stochastic signal model assumes the source waveform is a circularly symmetric complex normally distributed random process with zero mean and unknown variance. The derivation of the ML estimate was given by Böhme [22], in work on source parameter estimation. The unknown phase of the wavefront can be estimated using the eigenvectors of the covariance, as suggested by Paulraj and Kailath [66]. Source power and joint array/source (location) parameter estimates are separable in the stochastic model, first shown by Jaffer [67]. However, the solution is computationally intensive and requires a multi-dimensional search in a non-convex space even when array parameters are known (i.e. source direction and power unknown), which led Friedlander and Zeira to formulate an eigenvector method using known array shapes [14]. A less computationally intensive method was proposed by Viberg and Swindlehurst [40]. Their method forms a MAP estimate by assuming normal priors on each of the parameters. The numerical solution is found using a local linear approximation and converges via Newton's method. The ML solution is a special case of the MAP estimate, thus the approximation also can be used with no prior information. Viberg and Swidlehurst derived a solution for a towed array shape model but do not consider motion. Their analysis assumes at least 100 snapshots for the 10 element array. Prior knowledge, for the MAP estimate, may be available from non-acoustic sensors or known configurations. When there are multiple arrays of known shape with unknown relative orientation or phase, the problem is often referred to as partially-calibrated arrays [68, 69].

A few notes on the current state of the literature. There has been little consideration of the time-varying nature of a towed-array with unknown shape using acoustic data. The most significant contribution was proposed by Goldberg [60], whose work considers only the conditional maximum likelihood estimate. The use

of the unconditional or stochastic model is typically limited by the difficulty in solving for a joint solution, as stated by several authors, and remains an open problem [5, 40, 70]. Additionally, the problem was considered in the active case using the clutter by Varadarjan and Krolik, where a reduced parameter set modeled a dynamic array shape [47].

# 3

## Data Model

This chapter describes passive acoustic and heading sensor data models for a maneuvering towed hydrophone array. Acoustic narrowband and broadband frequency domain models are derived for unconditional ML estimates. For acoustic data, a narrowband model is given initially and then extended to a broadband model. A parametric array shape model is introduced for an arbitrary curve. The water pulley model is considered first, where simulated data is used to motivate a low rank parameterization. A non-linear array shape model is then considered using a low order polynomial interpolation. Since the motion model used here is not well known (although published), a brief comparison to traditional models and relevant issues are discussed.

Consider an array of  $M$  sensors collecting band-limited discrete-time data over an observation window indexed by  $n$ , referred to as a time instance. During data collection of time  $T$ , the array and acoustic field are assumed to be fixed. A single acoustic data collection, or snapshot, is indexed by  $n$  and modeled in the frequency domain. The coordinate system for sensor and source locations is defined by Figure 3.1, where bearing and elevation angle are represented by  $\theta$  and  $\phi$  respectively.

Bearings are held to a constant (North) while the origin moves with respect to the observation platform. Assume a far-field model such that the distance between array locations at sequential data collections is much less than the distance from the array to a source.

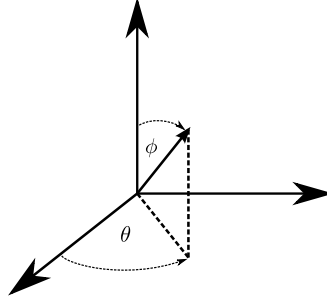


FIGURE 3.1: Polar coordinate system

### 3.1 Signal Model

The narrowband frequency domain model is given in terms of frequency,  $\omega$ , in radians from the  $m$ th sensor at the  $n$ th snapshot by  $x_m(n, \omega)$ . Sources are assumed to be far-field point sources, which vary in location as a function of time instance  $n$ . Sources are spatially parameterized by the wavenumber vector  $\mathbf{k}$ , given in (3.1), with length corresponding to the spatial wavelength

$$\mathbf{k}(n, \omega) = \frac{\omega}{c} \begin{bmatrix} \cos \theta(n) \sin \phi(n) \\ \sin \theta(n) \sin \phi(n) \\ \cos \phi(n) \end{bmatrix}, \quad (3.1)$$

and phase speed  $c$  in meters/sec. This vector points from the array to the source where  $-\mathbf{k}$  is used to denote propagation from the source to the array. The vector from the platform origin to each array element is denoted  $\mathbf{r}_m$ . The phase from the wavefront is modeled while the amplitude across the array is assumed to be negligible for far-field propagation. Note this model assumes no knowledge of the

original transmitted signal amplitude, which is typical in passive sonar. The phase, or array manifold vector, across the array for the  $q$ th source is given by the  $M \times 1$  element array

$$[\mathbf{a}_q(n, \omega)]_m = \exp(-j\mathbf{k}_q^T(n, \omega)\mathbf{r}_m(n)). \quad (3.2)$$

The  $M \times 1$  received data vector is formed by stacking data received by each sensor as  $\mathbf{x}(n, \omega) = [x_1(n, \omega), x_2(n, \omega) \cdots x_M(n, \omega)]^T$ . For  $Q$  sources, the signal vector is also stacked to form  $\mathbf{s}(n, \omega)$ . A steering matrix is formed by augmenting, or concatenating, steering columns  $\mathbf{A}(n, \omega) = [\mathbf{a}_1(n, \omega), \mathbf{a}_2(n, \omega) \cdots \mathbf{a}_Q(n, \omega)]$ . The received data vector is given by

$$\mathbf{x}(n, \omega) = \mathbf{A}(n, \omega)\mathbf{s}(n, \omega) + \boldsymbol{\eta}(n, \omega) \quad (3.3)$$

with noise represented by  $\boldsymbol{\eta}$ .

Source signals are jointly modeled as zero-mean circularly symmetric complex normally distributed random variables with covariance matrix  $E[\mathbf{s}(n, \omega)\mathbf{s}(m, \omega)] = \boldsymbol{\Sigma}(n, \omega)\delta(n - m)$ . The noise is independent of the source signals and circularly symmetric complex normally distributed with zero mean and covariance  $\sigma_\eta^2\mathbf{I}$ . For a known array shape the received data has zero-mean and covariance  $\mathbf{R}(n, \omega)$ . This is summarized below.

$$\mathbf{s}(n, \omega) \sim \mathcal{CN}(\mathbf{0}, \boldsymbol{\Sigma}(n, \omega)) \quad (3.4)$$

$$\boldsymbol{\eta}(n, \omega) \sim \mathcal{CN}(\mathbf{0}, \sigma_\eta^2\mathbf{I}(n, \omega)) \quad (3.5)$$

$$\mathbf{x}(n, \omega) \sim \mathcal{CN}(\mathbf{0}, \mathbf{R}(n, \omega)) \quad (3.6)$$

The covariance matrix  $\mathbf{R}(n, \omega)$  is a sum of the received source signal covariance and the noise covariance.

$$\mathbf{R}(n, \omega) = \mathbf{A}(n, \omega)\boldsymbol{\Sigma}(n, \omega)\mathbf{A}^H(n, \omega) + \sigma_\eta^2\mathbf{I}. \quad (3.7)$$

Broadband signals are modeled by Fourier synthesis, using a statistical model first published by Bangs [71]. The broadband signal model is formulated by stacking

multiple narrowband frequencies. The broadband vectors and matrices are denoted with bars. The source signal is expressed by stacking  $B$  narrowband vectors.

$$\bar{\mathbf{s}}(n) = [\mathbf{s}^T(n, \omega_1), \mathbf{s}^T(n, \omega_2), \dots, \mathbf{s}^T(n, \omega_B)]^T$$

The time-bandwidth product for the received data is assumed to be large. The rule-of-thumb is that the full bandwidth times the observation interval is greater than 16,  $BW \times T > 16$  (for analysis see [4]). In this case, each frequency bin can be approximated as independent; the signal vector is distributed  $\bar{\mathbf{s}} \sim \mathcal{CN}(0, \bar{\Sigma}(n))$ , where  $\bar{\Sigma}(n)$  is block diagonal.

$$\bar{\Sigma}(n) = \begin{bmatrix} \Sigma(n, \omega_1) & & \mathbf{0} \\ & \ddots & \\ \mathbf{0} & & \Sigma(n, \omega_B) \end{bmatrix}.$$

The received data vector and steering matrices are similarly stacked,

$$\bar{\mathbf{x}}(n) = [\mathbf{x}^T(n, \omega_1), \mathbf{x}^T(n, \omega_2), \dots, \mathbf{x}^T(n, \omega_B)]^T$$

$$\bar{\mathbf{A}}(n) = [\mathbf{A}^T(n, \omega_1), \mathbf{A}^T(n, \omega_2), \dots, \mathbf{A}^T(n, \omega_B)]^T$$

and distributed,  $\bar{\mathbf{x}}(n) \sim \mathcal{CN}(0, \bar{\mathbf{R}}(n))$ , with block covariance matrix

$$\bar{\mathbf{R}}(n) = \begin{bmatrix} \mathbf{R}(n, \omega_1) & & \mathbf{0} \\ & \ddots & \\ \mathbf{0} & & \mathbf{R}(n, \omega_B) \end{bmatrix} \quad (3.8)$$

$$\bar{\mathbf{R}}(n) = \bar{\mathbf{A}}(n)\bar{\Sigma}(n)\bar{\mathbf{A}}^H(n) + \sigma_\eta^2\mathbf{I}.$$

### 3.2 Water Pulley Array Shape Model

The water pulley model reviewed in Section 2.2 is used to model the towed array shape. The model approximates the towed array as piecewise linear, with physical

parameters shown in Figure 2.3. The array shape for the  $n$ th instance is a function of the heading from the previous,  $n - 1$ , instance as well as the towed forcing function. The partial differential equation for the simplified water pulley model is given by

$$\frac{\partial \psi}{\partial t} = -\tilde{\rho}v \frac{\partial \psi}{\partial x} \quad (3.9)$$

where  $\tilde{\rho}$  is a mechanical property related to stiffness,  $v$  is tow platform velocity tangent to the tow cable,  $t$  is time, and  $x$  is the spatial dimension. Additionally, a forcing function,  $\mathbf{u}$ , is known and caused by platform motion. Using a tow-point indicator (TPI), the forcing function is  $\mathbf{u} = \rho[\psi^{\text{TPI}} \ 0 \ 0 \ \dots]^T$ . Using a first-order discretization of (3.9), a state update equation is given by

$$\boldsymbol{\psi}(n) = \mathbf{F}\boldsymbol{\psi}(n - 1) + \mathbf{u}(n) + \boldsymbol{\epsilon}(n) \quad (3.10)$$

with noise term  $\boldsymbol{\epsilon}(n)$ . The state update matrix  $\mathbf{F}$  propagates the tow motion down the array according to

$$\mathbf{F} = (1 - \rho)\mathbf{I}_{N-1} + \rho \begin{bmatrix} 0 & 0 & 0 & 0 \\ 1 & 0 & 0 & 0 \\ 0 & \ddots & 0 & 0 \\ 0 & 0 & 1 & 0 \end{bmatrix}, \quad (3.11)$$

where  $\rho = \tilde{\rho}v\Delta_t/\Delta_x$  is the fraction of a spatial discretization that the forcing function propagates during a time step. Time and space discretization are given by  $\Delta_t$  and  $\Delta_x$  respectively. Note that  $\rho$  is limited such that  $\rho \leq 1$  for (3.11) to remain a valid approximation. In the literature, this value is typically close to  $\rho = 1$  since small forcing functions are used, and the tow cable is assumed to be nominally linear [38, 60].

When a large number of parameters is required, the estimate becomes difficult or computationally infeasible. For towed arrays, Varadarajan and Krolik proposed an empirical reduced basis set for the heading parameters [47]. While the application

in [47] is active sonar, the same physical array model can be applied to the passive case. Their work was verified with experimental data from heading sensors on a towed array. They suggested using principle component analysis (PCA) to find a reduced basis set for the heading sensors. In general, a linear basis set for the heading data is modeled

$$\psi = \mathbf{B}\gamma \tag{3.12}$$

Using platform maneuvers of the same form described in [47], this formulation can be intuitive understood. Consider an example sinusoidal maneuver between  $\pm 20^\circ$  using an array with 30 elements traveling 2 m/s. The array headings are sampled at 10 Hz, which is also used for the simulation time step,  $\Delta_t$ . For a stiffness of  $\tilde{\rho} = .96$ , the singular value spectrum of the heading data is given by Figure 3.2. Most of the

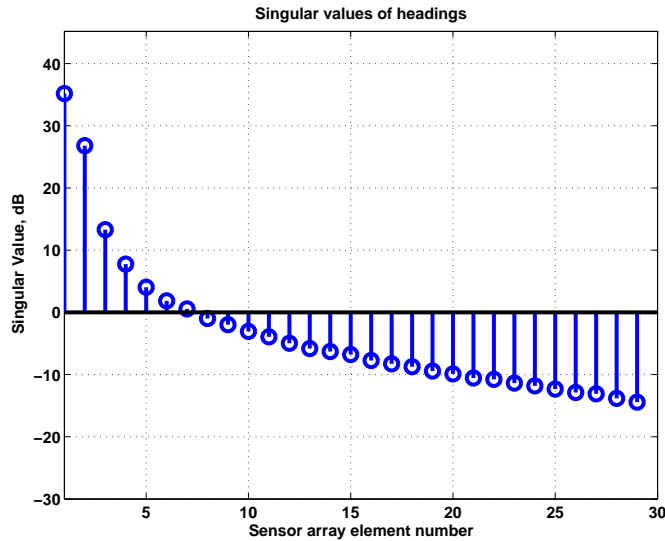


FIGURE 3.2: Singular value spectrum of array heading

information can be found in a few singular vectors. As noted in [47], a small value of  $\rho$  must be used to find a basis set. The trade-off is a larger data collection for a smaller parameter set.

Each singular value corresponds to a singular vector as well as an array shape.

The shapes corresponding to the largest seven eigenvalues are given in Figure 3.3. These shapes essentially correspond to the normal modes of the cable. It is interesting that the first two shapes are a straight line and a parabola, as these two shapes are also used by Gerstoft *et al.* to approximate a towed array using only the GPS data from a ship [17].

Note the state update, (3.10) can be written in terms of the basis parameters,  $\gamma$ , from (3.12) as given by

$$\gamma(n) = \mathbf{B}^\dagger(\mathbf{F}\mathbf{B}\gamma(n-1) + \mathbf{u}(n) + \epsilon(n)), \quad (3.13)$$

where  $\mathbf{B}^\dagger = (\mathbf{B}^H\mathbf{B})^{-1}\mathbf{B}^H$ . This will be used to generate the towed array positions for water pulley based array shape estimation.

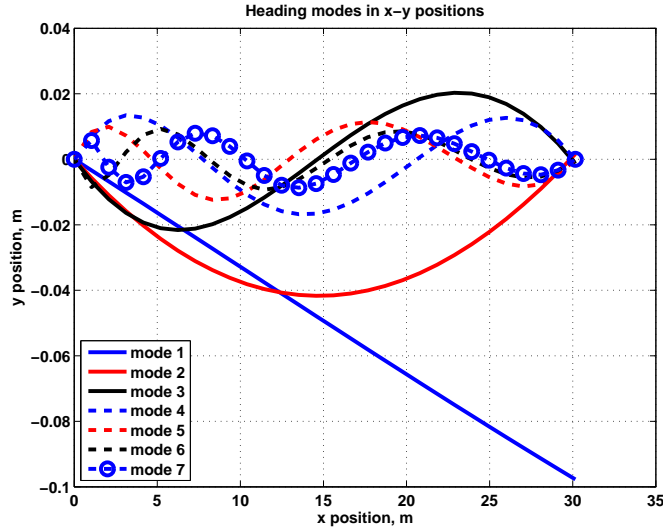


FIGURE 3.3: Array heading modes

### 3.3 Non-linear Array Shape Model

While the water pulley model assumes the tow cable is a string and considers stiffness through a single parameter,  $\rho$ , the model assumes a small bend approximation. A dynamical array shape model that includes a wide range of maneuvers can be derived

by treating the array as a string and solving the force balance equations in terms of headings [50]. The goal of the expanded model is to consider both small maneuvers, such as in the previous section, as well as severe turns. Note that the water pulley model is limited to slow, wide turns and is unable to predict motion when the array or cable is significantly bent. For example, the water pulley model essentially assumes that each segment follows the heading of the segment directly in front of it. However during a sharp turn, the tow platform will slide through the turn such that the forcing function will propagate down the array as a function of heading. Additionally, the sharp turn will diffuse down the tow cable such that the final section may cut through the turn. Both the normal and tangential drag components of the tow cable or array are considered in the non-linear array shape model.

Instead of starting with the piecewise linear model, assume the tow cable is a continuous function in  $x, y$  space. The shape can be described in terms of a continuous function of the angle tangent to the cable from North,  $N$ . Instead of using the  $x$ -axis as the nominally linear shape of the array, the arc length down the array is given by  $d$  where  $d = 0$  is the origin and  $d = L$  is the end of a cable of length  $L$ . The coordinate system is shown in Figure 3.4. Parameterization in this

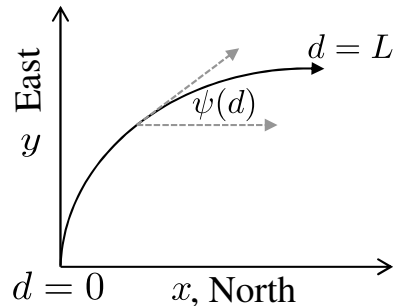


FIGURE 3.4: Array shape parameterization as function of arc length down array with origin at the tail of the array

way allows heading sensors to be described as sampled locations at known locations in  $d$ . Additionally, hydrophone locations are also at known lengths down the cable.

The model was described by Newhall *et al.* as a set of coupled differential equations as given by [50]

$$\frac{\partial \psi}{\partial t} = u \frac{\partial \psi}{\partial d} - \frac{\partial v}{\partial d}. \quad (3.14)$$

and

$$v = -\text{sign} \left( \frac{\partial \psi}{\partial d} \right) \sqrt{\left| \frac{T}{c_N} \frac{\partial \psi}{\partial d} \right|}$$

$$\frac{\partial u}{\partial d} = -v \frac{\partial \psi}{\partial d} \quad (3.15)$$

$$\frac{\partial T}{\partial d} = c_T \text{sign}(u) u^2$$

where the dependent variables are time,  $t$ , and the arc-length down the array  $d$ . The independent parameters are the heading tangent to the array,  $\psi$ , the velocity in the direction tangent to the array,  $u$ , the velocity normal to the array  $v$ , and tension  $T$ . The normalized drag parameters tangent,  $c_T$ , and normal,  $c_N$ , to the array are a physical properties based on array size and shape.

The equations from (3.14)-(3.15) are solved in the discrete domain by sampling at locations  $\mathbf{d} = [d_1 \cdots d_{\text{seg}}]$ , breaking the array into a known number of segments. Similarly, the same locations are used to discretize velocity,  $u$  and  $v$ , as  $\mathbf{u}$  and  $\mathbf{v}$ . The discretized first-order equivalent of (3.14) can be written as

$$\boldsymbol{\psi}_n = \boldsymbol{\psi}_{n-1} + \delta_t \left. \frac{\partial \boldsymbol{\psi}}{\partial t} \right|_{t=\delta_t n}$$

$$\boldsymbol{\psi}_n = \boldsymbol{\psi}_{n-1} + \delta_t \mathbf{D}_s \mathbf{U} \boldsymbol{\psi}_{n-1} - \delta_t \mathbf{D}_s \mathbf{v} \quad (3.16)$$

$$\boldsymbol{\psi}_n = (\mathbf{I} + \delta_t \mathbf{D}_s \mathbf{U}) \boldsymbol{\psi}_{n-1} - \delta_t \mathbf{D}_s \mathbf{v}$$

where  $\delta_t$  is the time discretization,  $\mathbf{U}$  is a diagonal matrix with  $\mathbf{u}$  on the diagonal, and  $\mathbf{D}_s$  is the first spatial derivative. In this case, spatial samples with uniform

spacing of  $\delta_d$  are used, and  $\mathbf{D}_s$  given by

$$\mathbf{D}_s = \frac{1}{2\delta_d} \begin{bmatrix} -3 & 4 & -1 & 0 & \cdots & 0 \\ -1 & 0 & 1 & 0 & & 0 \\ 0 & -1 & 0 & 1 & \ddots & \vdots \\ 0 & \ddots & \ddots & \ddots & \ddots & 0 \\ \vdots & & & 0 & -1 & 0 & 1 \\ 0 & \cdots & 0 & 1 & -4 & 3 \end{bmatrix}$$

Note that (3.14) can be solved in discrete form using (3.16) given a previous heading.

The boundary conditions for (3.15) are given by

$$T(t, 0) = 0$$

$$u(t, L) = u_L \cos(\psi - \psi_L) - v_L \sin(\psi - \psi_T)$$

$$v(t, L) = u_L \sin(\psi - \psi_L) - v_L \cos(\psi - \psi_T)$$

in terms of the tow point velocities,  $u_L, v_L$  and tow direction,  $\psi_T = \psi(t, L)$ . The differential equations, (3.15), are solved numerically using the 2nd order Runge-Kutta method. Special thanks to Bruce Newhall for suggesting the use of this model and providing insightful feedback on the initial work.

## Spatial Spectrum and Array Parameter Estimators

Passive source localization through beamforming typically assumes the receiver element locations are known and static. The shape of a towed array changes as it is pulled behind a maneuvering platform. First, a method to estimate the time-varying spatial spectrum for dynamic arrays is introduced in Section 4.1 assuming the shape is known. In the temporally broadband case, performance gains are possible when the target temporal spectral shape is known, and the broadband case is considered in Section 4.3. Since the array is mounted to underwater flexible cables, the array shape may be unknown. This is especially problematic during sharp maneuvers as the cable bends significantly, and mismatch between the true and assumed array shape can result in significant source detection and localization performance loss. Therefore an acoustic based array shape estimate based on the water pulley model is introduced in Section 4.5. Heading sensor data is considered as a constraint, and array shape parameters from active sonar work [47] are used. Separately, an acoustic based array shape estimate based on a non-linear array shape dynamical model is introduced in Section 4.6, where array shape parameters are formed directly from the physical model. Finally, a method to statistically fuse heading data with the

acoustic based estimate is provided in the framework of an extended Kalman filter.

The underwater acoustic community often refers to the spatial spectrum as the field directionality, and these terms are used inter-changeably here.

#### 4.1 Narrowband Spatial Spectrum Estimators

Recent work by Rogers and Krolik has shown the increased end-fire resolution and disambiguation ability of a maneuvering array with known locations [33]. The work proposed in this section was originally published in my M.S. thesis, [72]. Since the array parameter estimators build on my previous spatial spectrum estimation techniques, this work is included for completeness. Two narrowband estimates are first established then expanded to include broadband data. Knowledge of the temporal spectrum with broadband data is shown to improve performance, especially in the presence of spatial aliasing. Spatial spectrum estimation is formulated here as a covariance matrix estimation problem, where the source signal covariance is the unknown parameter of interest. In this section, only narrowband data is considered.

Let an assumed steering vector be defined as an array manifold vector parameterized by an arbitrary ( $q$ th) wavenumber,  $\mathbf{v}_q(n, \omega) = \mathbf{a}_q(n, \omega)$ . Assume the angular space around the array platform is a grid of  $Q'$  points, where  $Q'$  is greater than the number of sources  $Q' > Q$ . Since the number of sources is unknown, the received data is approximated as sum of  $Q'$  uncorrelated planewaves. This nonparametric approach is similar to classical temporal spectral estimation and was originally proposed by Fuhrmann [20]. In this approach, the received data is modeled using a steering matrix defined as

$$\mathbf{V}(n, \omega) = [\mathbf{v}_1 \ \mathbf{v}_2 \ \cdots \ \mathbf{v}_{Q'}]. \quad (4.1)$$

The received data is assumed to be  $\mathbf{x} = \mathbf{V}(n, \omega)\mathbf{s}(n, \omega) + \boldsymbol{\eta}(n, \omega)$  where the  $\mathbf{V}$  is known instead of the unknown  $\mathbf{A}$ . This results in an assumed acoustic data covariance given

by

$$\mathbf{R}(n, \omega) = \mathbf{V}(n, \omega)\mathbf{\Sigma}(n, \omega)\mathbf{V}^H(n, \omega) + \sigma_\eta^2\mathbf{I}. \quad (4.2)$$

The dimensionality of  $\mathbf{V}$  is then  $M \times Q'$  and,  $\mathbf{s}$  is  $Q' \times 1$ . Thus the only unknown parameters are the signal powers, covariance  $\mathbf{\Sigma}$  and noise power,  $\sigma_\eta^2$ . Since the number of sources will not be estimated in the remainder of this work, the number of grid points is referred to as  $Q$  instead of  $Q'$  for notational convenience. Note that data will be generated using point sources corresponding to true source locations, but the proposed method assumes a model containing assumed sources on a grid. The use of  $\mathbf{V}$  instead of  $\mathbf{A}$  denotes mismatch between generated data and the processing method. While it would be possible to describe the method using only the model of  $\mathbf{R}$  given by (4.2), the original point source definition using true source locations in (3.7) is the traditional array processing model.

Discretization provides the bearing angles for a bearing-time-record (BTR) or time-varying field directionality map. The field directionality map is formed using the  $Q$  grid points and are assumed to be uncorrelated. Thus, the  $Q \times Q$  source covariance matrix,  $\mathbf{\Sigma}$ , is diagonal. For far-field grid points, this corresponds to a spatially stationary field, which is a reasonable approximation over a limited array aperture. Time-varying field directionality and platform dynamics are physically constrained and captured by either a deterministic or stochastic model of the underlying covariance matrix, as described in Sections 4.1.1 and 4.1.2 respectively. Note that unlike methods where tracking is performed post-detection (as in Goldberg's work [60]), here the spatial spectrum dynamics are directly modeled within pre-detection processing [73].

#### 4.1.1 Derivative Based Maximum Likelihood: DBML

The first approach models the spectrum deterministically. Dependence on frequency is suppressed for notational convenience throughout narrowband derivations. The

ML estimate of the field directionality at snapshot  $n$  is given in terms of the probability density function (pdf),  $f$ , of the received data is written as

$$\hat{\Sigma}_n = \arg \max_{\Sigma(n)} f(\mathbf{x}(n), \dots, \mathbf{x}(n - N + 1) | \Sigma(n)). \quad (4.3)$$

In the radar literature, derivative-based updating (DBU) methods compensate for time-varying changes of the array (and therefore the clutter covariance matrix) using a first-order model of the adaptive weight vector [74]. In this work, DBU is used to approximate slowly time-varying field directionality using a model for  $\Sigma(n)$  given by

$$\Sigma(k) = \Sigma_o(n) + [k - (n - N + 1)]\dot{\Sigma}(n) \quad (4.4)$$

that applies over a sliding window where  $n - N + 1 \leq k \leq n$  and  $\Sigma_o$  represents the spatial spectrum at the start of the window. Let  $\tilde{k} = k - (n - N + 1)$  be a shifted version of  $k$ . By substituting (4.4) into (4.2), the approximation for the received signal covariance matrix is,

$$\mathbf{R}_x(k) \approx \mathbf{V}(k) \left( \Sigma_o(n) + (\tilde{k} - n)\dot{\Sigma}(n) \right) \mathbf{V}^H(k) + \sigma_n^2 \mathbf{I} \quad (4.5)$$

for  $k = [n, n - 1, \dots, n - N + 1]$ . Treating  $\Sigma_o$  and  $\dot{\Sigma}$  as unknown nonrandom parameters leads to a maximum likelihood estimate given by

$$\hat{\Sigma}_n, \hat{\dot{\Sigma}}_n = \arg \max_{\Sigma_o(n), \dot{\Sigma}(n)} f(\mathbf{X}_n | \Sigma_o(n), \dot{\Sigma}(n)) \quad (4.6)$$

where  $\mathbf{X}_n = \{\mathbf{x}(n), \mathbf{x}(n - 1), \dots, \mathbf{x}(n - N + 1)\}$ .

Since brute-force maximization of the likelihood function is computationally infeasible the Expectation-Maximization (EM) iterative technique is used to approximate the solution [23]. The EM algorithm requires splitting data into incomplete, or observable data, and complete, or unobservable data, where there is a many-to-one relation from the complete data to the incomplete data. The first step is to take

the expectation of the likelihood containing the complete data given the incomplete data and a previous parameter estimate. The second step is maximizing the result with respect to the unknown parameters. As described in previous array processing work using EM algorithms [25, 27, 33], define the complete data as the hidden source and noise signals,  $\mathcal{C}_N(k) = \{\mathbf{s}(k), \boldsymbol{\eta}(k), \dots, \mathbf{s}(k - N + 1), \boldsymbol{\eta}(k - N + 1)\}$  while the incomplete data is  $\mathbf{X}_n$ . The likelihood function with the complete data is given

$$f(\mathcal{C}_N(n)|\boldsymbol{\Sigma}_o, \dot{\boldsymbol{\Sigma}}) = f(\mathcal{C}_N(n)|\boldsymbol{\Sigma}_o, \dot{\boldsymbol{\Sigma}}) = \prod_{\tilde{k}=n}^{n+N-1} G(\mathbf{0}, \boldsymbol{\Sigma}_o(n) + (\tilde{k} - n)\dot{\boldsymbol{\Sigma}}(n))G(\mathbf{0}, \sigma_\eta^2\mathbf{I}) \quad (4.7)$$

in terms of the shift variable  $\tilde{k}$  from (4.5) and  $G(\mathbf{0}, \boldsymbol{\Sigma})$ , representing the zero-mean circular symmetric complex normal density function. Assuming each source is uncorrelated, the expectation of (4.7) with respect to  $\mathbf{s}, \boldsymbol{\eta}$  given a previous iteration is

$$\begin{aligned} & \mathbb{E}_{\mathcal{C}_N(n)} \left[ \ln f(\mathcal{C}_N(n)|\boldsymbol{\Sigma}_o(n), \dot{\boldsymbol{\Sigma}}(n)) \mid \boldsymbol{\Sigma}_o^{\text{old}}, \dot{\boldsymbol{\Sigma}}^{\text{old}}, \mathbf{X}_n \right] \propto \\ & \sum_{\tilde{k}=n}^{n+N-1} \sum_{q=1}^Q -\ln([\boldsymbol{\Sigma}(n)]_{qq} + (\tilde{k} - n)[\dot{\boldsymbol{\Sigma}}(n)]_{qq}) - \frac{h_q(\tilde{k})}{[\boldsymbol{\Sigma}(n)]_{qq} + (\tilde{k} - n)[\dot{\boldsymbol{\Sigma}}(n)]_{qq}} \quad (4.8) \end{aligned}$$

where  $h_q(\tilde{k}) = \left\{ \mathbb{E} \left[ \mathbf{s}(\tilde{k})\mathbf{s}^H(\tilde{k}) \mid \boldsymbol{\Sigma}_o^{\text{old}}, \dot{\boldsymbol{\Sigma}}^{\text{old}}, \mathbf{X}_n \right] \right\}_{qq}$  is the element  $(q, q)$  of the matrix given by

$$\begin{aligned} \mathbb{E} \left[ \mathbf{s}(\tilde{k})\mathbf{s}^H(\tilde{k}) \mid \boldsymbol{\Sigma}_o^{\text{old}}, \dot{\boldsymbol{\Sigma}}^{\text{old}}, \mathbf{X}_n \right] &= \boldsymbol{\Sigma}_o^{\text{old}} + (\tilde{k} - n)\dot{\boldsymbol{\Sigma}}^{\text{old}} + \\ & \left( \boldsymbol{\Sigma}_o^{\text{old}} + (\tilde{k} - n)\dot{\boldsymbol{\Sigma}}^{\text{old}} \right) \mathbf{G}(k) \left( \boldsymbol{\Sigma}_o^{\text{old}} + (\tilde{k} - n)\dot{\boldsymbol{\Sigma}}^{\text{old}} \right), \end{aligned}$$

and the observed data appears in the estimate through the sample covariance matrix  $\hat{\mathbf{R}}(k) = \mathbf{X}_n\mathbf{X}_n^H$  in  $\mathbf{G}(k)$ , which is defined in (4.9). The estimated covariance matrix using the previous estimate is defined as  $\mathbf{K}(k)$ , given in (4.10). To perform the

M-step, the maximization of (4.8) with respect to  $\Sigma(n)$  and  $\dot{\Sigma}(n)$  is performed numerically using the interior point algorithm. The field directionality map,  $\Sigma(n)$ , is constrained to be greater than 0 at every location, and the optimization is limited to 50 iterations.

$$\mathbf{G}(k) = \mathbf{V}^H(k) \left[ \mathbf{K}^{-1}(k) - \mathbf{K}^{-1}(k) \hat{\mathbf{R}}(k) \mathbf{K}^{-1}(k) \right] \mathbf{V}(k) \quad (4.9)$$

$$\mathbf{K}(k) = \mathbf{V}(k) (\Sigma_o^{\text{old}} + k \dot{\Sigma}^{\text{old}}) \mathbf{V}^H(k) + \sigma_\eta^2 \mathbf{I}. \quad (4.10)$$

#### 4.1.2 Recursive Bayes Maximum Likelihood: RBML

Using a Bayesian approach and stochastic model for the field directionality, assume the spectrum is a Markov random process or equivalently has an autoregressive model for the diagonal  $Q \times Q$  matrix  $\Sigma$  given by

$$\Sigma(n+1) = \Sigma(n) + \Delta, \quad (4.11)$$

where  $\Delta$  represents zero-mean state noise on the power from each angle. A more general model can be used, but this simple model leads to a computationally tractable solution for estimating the time-varying frequency-domain spatial spectrum. Uncertainty in the spatial spectrum dynamics is described by the diagonal state noise  $\Delta$ . This provides a probabilistic relation between sequential spectra, referred to as the transition pdf given by

$$f(\Sigma(k) | \Sigma(k-1)). \quad (4.12)$$

Note that  $\Sigma(n)$  in (4.11) is only dependent on the previous time-step  $\Sigma(n-1)$ . This allows the joint pdf to be simplified into a product written in terms of (4.12) given by

$$f(\Sigma(n), \dots, \Sigma(n-N+1)) = \prod_{k=n-N+1}^n f(\Sigma(k) | \Sigma(k-1)), \quad (4.13)$$

which leads to recursion in the estimate. The RBML estimate is defined in terms of the joint distribution of the data and the field directionality according to:

$$\hat{\Sigma}_n = \arg \max_{\Sigma(n)} f(\mathbf{X}_n, \Sigma(n)). \quad (4.14)$$

Letting all possible sequences  $\Sigma(k)$  for  $k = [n, \dots, n - N + 1]$  be defined as  $\mathcal{S}$ , the joint distribution in (4.14) can be written as

$$f(\mathbf{X}_n, \Sigma(n)) = \int_{\mathcal{S}} f(\mathbf{X}_n, \Sigma(n), \dots, \Sigma(n - N + 1)) d\Sigma(n - 1) \cdots d\Sigma(n - N + 1), \quad (4.15)$$

but is not computationally feasible to maximize for two reasons: the complex relation between  $\mathbf{X}_n$  and  $\Sigma(n)$  as well as the large size of  $\mathcal{S}$ .

To solve (4.14) and (4.15), the EM algorithm is again used to simplify the integration over  $\mathcal{S}$ , as suggested by Rogers and Krolik [33] by invoking the forward method from Markov chains [75, pp. 112-113]. The work presented in this section considers the general form of the transition pdf in (4.12) while previous work [33] only considered  $f(\Sigma(k)|\Sigma(k - 1)) = \delta(\Sigma(k) - \Sigma(k - 1))$ . In order to use the EM algorithm, the joint pdf from (4.15) is written in terms of the complete data  $\mathcal{C}_N$  and manipulated using Bayes's theorem,  $f(a, b) = f(a|b)f(b)$ , to express the joint pdf of the completed data and field directionality:

$$\begin{aligned} f(\mathcal{C}_N(n), \Sigma(n - N + 1), \dots, \Sigma(n)) = \\ f(\mathcal{C}_N(n)|\Sigma(n) \cdots \Sigma(n - N + 1)) f(\Sigma(n) \cdots \Sigma(n - N + 1)). \end{aligned} \quad (4.16)$$

To simplify the joint pdf, consider the likelihood of the spatial spectrum given by

$$f(\mathcal{C}_N(n)|\Sigma(n), \dots, \Sigma(n - N + 1)) = \prod_{k=n-N+1}^n f(\mathbf{s}(k), \mathbf{n}(k)|\Sigma(k)). \quad (4.17)$$

Using (4.13) and (4.17), the joint pdf in (4.16) is simplified into a recursive relation

$$\begin{aligned}
f(\mathcal{C}_N(n), \boldsymbol{\Sigma}(n), \dots, \boldsymbol{\Sigma}(n-N+1)) &= \\
&= \prod_{k=n-N+1}^n f(\mathbf{s}(k), \boldsymbol{\eta}(k) | \boldsymbol{\Sigma}(k)) \cdot f(\boldsymbol{\Sigma}(k) | \boldsymbol{\Sigma}(k-1)) \\
&= f(\mathbf{s}(n), \boldsymbol{\eta}(n) | \boldsymbol{\Sigma}(n)) f(\mathcal{C}_{N-1}(n-1), \boldsymbol{\Sigma}(n-1)) \\
&\quad f(\boldsymbol{\Sigma}(n) | \boldsymbol{\Sigma}(n-1))
\end{aligned} \tag{4.18}$$

with initial conditions  $f(\mathcal{C}_1(n-N+1), \boldsymbol{\Sigma}(n-N+1))$  assuming a uniform distribution over  $\boldsymbol{\Sigma}(n-N)$ . The joint pdf from (4.15) is then written in terms of the complete data and the recursion relation, (4.18), in the form

$$\begin{aligned}
f(\mathcal{C}_N(k), \boldsymbol{\Sigma}(k)) &= \left\{ \int_{\mathcal{S}_{k-1}} f(\mathcal{C}_{N-1}(k-1), \boldsymbol{\Sigma}(k-1)) f(\boldsymbol{\Sigma}(k) | \boldsymbol{\Sigma}(k-1)) d\boldsymbol{\Sigma}(k-1) \right\} \\
&\quad \times f(\mathbf{s}(k), \boldsymbol{\eta}(k) | \boldsymbol{\Sigma}(k)) \\
&\quad \text{for } k = n-N, \dots, n \tag{4.19}
\end{aligned}$$

where the integration is over  $\mathcal{S}_{k-1}$ , all possible values of  $\boldsymbol{\Sigma}(k-1)$ . Noting that the form of the integration is similar to an expectation of  $f(\mathcal{C}_N(k-1), \boldsymbol{\Sigma}(k-1))$ , a second order approximation is derived in Appendix A. The natural logarithm of the joint pdf in (4.19) for  $k = n$  is then given by,

$$\ln f(\mathcal{C}_N(n), \boldsymbol{\Sigma}(n)) = \sum_{k=n-N+1}^n -\ln \det(\pi \boldsymbol{\Sigma}(n)) - \mathbf{s}^H(k) \boldsymbol{\Sigma}^{-1}(n) \mathbf{s}(k) + \sum_{k=n-N+1}^{n-1} l_k, \tag{4.20}$$

where the second order terms,  $l_k$ , are defined in (A.3).

The expectation and maximization steps of the EM algorithm are now derived by taking the expectation of the joint pdf of the complete data and spectrum given the incomplete data,  $\mathbf{X}_n$ , and the previous estimate  $\boldsymbol{\Sigma}^{\text{old}}$ . Note the only terms in

(4.20) dependent on  $\mathbf{X}_n$  are the signal terms,  $\mathbf{s}$ . Let the source signal terms from the expectation step be defined  $h_q(k) = \mathbb{E}[|s_q(k)|^2 | \boldsymbol{\Sigma}^{\text{old}}, \mathbf{X}_n]$ . Taking the expectation of (4.20) with respect to the complete data results in

$$\begin{aligned} \mathbb{E}_{\mathcal{C}} [\ln f(\mathcal{C}_N(n), \boldsymbol{\Sigma}(n) | \boldsymbol{\Sigma}^{\text{old}}, \mathbf{X}_n)] \propto \sum_{q=1}^Q \left\{ -N \ln[\boldsymbol{\Sigma}(n)]_{qq} - \frac{(N-1)r_q^2}{2[\boldsymbol{\Sigma}(n)]_{qq}} \right. \\ \left. - \sum_{k=n-N+1}^n \frac{h_q(k)}{[\boldsymbol{\Sigma}(n)]_{qq}} + \sum_{k=n-N+1}^{n-1} \frac{r_q^2 h_q(k)}{2[\boldsymbol{\Sigma}(n)]_{qq}^2} \right\}, \quad (4.21) \end{aligned}$$

where  $r_q^2$  is the variance of  $[\boldsymbol{\Delta}]_{qq}$  in (4.11). The sum over  $Q$  is a result of assuming a spatially stationary field. Let  $h_q = \sum_{k=n-N+1}^n h_q(k)$ , the conditional expectation of the  $q$ th source power summed over the observation window of  $N$  snapshots. The solution to the maximization step of the EM algorithm is found by setting the derivative of (4.21) to zero and solving. Consider the  $q$ th source and refer to the result from (4.21) as  $z$  where the derivative is expressed

$$\frac{dz}{d[\boldsymbol{\Sigma}(n)]_{qq}} = \frac{-N}{[\boldsymbol{\Sigma}(n)]_{qq}} + \frac{0.5(N-1)r_q^2 + \sum_{k=n-N+1}^n h_q(k)}{[\boldsymbol{\Sigma}(n)]_{qq}^2} - \frac{r_q^2}{[\boldsymbol{\Sigma}(n)]_{qq}^3} \sum_{k=n-N+1}^{n-1} h_q(k). \quad (4.22)$$

Since (4.22) only depends on  $q$ , the maximization of  $Q$  parameters in (4.21) reduces to  $Q$  single parameter optimizations. The cubic equation has 2 non-trivial solutions with only one solution assuming the spatial spectrum variance is small, given by

$$[\hat{\boldsymbol{\Sigma}}(n)]_{qq}^{\text{new}} = \frac{h_q}{2N} + \frac{N-1}{4N} r_q^2 + \frac{1}{2N} \left( \left( \frac{N-1}{2} r_q^2 + h_q \right)^2 - 4N r_q^2 \sum_{k=n-N+1}^{n-1} h_q(k) \right)^{\frac{1}{2}} \quad (4.23)$$

The RBML estimate is given by (4.23). This provides a generalization of the time-varying model assumed by Rogers and Krolik [33, 34]. The result from their previous

work can be obtained by setting  $r_q = 0$  for  $q = [1, \dots, Q]$  in the solution (4.23). The previous solution simplifies to  $h_q/N$ , which is the time-average of the expected values of the signal covariance,  $h_q(k)$ .

Note the term  $h_q(k)$  is the  $q$ th element of the vector given by

$$\begin{aligned} \mathbb{E} [|\mathbf{s}(k)|^2 | \boldsymbol{\Sigma}^{\text{old}}, \mathbf{x}] &= \text{Var}[\mathbf{s}(k)] + |\mathbb{E}[\mathbf{s}(k)]|^2 \\ &= \boldsymbol{\Sigma}^{\text{old}} + \boldsymbol{\Sigma}^{\text{old}} \mathbf{G}(k) \boldsymbol{\Sigma}^{\text{old}} \end{aligned} \quad (4.24)$$

where  $\mathbf{G}(k)$  is defined in (4.9) and estimated received data covariance estimate from the previous EM step is

$$\mathbf{K}(k) = \mathbf{V}(k) \boldsymbol{\Sigma}^{\text{old}} \mathbf{V}^H(k) + \sigma_\eta^2 \mathbf{I}. \quad (4.25)$$

Lanterman considers Bayesian estimates using a combination of a likelihood and non-uniform prior (often improper and referred to as regularization)[27], which frequently results in numerical optimizations with high computational cost, as in the DBML method of Section 4.1.1.

## 4.2 Narrowband Simulation

Numerical simulation is used to demonstrate the performance of the two spatial spectrum estimators developed in Section 4.1. The goal is to demonstrate that capturing array dynamics allows a much smaller maneuvering uniform linear array (ULA) to provide field directionality maps comparable to larger arrays by enhancing endfire directions and suppressing backlobes. Assuming white noise  $\sigma_\eta^2 \mathbf{I}$ , the signal-to-noise (SNR) ratio is defined as  $[\boldsymbol{\Sigma}]_{qq}/\sigma_\eta^2$  for the  $q$ th source grid point, using received levels before array gain. Non-white noise is considered in broadband case. Consider a scenario with 4 interferers at positions relative to North at  $-90^\circ$ ,  $-14^\circ$ ,  $135^\circ$  each with 10 dB SNR and  $-135^\circ$  with 3 dB SNR. The environment is assumed to be 2-D because at the deeper end of littoral regions the 3-D noise field is predominately

near the horizon. The target begins at  $60^\circ$  and transitions to  $15^\circ$  with a maximum instantaneous bearing rate of  $-0.26^\circ$  per second with SNR of 3 dB. The cartoon bearing-time-record (BTR) illustrates the scenario in Figure 4.1. BTRs provide a method of viewing the angular map of source directions as it changes over time.

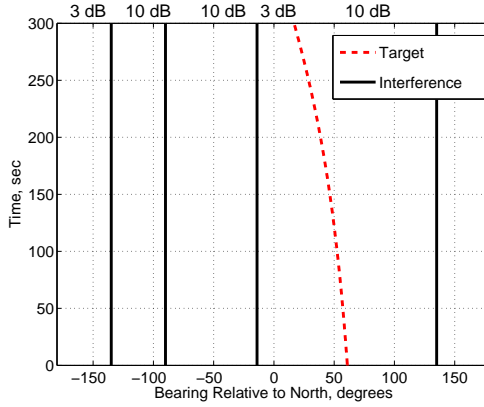


FIGURE 4.1: Illustrative BTR

For the narrowband case, each BTR is computed from  $-180^\circ$  to  $180^\circ$  with  $4^\circ$  spacing and snapshot length of 1 sec. The estimates are computed every 2 seconds, resulting in an overlap of  $\frac{N-2}{N}$  for  $N > 2$ . The simulated data is generated according to (3.3) assuming a narrowband frequency of 750 Hz and speed of sound of 1560 m/s. Conventional beamforming is accomplished by computing  $[\hat{\Sigma}(k)]_{qq} = [\mathbf{V}(k)^H \hat{\mathbf{R}}(k) \mathbf{V}(k)]_{qq}$  at each time instance independently using a rectangular window. The system used to show upper bound or “clairvoyant” performance in this example is a filled 660 element circular array with inter-element spacing of  $\lambda/2$  and diameter  $\approx 110\lambda$ . Circular arrays provide uniform angular resolution. This is compared against a short 7 element ULA maneuvering around the same circle at 2 m/s for 5 minutes with heading increments of  $+1^\circ$  per second. The circle is not fully completed in the simulation, and the circular array is matched to the path covered by the short maneuverable array. Unlike expensive, large surveillance arrays, short maneuverable arrays can be dispersed throughout an environment of interest. Assuming a short array can be

placed at 1/10 the distance to sources, the received SNR would increase by 20 dB under spherical spreading. An equivalent comparison used in this paper is to reduce the array gain of the 600-element array by 20 dB. This normalizes the array such that the large and small array achieve approximately the same output SNR. The large filled circular array is assumed to have a nearly perfect estimate of the received data covariance matrix for conventional beamforming, assuming 100 snapshots at each time instance. The resulting BTR, shown in Figure 4.2, displays each source clearly with a noise floor prescribed by the uniform weights. Previous work has compared a large array with several short fixed arrays at scattered locations using the same total number of elements using optimum placement [76].

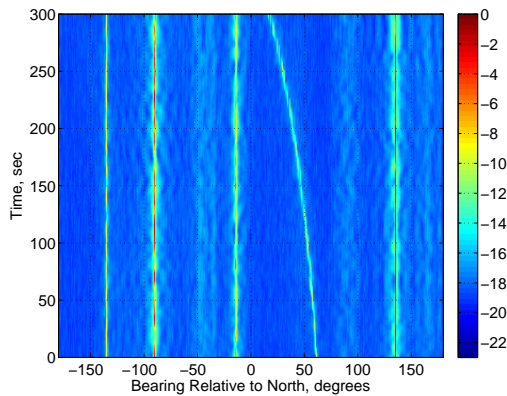


FIGURE 4.2: BTR showing power estimates, in dB, from narrowband conventional beamformer output for clairvoyant circular array.

Conventional beamforming is optimal in spatially diffuse noise limited environments with performance determined by the number of sensors and array weighting schemes. When using few sensors with many sources, however, the interference often limits the detection of weak targets. This occurs in the second array configuration, which utilizes 7 sensors in a ULA at  $\lambda/2$  spacing while maneuvering over the shape of the circular array. The symmetric geometry of a ULA causes ambiguities that appear as backlobes on the BTR. Conventional beamforming at each time instance

is unable to distinguish true sources from backlobes, which appear as diagonal stripes or extremely high bearing rate sources with circular platform maneuvers, shown in Figure 4.3(a). Poor endfire resolution of the ULA is visible as thick lines progressing from  $-180^\circ$  to  $180^\circ$  and also from  $0^\circ$  wrapping around to  $0^\circ$  over time. These problems can be mitigated with time-varying spatial spectrum estimation methods described in Section 4.1. The DBML and RBML algorithms perform 10 iterations every 2 sec, using only a single snapshot for each location. The algorithms approach convergence in this case, but the size of the sliding snapshot window,  $N$ , used by each algorithm is limited by the target motion. It is assumed that a single snapshot is available for each time instance,  $n$ , so that the number of snapshots used by the estimate is same as the size of the sliding window,  $N$ . The DBML estimate, using the previous  $N = 9$  snapshots with  $7/9$  overlap, displays the interferer and target tracks clearly without backlobes, as seen in Figure 4.3(b). For the first 50 seconds, the target is transitioning across the backlobe from the source at  $135^\circ$  and across the end-fire of the array creating uncertainty in the target power estimate. A similar ambiguity occurs again after the 200 second mark when the target passes through endfire again. The RBML estimate uses  $N = 1$  with no overlap and  $r_q = 0$ , as was used for a recent online technique originally developed for maneuvering long towed arrays [34]. The maneuverability of the short array and DBML/RBML allow significant suppression of the array ambiguities and increased endfire resolution. Comparing Figure 4.2 with Figures 4.3(b) and 4.3(c), the results show that the usable bearing space of short mobile arrays can approximate that of much larger arrays. Differences in array gain can be addressed by increasing the density of short arrays over the surveillance area or by reducing transmission loss through location (e.g. depth), thus exploiting the maneuverability of the small arrays.

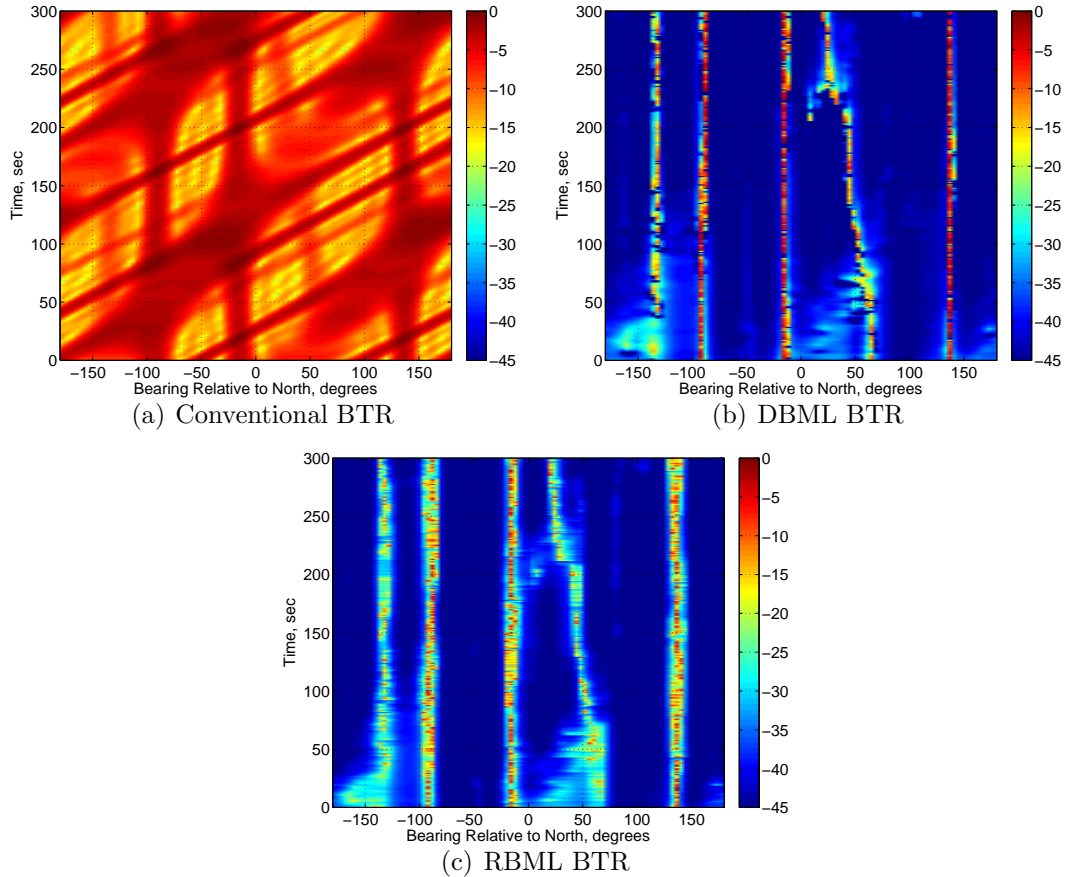


FIGURE 4.3: BTR showing narrowband power estimates, in dB, with a maneuvering short array using (a) conventional beamforming, (b) DBML estimate, and (c) RBML estimate.

### 4.3 Broadband Spatial Spectrum Estimator with Parameter Reduction

While the previous section only considers narrowband sources, this section introduces a broadband estimate and analyzes the effect of temporal spectrum knowledge. Temporal spectral knowledge is incorporated into the model of the broadband signal covariance matrix,  $\bar{\Sigma}$ , and used to reduce the number of parameters to be estimated. In this section, the Cramér-Rao bound (CRB) is derived to demonstrate the utility of data from multiple frequency bins. The multivariate circular symmetric complex normal probability density, for a single snapshot of array data, is assumed to have

covariance  $\mathbf{R}$  and mean  $\boldsymbol{\mu} = \mathbf{0}$ ,

$$f(\mathbf{x}) = \frac{1}{\det(\pi\mathbf{R})} \exp(-\mathbf{x}^H \mathbf{R}^{-1} \mathbf{x}).$$

Consecutive snapshots are assumed to be independent and identically distributed (i.i.d.). The Fisher information matrix,  $\mathbf{J}$ , is well known for the single snapshot case [71]

$$[\mathbf{J}]_{pq} = \text{Tr} \left\{ \bar{\mathbf{R}}^{-1} \frac{\partial \bar{\mathbf{R}}}{\partial \sigma_p^2} \bar{\mathbf{R}}^{-1} \frac{\partial \bar{\mathbf{R}}}{\partial \sigma_q^2} \right\}. \quad (4.26)$$

The bound on the covariance of an unbiased estimator is given by  $\text{cov}([\hat{\boldsymbol{\Sigma}}]_{qq}) \geq [\mathbf{J}^{-1}]_{qq}$  or for the scalar case  $\text{var}(\hat{\sigma}^2) \geq J^{-1}$ . Considering a single frequency at a time then expanding to  $B$  frequencies, the derivative term and inverse are block diagonal resulting in a simple expanded form of the Fisher information matrix,

$$[\mathbf{J}]_{pq} = \sum_{b=1}^B \text{Tr} \left\{ \mathbf{R}^{-1}(\omega_b) \frac{\partial \mathbf{R}(\omega_b)}{\partial \sigma_p^2} \mathbf{R}^{-1}(\omega_b) \frac{\partial \mathbf{R}(\omega_b)}{\partial \sigma_q^2} \right\}. \quad (4.27)$$

The key to this simplification is independence across frequency bins. For a single source, the resulting bound is trivial and independent of source location. The variables  $p$  and  $q$  in (4.27) index the unknown parameters. Traditional frequency-domain techniques estimate power at each frequency then use weighted summation to combine estimates, which requires estimating  $Q \times B$  parameters and then averaging to form the final  $Q$  parameters. This requires estimating the full set of parameters instead of directly estimating the final parameter. The parameter space reduces from  $Q \times B$  to as few as  $Q$  when the source temporal spectrum is known or a single parameter describes each source, such as unknown source level with known shape. Without loss of generality, consider the case when sources are assumed to have a flat spectrum. Typically, processing schemes incoherently average the estimate across

frequencies, resulting in a bound

$$\mathbf{J}_c^{-1} = \frac{1}{B^2} \sum_{b=1}^B \mathbf{J}^{-1}(\omega_b). \quad (4.28)$$

However with a reduced parameterization of the spectrum the derivation bound has a form

$$\mathbf{J}_B^{-1} = \left[ \sum_{b=1}^B \mathbf{J}(\omega_b) \right]^{-1}. \quad (4.29)$$

Refer to Appendix B for derivations of (4.28) and (4.29). The bound in (4.28) will be referred to as the full ML approach since it estimates each parameter then averages across frequency. The bound from (4.29) will be referred to as the reduced ML approach since it performs parameter reduction before estimation. Comparing the full ML approach with the reduced ML case, it can be seen that there will only be a significant difference when  $\mathbf{J}(\omega_b)$  varies between frequencies. For example, consider a 10 element ULA with static source at  $10^\circ$  and 10 dB SNR without spatial aliasing. The CRB of the power estimate of a second source is computed as a function of true bearing in order to explore the impact of angular source separation and bandwidth. Increasing separation quickly decreases the bound, as shown in Figure 4.4. The full and reduced bounds do not show significant differences for 550-750 Hz, however separation of approximately 2 dB occurs with 250-750 Hz. The full method reaches the reduced bound near  $30^\circ$ . It is clear that angular separation and not bandwidth impacts the bound the most in this case [77]. This is because the bound does not have large variations between frequencies in this simple case.

In contrast, spatial aliasing causes large variations in the bound since grating lobes create incorrect power estimates in ambiguous directions. However, grating lobes occur at known frequency dependant locations and can be exploited to reduce uncertainty. Comparing the forms of (4.28) and (4.29), very uncertain parameters

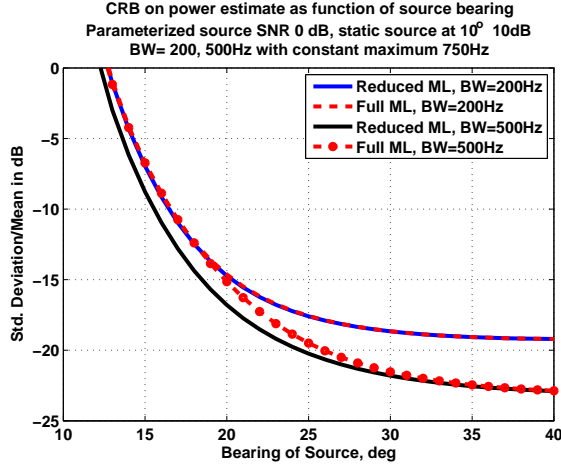


FIGURE 4.4: CRB of power estimate with 10 dB source at  $10^\circ$  as function of second source (0 dB) using 10 element ULA array with half wavelength spacing for various bandwidth without spatial aliasing

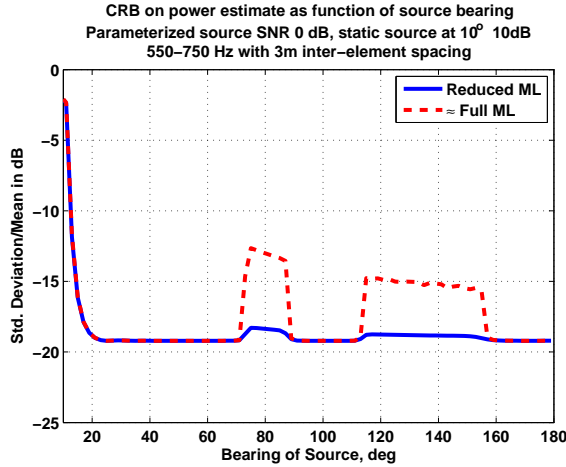


FIGURE 4.5: CRB of power estimate in aliasing region with 10 dB source at  $10^\circ$  as function of second source (0 dB) using 10 element ULA array with  $3\lambda/2$  spacing

will dominate in the full estimate while the reduced estimate is less sensitive to individual parameter uncertainty. Consider the previous example with a 10 element ULA but now with minimum  $3\lambda/2$  spacing over the 500-750 Hz range. This  $\approx 3$  m spacing results in 2 ambiguous regions over  $180^\circ$  which can be seen as jumps in the bound shown in Figure 4.5. The full parameter bound shown in Figure 4.5 uses

an approximation discussed in Appendix B for numerical stability. The reduced parameter bound remains significantly lower than the full method, reducing the impact of spatial aliasing. This motivates incorporating parameter reduction in broadband extensions of the spatial spectrum estimates.

Now the RBML estimate is extended for broadband sources. In order to focus on the broadband effects, the derivations assume the variance of the spatial spectrum is small,  $\mathbf{r}_q = 0$  for  $q = [1, \dots, Q]$ , but any dynamic model can be incorporated resulting in different likelihood functions and priors. The derivation for the RBML estimate in Section 4.1.2 is extended where (4.21) is replaced with expectation step (4.30) defined  $z_B$ ,

$$z_B = -N \sum_{b=1}^B \sum_{q=1}^Q \ln[\boldsymbol{\Sigma}(n, \omega_b)]_{qq} - \sum_{k=n-N+1}^n \left( \sum_{b=1}^B \sum_{q=1}^Q \frac{h_q(k, \omega_b)}{[\boldsymbol{\Sigma}(n, \omega_b)]_{qq}} \right) \quad (4.30)$$

where  $h_q(k, \omega_b) = \text{E} [|s_q(k, \omega_b)|^2 \mid \boldsymbol{\Sigma}^{\text{old}}, \mathbf{X}_n]$ . For simplicity, assume the spectrum is flat such that  $\boldsymbol{\Sigma}(n) = \boldsymbol{\Sigma}(n, \omega_b) \forall b = [1, \dots, B]$ . The estimate is now an optimization directly over  $\boldsymbol{\Sigma}(n)$ , thus a reduced broadband estimate. The maximization step is solved by setting the derivative of (4.30) equal to zero. The maximization step of (4.22) is now replaced by

$$\frac{\partial z_B}{\partial [\boldsymbol{\Sigma}(n)]_{qq}} = \frac{-NB}{[\boldsymbol{\Sigma}(n)]_{qq}} + \sum_{k=n-N+1}^n \sum_{b=1}^B \frac{h_q(k, \omega_b)}{([\boldsymbol{\Sigma}(n)]_{qq})^2}.$$

The reduced broadband estimate results in an estimate over the previous data across all frequencies, has the form

$$[\hat{\boldsymbol{\Sigma}}]_{qq} = \frac{1}{NB} \sum_{k=n-N+1}^n \sum_{b=1}^B \text{E} [|s_q(k, \omega_b)|^2 \mid \hat{\boldsymbol{\Sigma}}^{\text{old}}, \bar{\mathbf{x}}]. \quad (4.31)$$

From (4.31), it appears that multiple frequencies can be combined by averaging the final result, which is the traditional solution [33]. However, the estimate is given

by substituting (4.24) into (4.31), resulting in a solution in matrix form (4.32) that accommodates the parameterization of the temporal spectrum at each iterative,

$$\hat{\Sigma}_n^{\text{new}} = \hat{\Sigma}^{\text{old}} - \hat{\Sigma}^{\text{old}} \frac{1}{NB} \sum_{k=n-N+1}^n \sum_{b=1}^B (\mathbf{G}(n, \omega_b)) \hat{\Sigma}^{\text{old}} \quad (4.32)$$

where the frequency and time dependent terms from the conditional pdf are

$$\mathbf{G}(n, \omega_b) = \left( \mathbf{V}^H (\mathbf{K}^{-1} - \mathbf{K}^{-1} \hat{\mathbf{R}} \mathbf{K}^{-1}) \mathbf{V} \right) \quad (4.33)$$

$$\mathbf{K}(n, \omega_b) = \mathbf{V} \hat{\Sigma}^{\text{old}} \mathbf{V}^H + \sigma_\eta^2 \mathbf{I}. \quad (4.34)$$

In the flat temporal spectra, it is clear that the reduced broadband estimate, (4.32), does not result in simply averaging across frequencies as a post-processing method. Incorporating parameterization of the temporal spectrum knowledge into the estimate forces convergence to a joint solution. In contrast, the traditional full ML estimate, given by (4.35), averages outside of an estimate iteration and expands the space where the solution is allowed to exist then shrinks the space after convergence.

$$\hat{\Sigma}_n = \frac{1}{B} \sum_{b=1}^B \hat{\Sigma}_n(\omega_b) \quad (4.35)$$

#### 4.4 Broadband Simulation with Under-sampled Array

A simulation is used to demonstrate performance differences between a full ML approach, (4.35), and the reduced ML approach, (4.32) with under-sampled arrays subject to spatial aliasing. The simulation from Section 4.2 is extended with true BTR given in Figure 4.1, now over a 550-750 Hz bandwidth with 2 Hz bins and snapshot length of 1 sec. In order to demonstrate the effects of spatial aliasing, the array inter-element spacing is  $3\lambda/2$  for the maximum frequency,  $\approx 3\text{m}$ . For a uniform linear array, it is possible to have as many as 5 additional incorrect ambiguities from

2 grating lobes and a total of 3 backlobes. The clairvoyant circular array is reduced to 220 elements. The SNR is normalized for each array such that post-array gain is held constant as before. Conventional beamforming is used on the unrealisable circular array with incoherent frequency averaging resulting in relatively higher sidelobes, seen in Figure 4.6. The circular array does not suffer, however, from ambiguities due to spatial grating lobes.

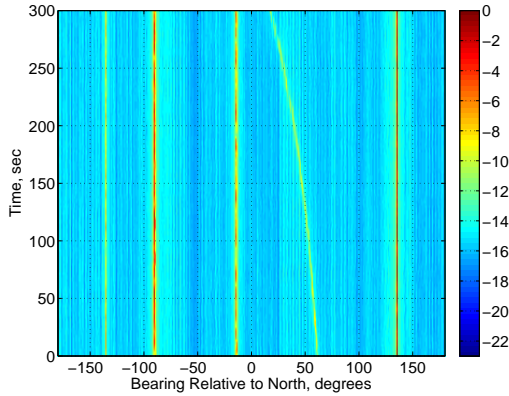


FIGURE 4.6: BTR showing power estimates, in dB, from broadband conventional beamformer output for under-sampled clairvoyant circular array.

A 7 element ULA array maneuvers over the path of the circular array as before. Note the length of the mobile platform is increased by a factor of 3 due to the larger spacing. Using the ULA, conventional beamforming output contains ambiguities as a result of spatial aliasing and array geometry, which vary as a function of platform orientation. This creates structured patterns appearing as maneuvering sources or swirls in the background of the BTR, shown in Figure 4.7(a). The full ML technique estimates the covariance matrix at each frequency, which contains spatial grating lobes, across all time and then averages the estimates across frequencies. This reduces the effects of spatial aliasing but results in sporadic sources appearing in ambiguous regions, as shown in Figure 4.7(b). It is possible to introduce regularization, for example by setting  $r_q$  in (4.23) to a non-zero value and forming a broadband

solution, but this will also reduce the estimated power of high bearing rate sources. A trade-off exists in this case but is not explored here. The reduced ML method provides significant suppression of spatial grating lobes, shown in Figure 4.7(c). The performance improvement from full ML to reduced ML is significant, with only a small ambiguity seen near  $100^\circ$ . There is also improvement from the narrowband case in Figure 4.3(c) to the broadband cases, although an increase in resolution is due to the larger length of the array in the broadband simulation.

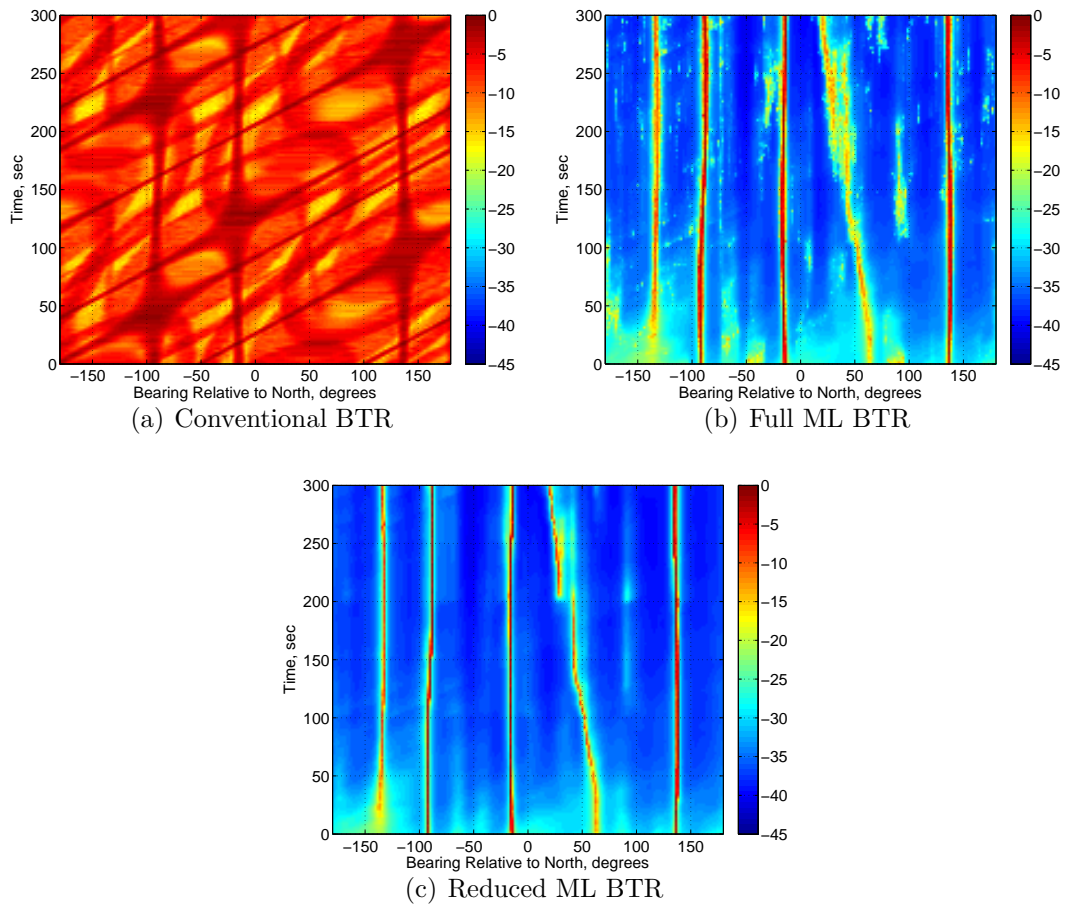


FIGURE 4.7: BTRs showing broadband power estimates, in dB, with an under-sampled maneuvering short array using (a) conventional beamforming, (b) full ML, and (c) reduced ML.

In order to understand the effects of surface wave noise on the field directionality

map estimate, consider the case where the background noise covariance,  $\mathbf{Q}$  instead of  $\sigma_\eta^2 \mathbf{I}$  in (3.8), is generated from noise generated by the ocean surface uniformly with downward directivity given by  $\cos^2(\beta)$ , where  $\beta$  is the angle measured from a downward-facing axis perpendicular to the ocean surface. The resulting spatial correlation of the surface wave noise at the array can be found in closed form in (70) of [78] where  $m = 1$ . For example, consider the case where  $\mathbf{Q} = \sigma_\eta^2 \mathbf{I} + \tilde{\mathbf{Q}}$  such that  $\tilde{\mathbf{Q}}$  is the surface generated noise with diagonal equal to the sensor noise. The resulting BTR has an increased noise floor due to the increased noise level as well as the correlation, as shown in Figure 4.8, but the performance does not otherwise change. Thus, the RBML algorithm is robust to this noise. Additionally, consider robustness to temporal spectrum mismatch. Consider the case where each source only transmits power over the middle 20% of the assumed 550-750 Hz band. Mismatch between the assumed source spectra and the received data, as well as the decrease in total signal energy, results in decreased performance, as shown in Figure 4.9. The algorithm is unable reduce spatial grating lobes to the levels achieved without mismatch by comparing the BTRs shown in Figure 4.7(c) and Figure 4.9. However, each of the five sources are clearly visible even though 80% of the assumed band is missing.

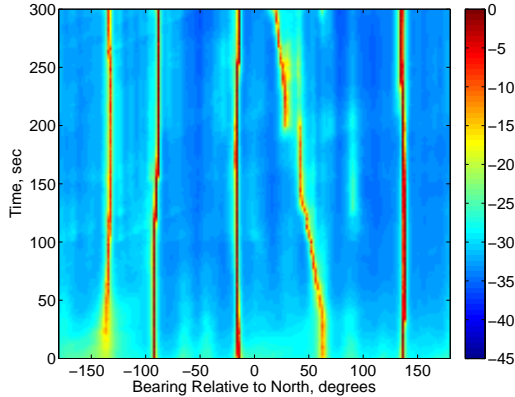


FIGURE 4.8: Broadband BTR demonstrating the performance of the reduced ML technique in the presence of surface wave noise.

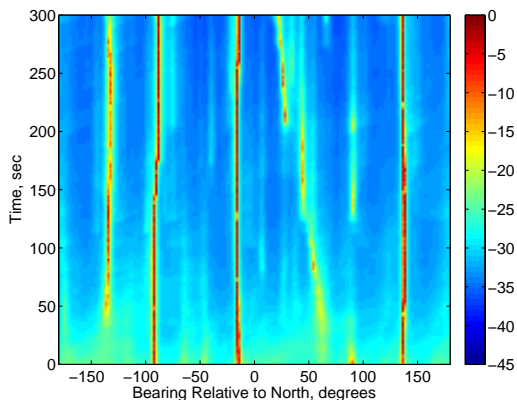


FIGURE 4.9: Broadband BTR using the reduced ML method with mismatched source signals. True source bandwidth 20% of assumed band.

A detection algorithm is used to provide an additional comparison among the different methods in the presence of spatial aliasing without surface noise. This is also used to demonstrate the potential for low SNR target detection using an array mounted on a small UUV. The null hypothesis ( $H_0$ ) is the target-free interference dominated environment, and the alternate hypothesis ( $H_1$ ) is a target with given target track in same environment. Since ambiguities result in false targets that cross the target track, an  $\tilde{M}$ -of- $\tilde{N}$  detector is used that is robust to spurious peaks [79]. Using  $\tilde{N} = 100$  observations of 1 second intervals, a detection occurs when  $\tilde{M} = 80$  or more power (BTR) estimates exceed a given threshold along an assumed target track. The true target track is used and the threshold is varied to determine the receiver operating characteristics (ROC) in terms of probability of detection,  $P_d$ , and probability of false alarm,  $P_f$ . In order to consider low SNR target detection, a target SNR of -25 dB is used, and interference levels are unchanged. Using 100 realizations, the result shown in Figure 4.10. The conventional delay-and-sum beamforming is unable to distinguish the target from the interferers. The full ML method provides some improvement over conventional, but the reduced ML method provides the best performance.

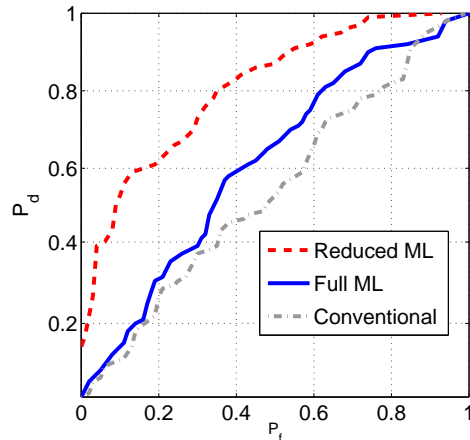


FIGURE 4.10: ROC curve with target SNR -25 dB using  $\tilde{M}$ -of- $\tilde{N}$  detector for under-sampled array

#### 4.5 Water Pulley Array Dynamical Motion Model with Heading Sensor Constraints

The spatial spectrum estimates discussed in Section 4.1 and Section 4.3 require a known array shape. Since a towed hydrophone array is a flexible cable, the array shape is often unknown and must be estimated. Traditional array shape estimation methods based on a deterministic signal model and a known number of sources jointly estimate directions of arrival and array shape. The acoustic field generated from littoral environments may contain heavy shipping traffic that dominates the noise field [80] and may not appear as distinct planewave sources due to the density of vessels in shipping lanes. In this section, the ambient noise field directionality is exploited to estimate the array curvature, and then fused with organic array position estimates. An acoustic based array shape estimate is introduced that exploits the differences in the dynamics of the  $360^\circ$  far-field versus array maneuvers. First, an ML estimate using acoustic data is derived using the array shape model from Section 3.2. This water pulley model works well for wide turns and is combined with heading

sensors to constrain the estimate. In Section 4.6, a method to filter such data using a more general dynamical model is used.

#### 4.5.1 Water Pulley Model Acoustic Estimate

Time dependence for the array shape parameter,  $\boldsymbol{\gamma}(n)$  in (3.13), is denoted with a subscript,  $\boldsymbol{\gamma}_n$ . The size of the moving window is  $N$ , and the array shape is assumed to be constant during the window. The received data at time  $n$  is distributed according to

$$\mathbf{x}(n, \omega) \sim CN(0, \mathbf{V}(\boldsymbol{\gamma}_n, \omega) \boldsymbol{\Sigma}_n \mathbf{V}^H(\boldsymbol{\gamma}_n, \omega) + \sigma_\eta^2 \mathbf{I}).$$

The log-likelihood of the array shape parameters is  $L(\boldsymbol{\gamma}_n) = \ln f(\mathbf{x}(n, \omega) | \boldsymbol{\gamma}_n, \boldsymbol{\Sigma}_n)$  and has the form given by

$$\begin{aligned} L(\boldsymbol{\gamma}_n) = & -\ln \det(\mathbf{V}(\boldsymbol{\gamma}_n, \omega) \boldsymbol{\Sigma}_n \mathbf{V}^H(\boldsymbol{\gamma}_n, \omega) + \sigma_\eta^2 \mathbf{I}) \\ & - \text{tr} \left\{ (\mathbf{V}(\boldsymbol{\gamma}_n, \omega) \boldsymbol{\Sigma}_n \mathbf{V}^H(\boldsymbol{\gamma}_n, \omega) + \sigma_\eta^2 \mathbf{I})^{-1} \hat{\mathbf{R}}_n(\omega) \right\} \end{aligned} \quad (4.36)$$

with leading constants ignored. However, as noted by Varadarajan and Krolik, towed arrays often have heading sensors to assist with array shape estimation and can be incorporated into the estimate as a linear constraint in order to resolve shape ambiguities [47]. A tow-point indicator (TPI) sensor measures the bearing from the towing platform to the sensor array. Given a sensor heading  $\psi_i$ , the constraint is  $\mathbf{b}_i^T \boldsymbol{\gamma} = \psi_i$  where  $\mathbf{b}_i^T$  is the  $i$ th row of basis matrix  $\mathbf{B}$ . The ML estimate has the form

$$\hat{\boldsymbol{\gamma}}_n = \arg \max_{\boldsymbol{\gamma}_n} L(\boldsymbol{\gamma}_n) \text{ subject to } \mathbf{b}_i^T \boldsymbol{\gamma}_n = \psi_i. \quad (4.37)$$

The spatial spectrum estimation work in Sections 4.1 and 4.3 utilize a grid of  $Q$  assumed sources. But traditionally, array shape estimates use a known, smaller number of sources. In order to provide a comparison between the two methods, a traditional method is also formed using the same array shape model. An estimator

based on Weiss and Friedlander's [54] work is introduced using the same array shape model as (4.37). The estimate, assuming the direction of arrivals are known, is given by

$$\hat{\boldsymbol{\gamma}}_{n,\boldsymbol{\theta}} = \arg \max_{\boldsymbol{\gamma}_n} \left( -\ln \text{tr} \left\{ (\mathbf{I} - \mathbf{A}(\boldsymbol{\gamma}_n, \boldsymbol{\theta}_n)[\mathbf{A}(\boldsymbol{\gamma}_n, \boldsymbol{\theta}_n)]^\dagger) \hat{\mathbf{R}}_n \right\} \right) \text{ subject to } \mathbf{b}_i^T \boldsymbol{\gamma}_n = \psi_i \quad (4.38)$$

where  $\boldsymbol{\theta}$  is used to denote angles of each source and  $()^\dagger$  is a pseudo-inverse. The major differences between the estimates in (4.37) and (4.38) is that direction of particular sources must be considered. The estimate based on the field directionality map, or spatial spectrum, in (4.37) is referred to as ML-FDM while the estimate in (4.38) is referred to as ML-DOA. Note that the ML-DOA method assumes the correct number of sources is known while the ML-FDM method uses a dense grid of effective sources. The performance loss is demonstrated with a simple example. The error of an estimate will be defined as

$$\text{ME} = \frac{1}{M} \sum_{m=1}^M \sqrt{(x_m - \hat{x}_m)^2 + (y_m - \hat{y}_m)^2}. \quad (4.39)$$

Consider a 30 element array with half wavelength spacing making a sinusoidal maneuver with known source locations. The source and target tracks shown in Figure 4.11 and the sinusoidal maneuver is shown in Figure 4.12. The platform starts at the origin and is towed East away from a pair of sources. One source starts at (3, 0.75) km and runs South at 5 m/s while the other starts at (4,-1) km and runs North at 5 m/s. The water pulley model is updated at a 10 Hz rate, and the acoustic frequency domain data at 2 Hz. The shape is assumed to be known for the first 40 seconds and then estimated for the remaining time as shown. The sensor heading estimate for a middle array element is shown in Figure 4.12. Note the ML-FDM sometimes lags behind the true heading, which will increase position

error. The error is given in Figure 4.13. The performance loss using the dense grid is easily seen as the error is higher. However, performance gains are possible when the source location is ambiguous or an incorrect number of sources is assumed. This is discussed in the context of a joint estimate as the source parameters must also be estimated.

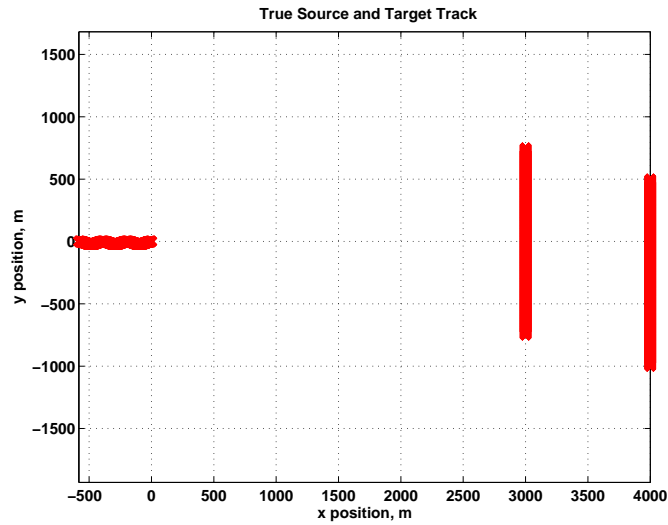


FIGURE 4.11: Source and array track for simulation

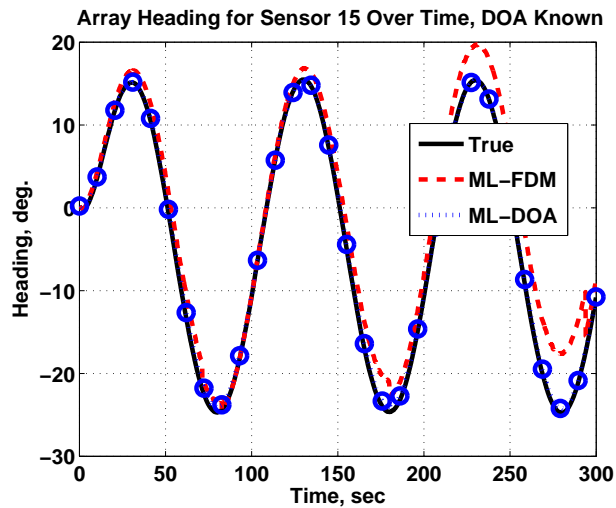


FIGURE 4.12: Sensor heading estimate with known source directions

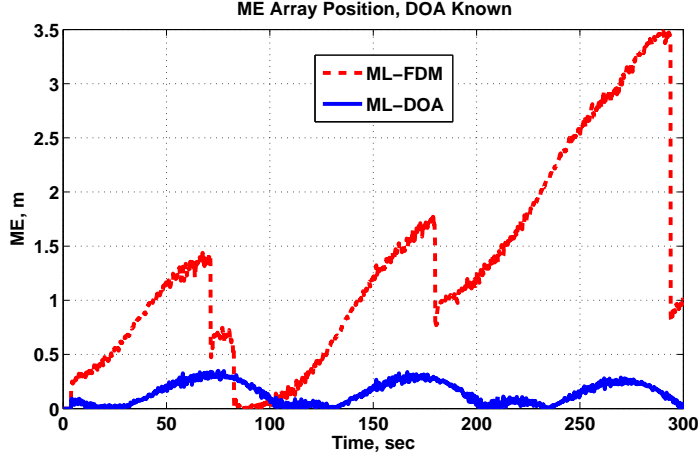


FIGURE 4.13: ME for array position estimate with known source directions

#### 4.5.2 Non-statistical Acoustic and Heading Sensor Fusion

In the passive problem, both source and array parameters must be estimated. This is done by alternating the spatial spectrum estimate with an array shape estimate at each time step. The spatial spectrum estimate  $\hat{\Sigma}_{n-1}$  is used in the log-likelihood (4.36) and estimate (4.37). Similarly, the steering vector  $\mathbf{V}$  in (4.9) will be dependent on  $\hat{\gamma}_n$ . This section will only consider narrowband data. The block diagram of the proposed ML-FDM algorithm is given in Figure 4.14.

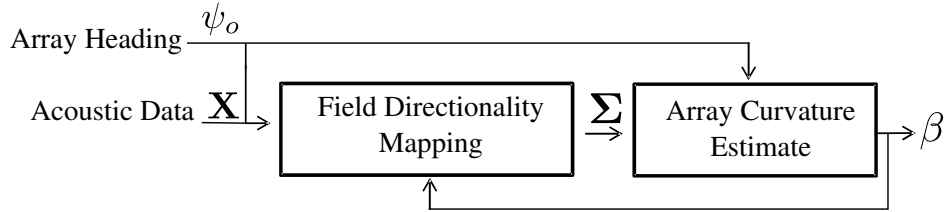


FIGURE 4.14: Block diagram of ML-FDM array shape estimate

The ML-FDM approach is robust to source ambiguities, because the spatial spectrum estimator is able to reduce ambiguities. The ML-FDM algorithm is compared to a method based on the ML-DOA estimate, using a conditional/deterministic signal (CML) approach. For a joint array/source parameter estimate, the ML-DOA

method is based on Goldberg, Weiss, and Friedlander's works [54, 60]. For a deterministic source signal model, the source signal estimate can be written in terms of the other unknown parameters, shown by  $\mathbf{s}$  in (4.40). The joint estimate results in an optimization over both parameter steps, given by (4.41). The block diagram of ML-DOA is shown in Figure 4.15. Note that the blocks are vertical to denote this can be done in a single mathematical step. This may also be done with the ML-FDM estimate but is computationally infeasible due to the larger parameter space when many sources are present.

$$\hat{\mathbf{s}} = \mathbf{A}^\dagger(\boldsymbol{\gamma}_n, \boldsymbol{\theta}_n) \mathbf{X}_n \quad (4.40)$$

$$\hat{\boldsymbol{\gamma}}_n, \hat{\boldsymbol{\theta}} = \arg \max_{\boldsymbol{\gamma}_n, \boldsymbol{\theta}_n} \left( -\ln \text{tr} \left\{ (\mathbf{I} - \mathbf{A}(\boldsymbol{\gamma}_n, \boldsymbol{\theta}_n) [\mathbf{A}(\boldsymbol{\gamma}_n, \boldsymbol{\theta}_n)]^\dagger) \hat{\mathbf{R}}_n \right\} \right) \text{ subject to } \mathbf{b}_i^T \boldsymbol{\gamma}_n = \psi_i \quad (4.41)$$

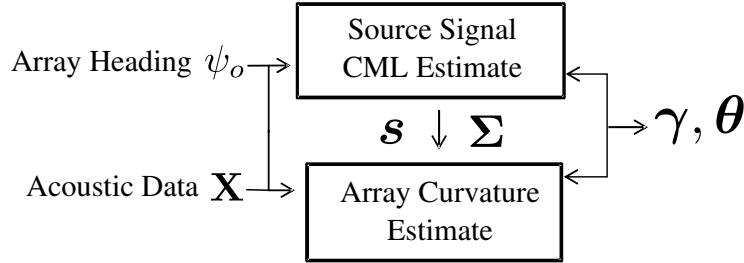


FIGURE 4.15: Block diagram of ML-DOA algorithm

The result of the 5 min simulation for the scenario from Figure 4.11 is shown in Figure 4.16. When the sources reach endfire, at 150 sec and 200 sec, the ML-DOA is unable to find the correct direction of the sources and fails to correctly estimate the array shape. The crossing paths problems is addressed by Goldberg in the form of a tracker [60]. However, Goldberg notes that the algorithm assumes perfect data association for the sources and that source motion must be modeled with enough physical parameters in order to disambiguate. For the simplest case, source bearing

velocity is estimated, Using the ML-FDM approach, this is not needed and allows sources to exist over the full  $360^\circ$ . In this case, the ML-FDM method is able to track the array shape over time. Previous shape estimates in literature assume sources do not have ambiguities given known array shapes, thus sources passing through endfire are ignored.

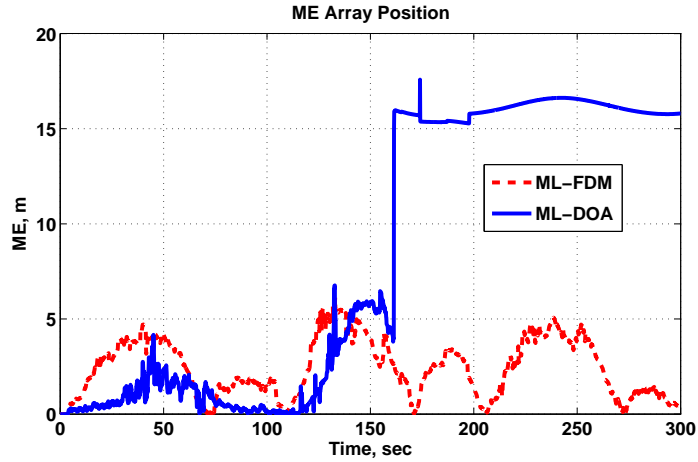


FIGURE 4.16: ME for array position estimate with unknown source directions

Now consider a simpler case where one source passes through endfire but one source does not. This allows for the ML-DOA algorithm to potentially correct itself. The source and array trajectories are shown in Figure 4.17. Again, the signal-to-noise ratio for each source before array gain is 10 dB. The tow platform performs a  $\pm 20^\circ$  sinusoidal maneuver throughout the entire simulation assuming constant forward motion of 2 m/s. A single snapshot of acoustic data collected for each array shape but now sliding window of 10 snapshots with 90% overlap is used to calculate estimates.

Ambiguities due to the linear array geometry cause incorrect direction of arrival estimates and degrade array shape performance for the ML-DOA technique. This can be seen in the example shown in Figure 4.18, where the ML-DOA method fails between 150 and 250 seconds. The ML-FDM method is able to maintain an

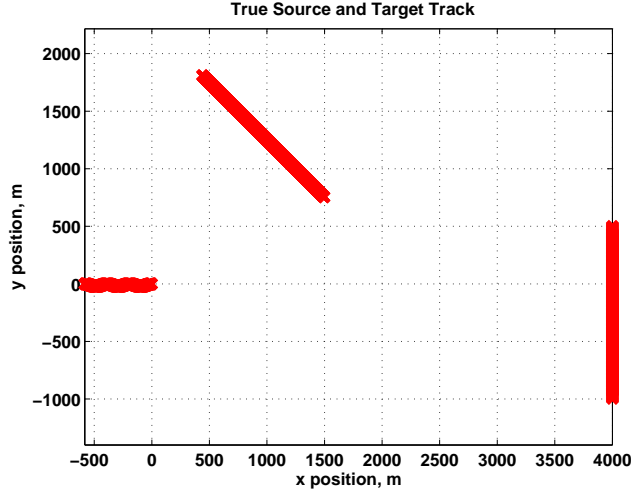


FIGURE 4.17: Source and array track for second simulation

unambiguous field directionality map during the entire maneuver. A Monte Carlo simulation of 100 runs with different signal realizations is used to demonstrate the estimate sensitivity to the received signals with limited snapshot support. The performance is computed by calculating root mean square error of the hydrophones positions across realizations. The ML-DOA method does not always fail at the same time instance, but the average error of the array shape is higher using ML-DOA as compared to ML-FDM over the entire maneuver. This is shown in the empirical cumulative distribution function (CDF) of error across time and realizations combined. The probability of low error for ML-DOA is higher than ML-FDM below the median, where  $F(x)=.5$  in Figure 4.19. However, above the median the ML-FDM shows a significantly higher probability over ML-DOA for the same error threshold. For example, the probability that the RMSE is at most 5 m is 0.9 for ML-FDM but only 0.6 for ML-DOA. In this case, 5 m is  $2.5 \lambda$ . In order to be effective for beamforming, the array shape estimate error must be much lower than a wavelength.

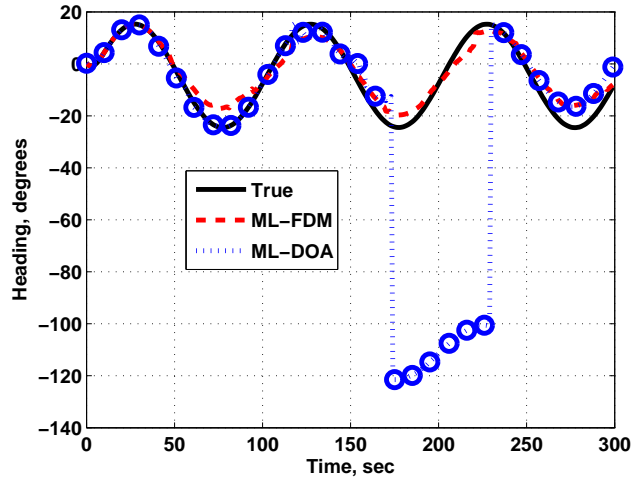


FIGURE 4.18: Array heading estimate for sensor 15

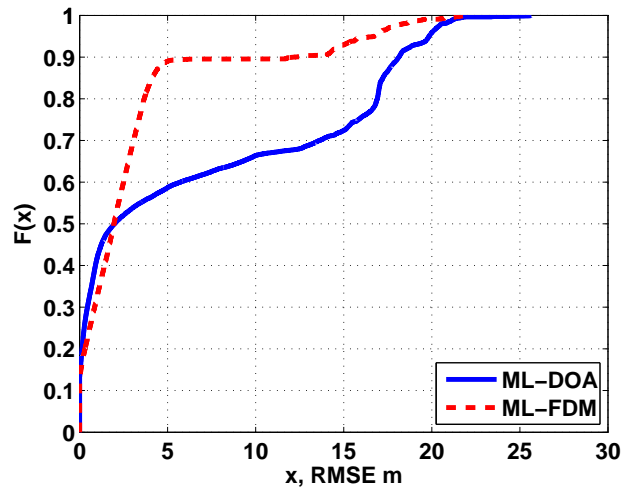


FIGURE 4.19: Empirical cumulative distribution function of RMSE of array shape

#### 4.6 Non-linear Dynamical Motion Model with Statistical Heading Sensor Fusion

The results from the previous section demonstrate that the RBML spatial spectrum estimate can be used in a joint array/source parameter estimate (ML-FDM) instead of direction of arrival estimation (ML-DOA). Note that other spatial spectrum es-

timates can be used to replace the RBML estimate in general. In this section, the joint array/source estimation problem is expanded to a larger class of array shapes and maneuvers. The water pulley model from the previous section is limited to slow turns. Another ML estimate is derived but instead using the array shape model from Section 3.3. This more complicated model works for both wide and sharp turns, and arbitrary array shapes are considered. Additionally, a method to statically fuse acoustic based array shape estimates and heading sensor data is derived in the form of an extended Kalman filter. First, a method to exploit the arbitrary array shape model from Section 3.3 is introduced. The array shape dynamical model is solved discretely in terms of arc length down the tow cable. Linear interpolation is used to relate heading sensor data to the dynamical model. A separate parameterization that is appropriate for acoustic data is used, based on polynomial fitting in heading (unlike Section 4.5 which used an empirical low rank approximation). Finally, a filter is derived to fuse heading data and the acoustic based method. The non-linear relationship between acoustic data and heading as well as the motion normal to the array are treated as second order effects and are ignored for error propagation in the filter.

#### 4.6.1 Parametric Array Shape Approximation

Heading sensors measure the absolute heading from North with additive noise such that the measurements,  $\boldsymbol{\psi}_H$ , are distributed according to  $\boldsymbol{\psi}_{H,n} \sim \mathcal{N}(\mathbf{L}\boldsymbol{\psi}_n, \bar{\mathbf{C}}_n)$ . Heading measurements can be related to the underlying array shape through a piece-wise linear interpolation matrix  $\mathbf{L}$ . Assuming the spatial samples,  $\mathbf{d}$ , have equal spacing given by  $\delta_d$  then the interpolation matrix is given by [81, p. 104]

$$\mathbf{[L]}_{a,b} = \begin{cases} 1 - (g_a - d_b)/\delta_d & \text{if } d_b < g_a < d_{b+1} \\ 1 & \text{if } g_a = g_b \\ 0 & \text{otherwise} \end{cases} \quad (4.42)$$

where  $\mathbf{g}$  contains the heading sensor placements in terms of  $d$ .

Since the tow cable is continuous, array heading typically varies smoothly as a function of distance, and a low-dimensional basis set has been empirically shown to accurately model small turns [47]. Alternatively, the shape of the array has been modeled using a bow parameter, as suggested by Gerstoft *et al.* [17] for heading or GPS data. In this paper, an analytic shape parameterization is given in terms of headings that is particularly amenable to both heading and acoustic data. Consider the polynomial fit given  $p + 1$  samples,  $\psi_p$  at locations  $d_q$ ,

$$\psi_{AL}(d) = \sum_{p'=0}^p L_{p,p'}(d)\psi_{p'} \quad (4.43)$$

where  $L_{p,p'}(d) = \prod_{p^*=0}^p (d - d_{p^*}) / (d_{p'} - d_{p^*})$  for  $(p^* \neq p')$  forms the  $p$ th interpolating polynomial in Lagrange form [81]. The Newton form of (4.43) is thus found by considering the divided differences between sampled points and given by

$$\psi_{Ap}(d) = \sum_{p'=0}^p \beta_{p'} \prod_{p^*=0}^{p'} (d - d_{p^*}) \quad (4.44)$$

where the coefficients,  $\beta$ , represent the divided differences. In matrix form, this can be represented as  $\boldsymbol{\psi}_A = \mathbf{G}\mathbf{b}$  where each row of  $\mathbf{G}$  represents a distinct sample location, each column corresponds to orders of the product in (4.44), and  $\mathbf{b}$  is the vector of parameters (divided differences)  $\beta_{p'}$ . The least squares fit for the basis parameters given arbitrary headings is found using the pseudo-inverse,  $\boldsymbol{\psi}_{LS} = \mathbf{G}^\dagger \boldsymbol{\psi}_A$ .

Without loss of generality, the first divided difference is considered as this approximation is well suited to the array shape problem as will be shown. The heading function is approximated linearly given a heading,  $\psi_o$  at location  $d_o$  such that

$$\psi_A(d) = \psi_o + \beta(d - d_o). \quad (4.45)$$

Note that this formulation avoids the inherent rotational ambiguity of acoustic based shape estimation (see [39]), which is mitigated by at least one given heading,  $\psi_o$ . For the specific case given in (4.45), the basis set for hydrophone locations is written as

$$\mathbf{G} = \begin{bmatrix} 1 & d_1 - d_o \\ 1 & d_2 - d_o \\ \vdots & \vdots \\ 1 & d_M - d_o \end{bmatrix} \quad (4.46)$$

with parameters  $\mathbf{b} = [\psi_o \ \beta]^T$ .

#### 4.6.2 Acoustic Based Array Shape Estimate

First, the joint array curvature and field directionality estimate is derived as an iteration between alternating ML estimates. Second, the array curvature estimate is combined with heading sensor data and filtered with a dynamical model. The block diagram is shown in Figure 4.20. A single heading sensor or GPS data,  $\psi_o$ , provides the absolute heading from North to orient the relative acoustic based shape estimate. The joint array shape and field directionality ML estimate is split into two ML estimates: Array Curvature Estimate with output shape parameter  $\beta$  (passing  $\psi_o$  through the estimate) and Field Directionality Mapping with output  $\Sigma$ . The estimates are calculated once for each acoustic data snapshot. The acoustic based array shape estimate is fused with heading sensor data using a simplified extended Kalman filter. The final array shape estimate heavily weights heading sensor data under non-maneuvering operating conditions but exploits acoustic data from a relatively static but directional field during sharp turns or maneuvers, when heading sensors are less accurate.

#### *Estimation of Array Parameters with Acoustic Data*

The acoustic based array shape estimate is derived as a ML estimate formed by maximizing the probability density function (pdf) of the received acoustic data given

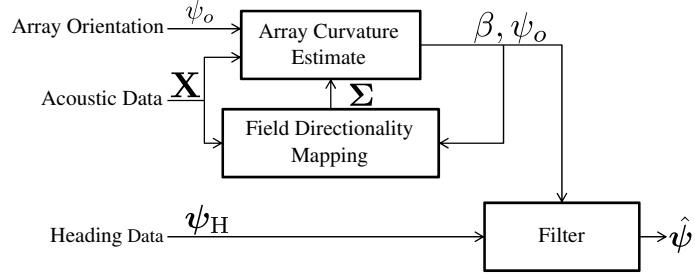


FIGURE 4.20: Block diagram of acoustic and heading data fusion

the unknown bow parameter  $\beta$ , as shown by

$$\hat{\beta}_n = \arg \max_{\beta_n} f(\mathbf{X}_n(\omega) | \beta_n, \Sigma_n). \quad (4.47)$$

Note that  $\Sigma_n$  is unknown and a multidimensional search over source and receiver parameters is computationally infeasible. The problem is divided into two simpler problems: array curvature estimation and field directionality mapping. Consider a sliding window of data  $\mathbf{X}_n(\omega) = [\mathbf{x}_n(\omega) \ \mathbf{x}_{n-1}(\omega) \ \cdots \ \mathbf{x}_{n-N+1}(\omega)]$ . Thus, the problem is separated into two estimation steps for each time instance  $n$ ; the array shape estimate given in (4.48), and the field directionality map shown in (4.49).

$$\hat{\beta}_n = \arg \max_{\beta_n} f(\mathbf{X}_n(\omega) | \Sigma_n \approx \hat{\Sigma}_{n-1}, \beta_n) \quad (4.48)$$

$$\hat{\Sigma}_n = \arg \max_{\Sigma_n} f(\mathbf{X}_n(\omega) | \Sigma_n, \beta_n \approx \hat{\beta}_n) \quad (4.49)$$

The joint estimate iterates between the individual ML estimates (4.48) and (4.49) and will be referred to as the ML-FDM estimate where FDM refers to the field directionality map, in the same way as the ML-FDM solution from Figure 4.14. The log-likelihood of the array shape parameter, of the same form as (4.36), using the

stochastic source model is given by

$$\begin{aligned} \ln f(\mathbf{X}_n(\omega)|\beta_n, \hat{\Sigma}_{n-1}) &= -\ln \det \left( \mathbf{V}(\beta_n, \omega) \hat{\Sigma}_{n-1} \mathbf{V}^H(\beta_n, \omega) + \sigma^2 \mathbf{I} \right) \\ &\quad - \text{tr} \left( \left( \mathbf{V}(\beta_n, \omega) \hat{\Sigma}_{n-1} \mathbf{V}^H(\beta_n, \omega) + \sigma^2 \mathbf{I} \right)^{-1} \hat{\mathbf{R}}_n(\omega) \right). \end{aligned} \quad (4.50)$$

where leading constants have been ignored. Note that solving (4.48) using (4.50) requires a straight forward single parameter non-linear optimization. The search space can be constrained based on the previous shape and platform size.

For broadband data, each frequency bin is assumed to be uncorrelated such that the broadband likelihood function is a sum of narrowband likelihood functions, (4.50). The spatial spectrum is assumed to be temporally flat such that  $\Sigma_n = \Sigma_n(\omega) \forall \omega$  although spectral mismatch mismatch is tolerated. The method given in Section 4.3 referred to as RBML (4.49). This method provides a sequence of field directionality maps that accounts for the time-varying array shape using the expectation-maximization algorithm. In this broadband case,  $\ln f(\bar{\mathbf{X}}|\beta_n, \hat{\Sigma}_{n-1}) = \sum_{b=1}^B \ln f(\mathbf{X}_n(\omega_b)|\beta_n, \hat{\Sigma}_{n-1})$ .

#### *Acoustic and Heading Sensor Statistical Fusion*

Typically, towed arrays have heading and depth sensors to provide array shape estimates. Heading and acoustic sensor fusion forms a single shape estimate that is robust to temporary or permanent heading sensor failure. The heading and acoustic shape estimates are combined and filter in the framework of an extended Kalman filter. Data fusion is accomplished by considering the heading sensor and acoustic based estimates as measurements of the same physical system and filtering using a dynamical motion model.

Let the measurement equation be defined by stacking heading and acoustic based data and corresponding transformations, (4.42) and (4.46), from the state vector of

headings,  $\boldsymbol{\psi}$ , as

$$\begin{bmatrix} \boldsymbol{\psi}_{H,n} \\ \mathbf{b}_n \end{bmatrix} = \begin{bmatrix} \mathbf{L} \\ \mathbf{G}^\dagger \end{bmatrix} \boldsymbol{\psi}_n + \begin{bmatrix} \bar{\mathbf{v}}_n \\ \tilde{\mathbf{v}}_n \end{bmatrix} \quad (4.51)$$

or more compactly by letting  $\mathbf{z}_n = [\boldsymbol{\psi}_{A,n}^\top \mathbf{b}_n^\top]^\top$  such that

$$\mathbf{z}_n = \mathbf{H}\boldsymbol{\psi}_n + \mathbf{v}_n. \quad (4.52)$$

where  $\mathbf{H} = [\mathbf{L}^\top (\mathbf{G}^\dagger)^\top]^\top$  and  $\mathbf{v}_n \sim \mathcal{N}(\mathbf{0}, \mathbf{C}_n)$ ,  $\mathbf{C}_n = \text{diag}(\bar{\mathbf{C}}_n, \tilde{\mathbf{C}}_n)$ . The non-linear state update, where the solution to (3.15) is denoted by  $F(\boldsymbol{\psi})$ , with additive white normal process noise,  $\mathbf{w}_n \sim \mathcal{N}(\mathbf{0}, \mathbf{Q}_n)$ , is written as

$$\boldsymbol{\psi}_n = F(\boldsymbol{\psi}_{n-1}) + \mathbf{w}_n. \quad (4.53)$$

The extended Kalman filter uses the non-linear function,  $F$ , to predict state updates but approximates error prediction via Taylor series expansion expressed as  $\mathbf{F}_n = \partial F(\boldsymbol{\psi})/\partial \boldsymbol{\psi}$  evaluated at  $\boldsymbol{\psi} = \boldsymbol{\psi}_n$ . Using (4.51)-(4.53), the extended Kalman filter equations are summarized as

$$\begin{aligned} \hat{\boldsymbol{\psi}}_{n|n-1} &= F(\boldsymbol{\psi}_{n-1|n-1}) \\ \mathbf{S}_{n|n-1} &= \mathbf{F}_n \mathbf{S}_{n-1|n-1} \mathbf{F}_n^\top + \hat{\mathbf{C}}_n \\ \mathbf{K}_n &= \mathbf{S}_{n|n-1} \mathbf{H}^\top (\mathbf{H} \mathbf{S}_{n|n-1} \mathbf{H}^\top + \hat{\mathbf{Q}}_n)^{-1} \\ \hat{\boldsymbol{\psi}}_{n|n} &= \hat{\boldsymbol{\psi}}_{n|n-1} + \mathbf{K}_n (\mathbf{z}_n - \mathbf{H} \hat{\boldsymbol{\psi}}_{n|n-1}) \\ \mathbf{S} &= (\mathbf{I} - \mathbf{K}_n \mathbf{F}_n) \mathbf{S}_{n|n-1} \end{aligned} \quad (4.54)$$

Note that the state update is non-linear and accounts for the motion of the tow system sliding through the water while not relying on a small angle approximation. Tangential and normal motion dependence on heading are not considered for error propagation for simplicity since the spatial derivative of tangential velocity appears as a first-order effect and tangential velocity is expected to dominate normal velocity. That is the tow cable is pulled from a single end and not the middle of the cable. As

shown in (3.16), the state update equation is linear with respect to heading when this dependency is neglected. Using (3.16), the derivative of the state update equation is given by

$$\mathbf{F}_n \approx \mathbf{I} + \delta_t \mathbf{D}_s \mathbf{U}. \quad (4.55)$$

Additionally, note that the measurement and process covariance matrix must be estimated. While the measurement noise can be estimated from the data,  $\mathbf{z}_n$ , the process noise is typically assumed known or selected a priori. However for the case of towed arrays, navigation from the tow platform can be exploited. The planned maneuver, in terms of heading  $\psi$ , is used to estimate the process noise. A first order auto-regressive model, with parameter  $\gamma$ , is used to estimate the variance in Cartesian space to avoid wrapping in angle space, given by the following equations.

$$\mu_n^x = (1 - \gamma)\mu_{n-1}^x + \gamma \cos(\psi_n) \quad (4.56)$$

$$\mu_n^y = (1 - \gamma)\mu_{n-1}^y + \gamma \sin(\psi_n) \quad (4.57)$$

$$\hat{\varepsilon}_n^2 = (1 - \gamma)\hat{\varepsilon}_{n-1}^2 + \gamma ((\cos(\psi_n) - \mu_n^x)^2 + (\sin(\psi_n) - \mu_n^y)^2) \quad (4.58)$$

Thus the estimate of the process noise is given by  $\hat{\mathbf{Q}}_n = \hat{\varepsilon}_n^2 \mathbf{I}$ . Similarly, the measurement noise,  $\hat{\mathbf{C}}_n$  is estimated from data,  $\mathbf{z}_n$ , where each data element is assumed to be independent but, unlike process noise, not identically distributed.

#### 4.6.3 Performance Bounds

The Cramér-Rao Lower Bound (CRLB) of acoustic based array shape estimation is considered to demonstrate the performance limits as a function of a known field directionality. Unlike previous derivations (i.e. [44, 65, 82]), the bound is derived assuming inter-element spacing on a flexible cable is known, as such is the case for towed arrays. A direct derivation for the bound in terms of headings is given in [83]. Here the bound is given in terms of the polynomial approximation of headings and all derivatives are given in analytic, closed form. The bound is computed using the

Fisher information matrix given by

$$[\mathbf{J}]_{a,b} = N \text{tr} \left\{ \mathbf{R}(\mathbf{b})^{-1} \frac{\partial \mathbf{R}(\mathbf{b})}{\partial \beta_a} \mathbf{R}^{-1}(\mathbf{b}) \frac{\partial \mathbf{R}(\mathbf{b})}{\partial \beta_b} \right\}.$$

The exact Fisher information matrix assuming the environment is known can be computed given the derivative

$$\frac{\partial \mathbf{R}(\mathbf{b})}{\partial \beta_a} = \frac{\partial \mathbf{A}(\mathbf{b})}{\partial \beta_a} \mathbf{\Sigma} \mathbf{A}^H(\mathbf{b}) + \mathbf{A}(\mathbf{b}) \mathbf{\Sigma} \frac{\partial \mathbf{A}^H(\mathbf{b})}{\partial \beta_a}$$

where

$$\frac{[\partial \mathbf{A}(\mathbf{b})]_{m,q}}{\partial \beta_a} = [\mathbf{A}(\mathbf{b})]_{m,q} \frac{\partial(-j\mathbf{k}^T(\theta_q)\mathbf{r}_m(\mathbf{b}))}{\partial \beta_a} \quad (4.59)$$

with compact notation such that (4.59) can be written as  $\mathbf{A}(\beta) \odot \dot{\mathbf{A}}$  with the Hadamard product. However, the array shape model defined by (4.45) couples the rows of the steering matrix,  $\mathbf{A}$ , via  $\beta_a$  such that

$$[\dot{\mathbf{A}}]_{m,q} = -j \frac{\omega}{c} \left( \frac{\partial x_m}{\partial \beta_a} \cos(\theta_q) + \frac{\partial y_m}{\partial \beta_a} \sin(\theta_q) \right) \quad (4.60)$$

where

$$\frac{\partial x_m}{\partial \beta_a} = - \sum_{m'=2}^m \left[ (d_{m'} - d_{m'-1}) \sin \left( \sum_{p'=0}^p \beta_{p'} \prod_{p^*=0}^{p'} (d_{m'} - d_{p^*}) \right) \sum_{p'=a}^p \prod_{p^*=0}^{p'} (d_{m'} - d_{p^*}) \right]$$

and the  $y$ -axis derivative of the same form with  $\cos$  replacing  $-\sin$ . The variance of the estimate is bounded by the inverse of the Fisher information matrix such that

$$\text{var}(\hat{\beta}_p) \geq [\mathbf{J}^{-1}]_{p,p}. \quad (4.61)$$

Consider an array with  $M = 40$  elements at half-wavelength (2.5m) spacing using a linear approximation assuming the heading at the center of the array is known. The CRLB of the array curvature,  $\beta$ , as a function of the number of equal spaced

sources, over  $180^\circ$ , for an array curvature with  $\beta = .23^\circ$  is shown in Figure 4.21 in terms of root-mean-square-error (RMSE). In this case with  $\psi_o = 0$  from (4.45), the maximum difference along the  $y$ -axis,  $\max(|y_a - y_b|)$ , is equal to a wavelength. The bound decreases with an increasing number of sources due to increased total SNR. However, it should be noted that the bound quickly decreases with received single source SNR. While a field of many sources with identical SNR levels is unlikely, Figure 4.21 shows the typical levels where acoustic data may be used supplement noisy heading data. When heading sensor noise exceeds  $0.1^\circ$  RMSE, then acoustic based techniques may provide improved array shape estimates. The CRLB for a

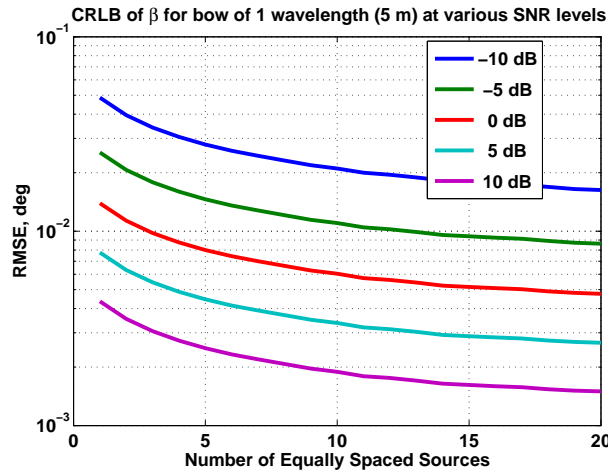


FIGURE 4.21: CRLB of  $\beta$ , for  $\beta = .23^\circ$  such that difference in  $y$  is equal to a wavelength of 5m, as a function of the number of sources with the same SNR around  $180^\circ$  for various SNR levels

wider range of sources is shown on a logarithmic scale in Figure 4.22. The bound begins to increase with more than 30 sources in the field. Thus, the ability to estimate the array shape is a function of the directionality of the field. Note the bound has a plateau effect regardless of SNR. The number of degrees of freedom for source separation is equal to the number of hydrophones, which is 40. Thus as the number of sources approaches the number of hydrophones, the CRLB of  $\beta$  starts to degrade. As a field begins to appear isotropic in terms of a beamformer with limited

resolution, the ability to estimate array curvature diminishes.

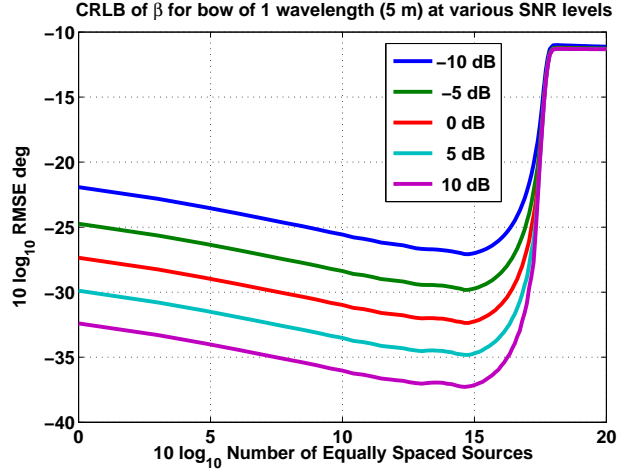


FIGURE 4.22: CRLB of  $\beta$ , for  $\beta = .23^\circ$  such that difference in  $y$  is equal to a wavelength of 5m, for an extended number of sources on a logarithmic scale with the same SNR around  $180^\circ$  for various SNR levels

#### 4.6.4 Simulation Results

Numerical simulation of a multi-source environment with a maneuvering platform is used to demonstrate acoustic based array shape estimation and heading sensor fusion. A 40 element array uniformly spaced at a half wavelength (2.5 m) is assumed to be towed 100 m behind a maneuvering platform. The total length of the cable is 197.5 m long. The tow platform initially heads North ( $0^\circ$ ) and performs a sharp  $90^\circ$  turn towards East ( $90^\circ$ ) with constant forward velocity of 4m/s. The dynamical motion model of Section 3.3 is used to simulate array shape data with 32 equally spaced spatial samples. The bearing at the front and aft (rear) of the tow cable is shown in Figure 4.23 without process noise. The effects of the array shape model can be seen in the differences between the front and aft heading sensors as the tail of the tow cable does not execute the same sharp turn that occurs at the front of the tow cable. Since acoustic data is only collected at the array, the shape of tow cable not containing the array is ignored for acoustic based shape estimation. However,

the entire tow cable is considered when generating the simulated shape data.

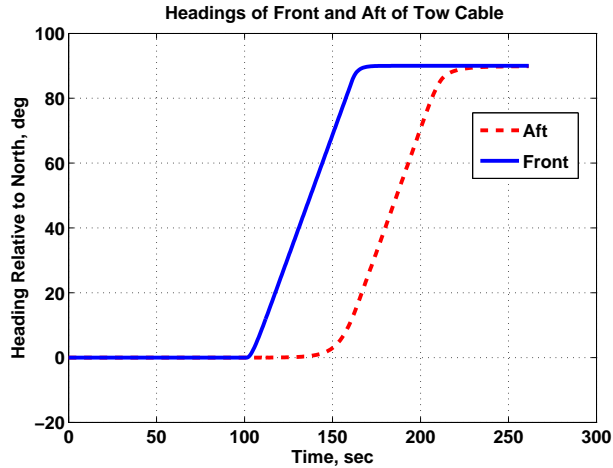


FIGURE 4.23: Headings at head and tail of the tow cable during maneuver

For acoustic based estimation, assume the heading at the middle of the array is measured with additive noise (std. dev.  $0.5^\circ$ ), and process noise along the entire array is  $\mathbf{Q} = (0.05^\circ)^2 \mathbf{I}$  such that the std. dev. of the process noise is a tenth of the measurement noise. Received acoustic data is simulated using four far-field sources (5 dB SNR,  $[\Sigma]_{q,q}/\sigma^2$ ) with bearings uniformly (randomly) distributed over  $360^\circ$ . The acoustic based estimate generated by (4.48) is referred to as ML-FDM. For comparison, the conventional ML estimate that jointly estimates the array shape and source directions of arrival (DOA) as derived by Weiss and Friedlander [54] is referred to as ML-DOA. For a fair comparison to the best case ML-DOA performance, the number of sources is assumed known, and the algorithm is initialized by the true source estimates. The ML-FDM algorithm is set to  $Q = 180$  grid points for the noise field, sampled every  $2^\circ$ , and is initialized with a uniform noise field level of 0 dB. Also, the linear heading approximation (4.45) was implemented for both acoustic array shape estimates. A single snapshot of acoustic data over 290-300 Hz with 2 Hz bins is generated for each physical location, updated every 0.5 s, and a sliding window of five snapshots is used to estimate the covariance matrix. Since the FDM

technique used in ML-FDM accounts for time-varying array shapes, the previous  $N = 10$  time intervals are used to estimate the FDM.

First consider a single realization of array shape estimate. The shape estimates are shown at various time points in Figure 4.24. Note that at 150 s the ML-DOA algorithm incorrectly estimates a curvature that is symmetrical to the true shape, which is a result of the left/right ambiguity inherent in the ML-DOA formulation. The ML-DOA algorithm was formulated for sources over an unambiguous  $180^\circ$ , while the ML-FDM technique considers the full  $360^\circ$  field by exploiting array orientation and shape changes.

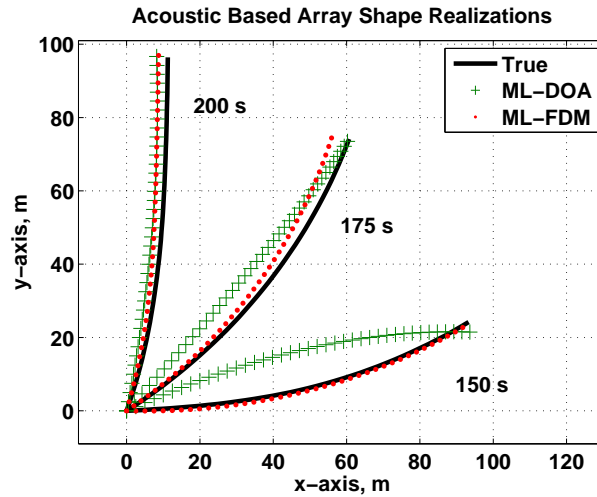


FIGURE 4.24: Acoustic based array shape estimates at various times for a single realization

Consider the case where heading sensors are placed at the front and rear of the array as well as at the tow point on the tow-ship. Initially, each heading sensor has a standard deviation of  $0.5^\circ$ . Heading sensors on the array are greatly affected by the tow forces through the water. The variances of the heading sensors given in [50] are implemented to simulate heading sensor noise during a maneuver, where at the peak of the turn the standard deviation is  $20^\circ$ . The heading sensor at the front of the array is 100 m behind the tow-ship, and the rear sensor is 197.5 m behind the

tow-ship. The heading measured at the tow-ship maintains a constant  $0.5^\circ$  standard deviation because it is not subject to the forces that dramatically increase variance. The same  $90^\circ$  turn is performed as described in Figure 4.23. The state vector used for filtering is 12 equally spaced samples. Note that the filter uses a lower order model than the generative process with 32 samples. When the dynamical models are perfectly matched and process noise is much less than the heading sensor noise, tow ship heading data alone provides sufficient data for highly accurate shape estimation. In this case, diagonal loading of  $\hat{\mathbf{C}}$  in (4.54) can be used to rely heavily on the model. The array shape calculated by filtering only the heading sensor data compared with the fused/filtered heading and acoustic data is shown for various time points in Figure 4.25. The fused estimate is able to more closely follow the true array shape during the turn but estimates are similar at the end of the turn.

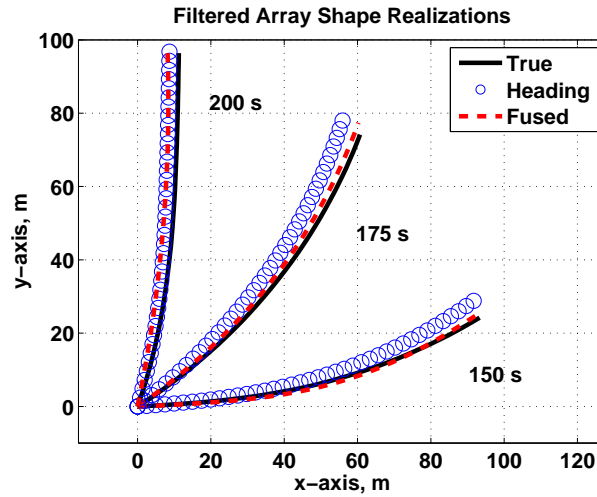


FIGURE 4.25: Filtered array shape estimates using heading data and both heading and acoustic estimates fused at various times for a single realization

The RMSE is calculated over 100 Monte Carlo realizations and across hydrophones in terms of  $(x,y)$  position. Using uniformly distributed source locations in bearing, the RMSE is given as a function of time and normalized by a wavelength in Figure 4.26. The acoustic based estimates (ML-FDM and ML-DOA) have a higher

nominal error level. During the turn from 150 s to 200 s, the performance of traditional and proposed estimation schemes separate. As heading sensors are corrupted with high noise levels, the heading data RMSE increases dramatically. The increase in RMSE for the ML-DOA is primarily driven by outliers that result from incorrect shape estimates due to ambiguities, such as those in Figure 4.24, which occur in 12% of the realizations. For ML-FDM, the relative shape of the array is unaffected by heading sensor failure, and the algorithm is able to disambiguate the field. The fused and filtered estimate has low RMSE outside of the turn by relying on heading sensors and maintains low error during the turn by exploiting the ML-FDM acoustic estimate. The proposed estimate allows smooth transitioning between acoustic and heading data. Note that the array shape can be estimated even if many heading sensors permanently fail, especially sensors at the front of the array or tow cable that are most susceptible.

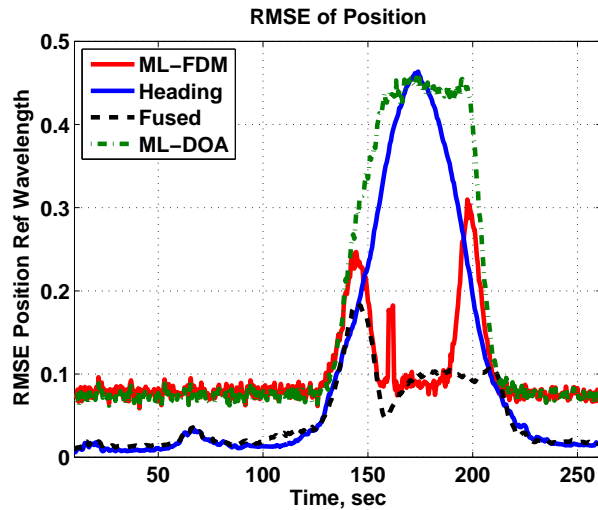


FIGURE 4.26: RMSE of hydrophone position using heading and/or acoustic data from four (5 dB) sources uniformly distributed in bearing during maneuver

The empirical cumulative distribution function (CDF) of position error is used to quantify performance and is less sensitive to outliers than RMSE. The ideal performance, in terms of CDF, is low error with high probability that results in a curve

with an elbow in the top left corner of the plot. In general, a higher curve is better and results in higher probability of lower error. Since filtered heading data is more accurate in straight tow conditions, heading data results in a lower median than acoustic data, shown by  $F(x)=0.5$  in Figure 4.27. However, heading data is inaccurate during the turn and the resulting error distribution has a heavy tail. Both acoustic based estimates have a higher median error but greater ability to estimate shape during a turn. Note that the ML-DOA and ML-FDM error distributions are similar but separate after 0.2 wavelengths, which denotes ML-FDM is more robust. Most significantly, the fused estimate shows higher probability of lower error than any of the individual estimates. Specifically, the 90th percentile of the error as a percentage of a wavelength is 30% for the filtered heading estimate, 19% for ML-DOA, 17% for ML-FDM, and 10% for the combined, filtered estimate.

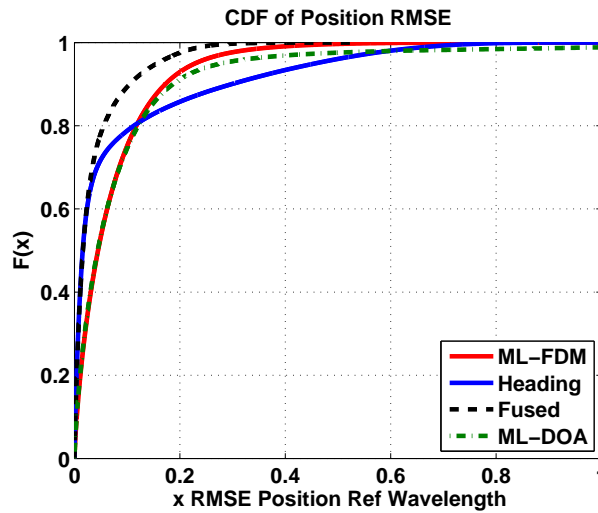


FIGURE 4.27: Cumulative distribution function of position error, relative to a wavelength, across hydrophone, maneuver time, and realizations

Finally, the shape estimation errors using the acoustic data is considered to better understand performance limitations. Distinctive peaks appear in the RMSE plots, in Figure 4.26 as the turn reaches the array in time 120 s and at the end of the turn at 200 s. The cause of this error is the inability of a linear heading model to fit the

shape of the true array. The RMSE of hydrophone heading as a function of time and hydrophone for the ML-FDM estimate is shown in Figure 4.28. Note that the error peaks at the times of the turn transitions and at the far ends of the array. Since the measured heading at the middle of the array is used in the model, the error is least in the middle. The dynamical motion model captures the bend of a tow cable travelling along the array, which is most significant during maneuver start and end times, but linear heading model cannot capture this shape. A higher order polynomial fit will reduce this error but results in a bias/variance trade-off. The array shape model used here could fuse additional shape measurement techniques (i.e. bend or relative heading sensor) to reduce these effects.

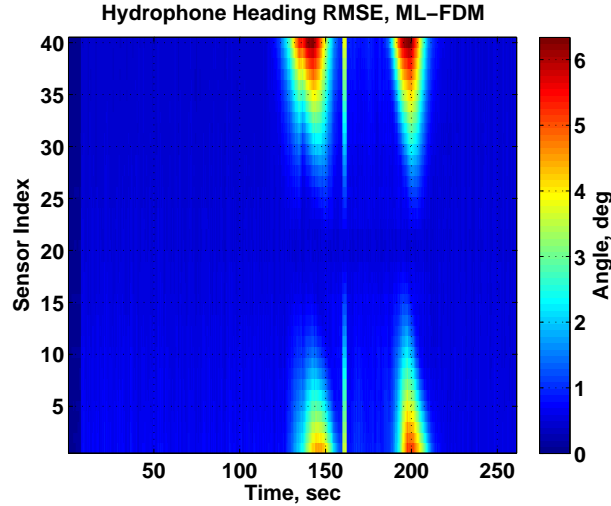


FIGURE 4.28: RMSE of hydrophone headings using ML-FDM shape estimate across realizations as a function of simulation time

## 4.7 Conclusion

A method to estimate towed array shape using acoustic data was introduced in this chapter using a heading polynomial approximation and noise field directionality mapping. Instead of using discrete planewaves and a deterministic signal model, the solution is formed using a stochastic noise field model that captures discrete and dis-

tributed sources. The array shape and field are estimated jointly in order to consider a maneuvering tow platform. The acoustic based solution is fused with external array shape data, such as heading sensors. A dynamical motion model and filter from the literature is exploited to fuse the data without using a small angle approximation and includes array motion perpendicular to tow heading. The combined estimate uses heading data when the heading sensors are operating normally and exploits hydrophone data during sharp turns when heading sensors fail. Such a solution is also applicable for systems that experience permanent heading sensor failure. For the case of working noisy heading sensors, it is possible that the vibrations that disrupt heading sensors may also introduce acoustic noise in hydrophones resulting in a reduction in acoustic SNR over a given band. In the limiting case where acoustic noise severely limits acoustic based array shape estimation, subsequent acoustic processing, such as beamforming, may not be useful regardless of array shape estimation.

## Under-sampled Arrays with Limited Data

The remainder of this document will focus on a particular sub-set of linear under-sampled arrays known as augmentable arrays. The towed array work in Chapter 4 considers array manifold ambiguities due to left/right symmetry and spatial aliasing. Left/right ambiguities exist for all linear geometries, as a cone shown in Figure 2.2, regardless of inter-element spacing, but spatial aliasing is limited to uniformly spaced arrays. In this chapter, additional ambiguities for linear arrays are considered and reviewed. My previous work has described the ability to reduce ambiguities by using incoherent data from different array configurations and incorporating temporal frequency domain knowledge. This chapter focuses on ambiguities in signal or interference subspaces due to non-uniform spatial sampling for static arrays. The formal definition of the array manifold is given and source spatial spectrum identifiability is discussed based on previous literature. The application of partially adaptive processing is introduced for non-uniformly sampled arrays. This is shown to significantly enhance array gain when the number of data snapshots is limited.

It is important to note that only fully augmentable arrays, described later, are considered in this work. This significantly limits the scope of the problem. Various

methods have been proposed for partially augmentable arrays (see [84–86]), but are not considered here.

## 5.1 Mathematical Background

The basic array processing principles for augmentable arrays are reviewed in this section. The problem setup draws from Van Trees’s comprehensive book [5], a book by Johnson and Dudgeon [87], and work by Manikas and Dowlet [88].

The narrowband frequency domain model for the data, rewritten in (5.1), is a function of the source wavenumber  $\mathbf{k}$  received by the  $m$ th element at location  $\mathbf{r}_m$ . For convenience,  $\mathbf{k}$  is also restated below. This model is reexamined to motivate various types of linear array configurations.

$$x_m(\mathbf{k}, \mathbf{r}_m) = se^{-j\mathbf{k}^T\mathbf{r}_m} \quad (5.1)$$

$$\mathbf{k} = \frac{\omega}{c} \begin{bmatrix} \cos \theta \sin \phi \\ \sin \theta \sin \phi \\ \cos \phi \end{bmatrix}$$

The vector used to model propagation for a source with wavenumber  $\mathbf{k}$  at  $M$  sensor locations is given by

$$\mathbf{a} = \begin{bmatrix} e^{-j\mathbf{k}^T\mathbf{r}_1} \\ e^{-j\mathbf{k}^T\mathbf{r}_2} \\ \vdots \\ e^{-j\mathbf{k}^T\mathbf{r}_M} \end{bmatrix}, \quad (5.2)$$

as was used in (3.2). The vector  $\mathbf{a}$  defines an array manifold vector while the array manifold is defined formally as  $\mathcal{A} = \mathbf{a}(\tilde{\mathbf{k}}) \forall \tilde{\mathbf{k}} \in \Theta$ , where  $\Theta$  represents all possible wavefront vectors. The array manifold is important for spatial spectrum estimation; for example, limiting sources to physically feasible positions provides performance increases in Chapter 4. The array manifold spans a subspace of the  $M$ -dimensional

complex space  $\mathfrak{C}^M$ . For example in  $x$ - $y$  space and far-field scenarios in homogeneous fields, only  $\tilde{\mathbf{k}} = \mathbf{k}(\theta)$  is considered such that  $\Theta$  is bounded, where  $0 \leq \theta < 360$ .

### 5.1.1 Uniform Linear Arrays

The array manifold is a function of the spatial sampling method, such as discrete sensor locations and individual sensor type. Assuming far-field sources, a uniform linear array (ULA) of omni-directional sensors with spacing  $d$ , consider a homogeneous (constant propagation speed) field modeled using only a single spatial variable, where  $\mathbf{r}$  has exactly one non-zero component. In other words, the coordinate system is defined such that the array exists on a single axis. Assume the spatial dimension is parameterized by  $k_x$ , where  $k_x = \frac{\omega}{c} \cos(\theta) \sin(\phi)$ . The array manifold vector is then given for an array with center at the origin as

$$\mathbf{a}(k_x) = \left[ e^{-j(\frac{M-1}{2})k_x d} \quad e^{-j(\frac{M-1}{2}-1)k_x d} \quad \dots \quad e^{j\frac{M-1}{2}k_x d} \right]^T. \quad (5.3)$$

Note that the vector contains conjugate pairs. The wavenumber response, or beam-pattern in  $k_x$ , is used to determine the response as a function of wavenumber given a set of weights. This is defined for fixed weights  $\mathbf{w}$ .

$$\begin{aligned} b(k_x) &= \mathbf{w}^H \mathbf{a}(k_x) \\ &= e^{j\frac{M-1}{2}k_x d} \sum_{m=0}^{M-1} w_m^* e^{-jm k_x d} \end{aligned} \quad (5.4)$$

From (5.4) it can be seen that the transform of the weights is periodic with a period  $0 \leq k_x d < \pi$ , also known as the visible region. Typically, the weights are a function of the steering vector, which is an array manifold vector parameterized by the assumed source location. Additionally, windows can be applied to the weights, but only uniform windows are considered for data-independent weights here. In the literature, the term steering vector may be used to describe both the array manifold vector

and the weight vector, especially when the assumed/steering direction equals the source direction and uniform array element shading is used. In a non-dispersive environment,  $k_x = \frac{\omega}{c} \cos \theta \sin \phi = \frac{2\pi}{\lambda} \cos \theta \sin \phi$  is bounded by the possible physical locations such that  $0 \leq k_x < \frac{2\pi}{\lambda}$ . The (temporal) wavelength is given by  $\lambda$ . The physical bounds form an upper bound  $d \cdot k_x \leq \pi$  such that  $d \leq \frac{\lambda}{2}$ . Spatial aliasing occurs when  $d > \frac{\lambda}{2}$ . These appear in the beampattern from (5.4) as peaks known as grating lobes. Aliasing refers to the linear case where array manifold vectors for two different physical locations are the exact same. In this case,  $\mathbf{a}(k_1) = \mathbf{a}(k_2)$  for  $k_1 \neq k_2$ .

The array manifold vector from (5.3) can be rewritten as

$$\mathbf{a}(k_x) = e^{-j\frac{M-1}{2}k_x d} \left[ 1 \quad e^{jk_x d} \quad \dots \quad e^{j(M-1)k_x d} \right]^T \quad (5.5)$$

in order to emphasize the Vandermonde structure. A  $M \times Q$  Vandermonde matrix is defined as

$$\begin{bmatrix} 1 & 1 & \dots & 1 \\ a_1 & a_2 & \dots & a_Q \\ a_1^2 & a_2^2 & \dots & a_Q^2 \\ \vdots & \vdots & \ddots & \vdots \\ a_1^{M-1} & a_2^{M-1} & \dots & a_Q^{M-1} \end{bmatrix}. \quad (5.6)$$

Vandermonde columns are linearly independent for distinct  $a_q$ 's. Thus, the steering vectors for ULAs are linearly independent for distinct wavenumbers in the visible region, or distinct directions  $\theta$  in 2-D space. The array manifold matrix is formed by augmenting manifold vectors columns, written as

$$\mathbf{A} = \left[ \mathbf{a}(\theta_1) \quad \mathbf{a}(\theta_2) \quad \dots \quad \mathbf{a}(\theta_Q) \right], \quad (5.7)$$

and will be a Vandermonde matrix for a ULA in this case.

Again consider the beampattern given in (5.4). Assume the weights are given as  $w_m = \frac{1}{M}$ , which corresponds to a steering vector at broadside. The beampattern is

given by

$$b(k_x) = \frac{1}{M} \frac{\sin\left(\frac{M}{2}k_x d\right)}{\sin\left(\frac{1}{2}k_x d\right)} \quad (5.8)$$

where the first zero in the positive  $k_x$  direction occurs at  $k_x = \frac{2\pi}{Md}$ . From this it can be seen that the resolution of the array is a function of the total aperture length  $Md$ . A non-uniformly spaced array may be used to increase spatial resolution. However, note that the maximum array gain in the presence of spatially white noise is determined by the total number of physical sensors, where array gain is the ratio of the SNR of the array beamformed output over the SNR of a single receive element with  $|\mathbf{w}^H \mathbf{a}(k_x)|^2 = 1$ . For complete analysis see [5, p. 63]. A non-uniformly spaced linear array can achieve higher spatial resolution, but not higher array gain, than a ULA given the same number of sensors. This will be revisited later for colored noise or multiple sources.

### 5.1.2 Non-uniform Linear Arrays

Two types of non-uniform linear arrays (NLA) are considered. The first is the minimum redundancy linear array (MRLA) [89], which minimizes the number of sensors required to estimate a received covariance matrix of wide sense stationary data. In general, far-field uncorrelated sources in a homogeneous field are sufficient conditions for wide sense stationarity. In this case, the covariance matrix of data received by a ULA with white noise is Hermitian and Toeplitz. A Hermitian matrix is conjugate symmetric; a Toeplitz matrix has constant diagonal terms. The form of a Toeplitz Hermitian matrix is given by

$$\begin{bmatrix} a_0 & a_1 & a_2 & \cdots & a_M \\ a_1^* & a_0 & a_1 & \cdots & a_{M-1} \\ a_2^* & a_1^* & \ddots & & \vdots \\ \vdots & \vdots & & \ddots & \vdots \\ a_M^* & a_{M-1}^* & \cdots & \cdots & a_0 \end{bmatrix}. \quad (5.9)$$

Thus the entire matrix is known if  $a_m$  is known for all  $m \in [0, \dots, M]$ . Techniques to estimate covariance matrices of this form were first described by Burg *et. al* [21]. A MRLA uses the fewest number of sensors,  $M$ , to estimate a covariance matrix of size  $M_\alpha$  corresponding to a ULA. Element spacings are difficult to calculate because there is no formula for a spatial sequence that is minimally redundant, although various computational techniques have been suggested [90]. The number of times a spatial correlation lag ( $m$ th lag is  $a_m$  in (5.9)) is repeated is determined through the difference co-array, defined as

$$c(\tilde{\tau}) = \sum_{|m-n|=\tilde{\tau}} w_m w_n^*, \quad (5.10)$$

where  $w$  is the spatial windowing function used across the array and  $\tilde{\tau}$  is defined for all  $m, n \in [0 \dots M]$ . The uniform, also known as rectangular or boxcar, window is given by  $\mathbf{w} = \mathbf{1}_{M \times 1}$ . A similar concept is used in active array processing known as the sum co-array. The difference co-array is used here to determine the size of the largest covariance matrix. A spatial correlation vector is given by

$$\mathbf{r}_\alpha(\tilde{\tau} = |m - n|) = \mathbf{E}[x_m x_n^*]. \quad (5.11)$$

From the set of integers spanned by all spatial correlation lags,  $\tilde{\tau}$ , the subset of contiguous integers is indexed by  $\tau$ . A Vandermode covariance can be generated using  $r_\alpha(\tau) = a_\tau$  in (5.6). In this way, the covariance matrix of the co-array is formulated instead of the array itself. Increasing the number of effective lags can be characterized as augmenting the array manifold [91]. Note that the signal itself is not augmented, but the covariance matrix is augmented. The form of the augmented array manifold vector with  $M_a = \tau$  is given by

$$\mathbf{a}_\alpha(k) = [1, e^{-jkd}, \dots, e^{-jkd(M_a-1)}]^T \quad (5.12)$$

with augmented array manifold given by

$$\mathbf{A}_\alpha(\tilde{k}) = \mathbf{a}_\alpha(\tilde{k}) \forall \tilde{k} \in \Theta. \quad (5.13)$$

The augmented array manifold matrix for  $Q$  sources is  $\mathbf{A}_\alpha = [\mathbf{a}_\alpha(k_1) \cdots \mathbf{a}_\alpha(k_Q)]$ . Various methods have been proposed to form the co-array correlation vector with limited data and will be reviewed in the following sections.

Due to the difficulty of generating the spacings for a MRLA with a large number of elements, a class of non-uniform arrays has recently been developed by Vaidyanathan and Pal [92] based on properties of co-prime numbers. Integers  $M$  and  $N$  are coprime if they share no common factors other than 1. This leads to a co-array defined over  $\tilde{\tau} = Mn_1 + Nn_2$ , for  $0 \leq n_1 \leq N - 1$ ,  $0 \leq n_2 \leq M - 1$ . Therefore, two ULAs sharing a common axis and starting element are constructed with  $M\frac{\lambda}{2}$  and  $N\frac{\lambda}{2}$  spacing to create a NLA with  $M + N - 1$  elements. The range of values is a subset of  $[-N(M - 1), M(N - 1)]$ . Note that the values of interest are the contiguous values,  $\tau$ . The largest contiguous set is  $0 \leq \tau \leq MN - 1$  when  $n_1$  is expanded to  $0 \leq n_1 \leq 2N - 1$ . This is also possible with the expansion of  $n_2$  over  $-(M - 1) \leq n_2 \leq M - 1$ . This work has also been extended from the 1-D case to multiple dimensions [93]. However, co-prime arrays are not fully augmentable. Consider an array with largest spacing  $\max(M(2N - 1), NM) = 2MN - M$ , the largest contiguous set is  $MN$ . Therefore, any processing over a filled co-array will result in truncating the spatial aperture in half. All of the following work can be applied to contiguous co-arrays but the spatial aperture, and therefore degrees of freedom, will be halved for co-prime arrays.

### 5.1.3 Array Manifold Ambiguity and Identifiability

Many traditional source localization and parameter estimation techniques are based on the separation between the signal and noise subspaces in the received signal co-

variance matrix, such as the well known MUSIC algorithm [94]. A basic assumption in subspace algorithms is the ability to estimate and separate signal and noise eigenvectors. Subspace methods assume that the rank of the signal subspace is equal to the number of discrete signals and each source adds a unique linearly independent array manifold vector, and therefore the array manifold matrix must be full (column) rank. This is true for a ULA in white noise as long as there are fewer distinct sources than sensors, since the array manifold matrix is Vandermonde and thus full rank. Remember this is confined to the far-field, uncorrelated point source case. When the array manifold matrix is rank deficient, that is  $\text{rank } \mathbf{A}_{M \times Q} < Q$ , then an array manifold ambiguity exists. Proukakis and Manikas have shown that any linear array will have manifold ambiguities if the length of the array,  $L = \tilde{M} \frac{\lambda}{2}$ , exceeds a length such that:  $\tilde{M} > M - 1$  [95]. The ability to uniquely localize a source and the lack of an array manifold ambiguity are subtly different. Abramovich *et al.* [96] distinguish an array manifold ambiguity from identifiability in the following way. The source parameter,  $\tilde{k} \in \Theta$ , is considered nonidentifiable if at  $k_1 \in \Theta$  there exists  $k_1 \neq k_2$ ,  $k_2 \in \Theta$ , such that  $\mathbf{a}(k_1) = \mathbf{a}(k_2)$ . This implies an array manifold ambiguity exists as well. Note that it is possible for the parameter to be pointwise nonidentifiable such that a subset smaller than  $\Theta$  exists where the parameter is identifiable. Now consider the co-array manifold matrix,  $\mathbf{A}_\alpha$ , of size  $M_\alpha \times Q$  from (5.13). Note that  $\mathbf{A}_\alpha$  is Vandermonde and therefore the rank of  $\mathbf{A}_\alpha$  is the number of (distinct) sources,  $\text{rank } \mathbf{A}_\alpha = Q$ . This conditions means that there are no ambiguities on the co-array manifold, and therefore  $Q \leq M_\alpha$  distinct source wavenumbers are identifiable. To summarize for fully augmentable arrays, array manifold ambiguities in  $\mathcal{A}$  may be identifiable in  $\mathcal{A}$  and will not be ambiguous in  $\mathcal{A}_\alpha$ .

#### 5.1.4 Exploiting the Co-array

Source localization techniques based on direction of arrival have been developed using the co-array covariance matrix. For ULA geometries, the goal of these techniques is to form a field directionality map that “lifts” the source peaks above the noise [87, p. 384] and often these methods do not correspond to source amplitude [87, p. 372]. The covariance matrix of the co-array is referred to as  $\mathbf{R}_\alpha$  and entirely defined by  $\mathbf{r}_\alpha$  (5.11). This matrix is estimated using using the received data by augmenting the received data covariance matrix,  $\hat{\mathbf{R}}$ . Statistical analysis was performed by Pillai and Haber [91], where  $\hat{\mathbf{R}} = \frac{1}{N} \sum_{n=1}^N \mathbf{x}(n)\mathbf{x}^H(n)$  for  $N$  snapshots and

$$\hat{\mathbf{R}}_\alpha = \sum_{i=1}^{M_\alpha} \mathbf{A}_i \hat{\mathbf{R}} \mathbf{A}_i^T + \sum_{i=1}^{N_\alpha} (\mathbf{B}_i \hat{\mathbf{R}} \mathbf{C}_i^T + \mathbf{C}_i \hat{\mathbf{R}} \mathbf{B}_i^T). \quad (5.14)$$

The definitions of  $\mathbf{A}_i$ ,  $\mathbf{B}_i$  and  $\mathbf{C}_i$  are determined by  $\tau$  such that each matrix contains only one non-zero element, which is equal 1. Note that  $M_\alpha$  is the size of the augmented matrix and  $N_\alpha = M_\alpha(M_\alpha - 1)/2$ . The analysis by Pillai and Haber showed that the variance of  $\hat{\mathbf{R}}_\alpha$  is larger than  $\hat{\mathbf{R}}$ , requiring twice as many snapshots for a MRLA to match the performance of a ULA with the same aperture size. In later work, Abromavich *et. al* suggested averaging each lag,  $\tau$ , and forming the diagonals for the covariance as independent operations [97], which is the formulation used in the work proposed here. Note augmentation increases the number of parameters but does not provide more data. Conventional and MVDR beamforming has been applied to the augmented covariance matrix.

More recently, the concept of Khatri-Rao beamforming [98] has been extended to the Gaussian source model by Pal and Vaidyanathan [99]. Instead of estimating each lag individually as in (5.14), the received data covariance matrix is vectorized where  $\text{vec}(\hat{\mathbf{R}}) = \mathbf{A}^* \odot \mathbf{A} \mathbf{p} + \bar{\mathbf{1}}$  such that  $\mathbf{p} = \text{diag}(\boldsymbol{\Sigma})$ ,  $\mathbf{e}_m$  is a vector of zeros with 1 at the  $m$ th element, and  $\bar{\mathbf{1}} = [\mathbf{e}_1^T \cdots \mathbf{e}_M^T]^T$ . The Khatri-Rao product is a series of

column-wise Kroniker products such that  $\mathbf{A}^* \odot \mathbf{A} = [\mathbf{a}_1^* \otimes \mathbf{a}_1 \ \mathbf{a}_2^* \otimes \mathbf{a}_2 \ \cdots \ \mathbf{a}_Q^* \otimes \mathbf{a}_Q]$ . The vectorization of the covariance matrix results in multiple observations of the same lag with alternative definition by [99] as  $\tau = m - n$  (instead of the absolute value and therefore “doubling” the degrees of freedom). However, the resulting vectorized covariance is modified by deleting multiple observations of the same lag. The resulting vector is then split into over-lapping sub-arrays, defined as  $\mathbf{z}_i$ . The augmented covariance matrix is formed as  $\mathbf{R}_\alpha(\mathbf{z}) = \sum \mathbf{z}_i \mathbf{z}_i^H$ . This formulation results in a covariance matrix with the same size as direct augmentation given by (5.14) but is positive semi-definite. As noted in [99], a spatial smoothing technique known as forward-backward smoothing can be used to increase the dimensionality sub-array approach. Regardless, Khatri-Rao formulation ignores multiple independent observations of the same lag,  $\tau$ , at different locations (i.e. 2,1 and 4,3). Additionally, the proposed Khatri-Rao MVDR weights for MVDR require a “moderate” number of snapshots, which [99] implies to be on the order of 100s of snapshots with an array of  $M = 4$  sensors and effective co-array of  $M_\alpha = 11$ , where 100 snapshots with 4 jammers are required to achieve an array gain above the non-adaptive equivalent ULA.

Subspace methods applied directly to the received data covariance matrix of NLAs can fail due to array manifold ambiguities. Subspace techniques begin with a separation into signal and noise subspaces [15, 94], such as an SVD,  $\hat{\mathbf{R}} = \mathbf{U}\mathbf{\Sigma}\mathbf{V}^* = \mathbf{U}_s\mathbf{\Sigma}_s\mathbf{V}_s^* + \mathbf{U}_n\mathbf{\Sigma}_n\mathbf{V}_n^*$ . Where the singular vectors in  $\mathbf{U}$  corresponding to the  $Q$  largest singular values in  $\mathbf{\Sigma}$  form  $\mathbf{U}_s$  and the others form  $\mathbf{U}_n$ . The MUSIC spectrum is calculated by  $P(\theta) = \frac{1}{\mathbf{w}(\theta)^H \mathbf{U}_n \mathbf{U}_n^H \mathbf{w}(\theta)}$ . However, this degrades when an array manifold ambiguity occurs, and  $(\text{rank } \mathbf{U}_s) < Q < M$ . Array manifold ambiguities also always occur when  $Q > M$  in spatially stationary fields. Abramovich *et al.* noted that the co-array will not have an array manifold ambiguity as long as  $Q < M_a$  [96], and

suggested using MUSIC with  $\mathbf{R}$ , which results in non-source peaks due to ambiguities, alongside the higher variance MUSIC estimate with  $\mathbf{R}_a$ . No ambiguities occur using  $\mathbf{R}_a$ ; peaks that occur in both are used as location estimates.

Fuchs and Abramovich *et al.* have considered a technique based on the Pisarenko method [96, 100], which is referred to as the model-fitting method to contrast the subspace methods. The technique is performed through a linear program defined as

$$\begin{aligned} & \min_{p_m} \sum_{m=1}^{M_a} p_m \\ & \text{sub. to } \sum_{m=1}^{M_a} p_m \mathbf{a}(\theta_m) + \eta \mathbf{e}_1 = \hat{\mathbf{r}}_a \\ & \text{with } p_m > 0, \end{aligned} \tag{5.15}$$

where  $\mathbf{e}_1$  is a unit vector with 1 as the first element and  $\hat{\mathbf{r}}_a$  is an estimate of (5.11). In [100], the output power of a conventional beamformer is used for  $\hat{\mathbf{r}}_a$  to avoid the problem of imaginary numbers in  $\hat{\mathbf{r}}_a$ . In [96], the program is defined with an explicit formulation using only real numbers in the context complex data. The definition in [96] is more appropriate for frequency domain data:

$$\begin{aligned} & \min \mathbf{f}^T \mathbf{p} \\ & \text{sub. to } \mathbf{D}_{LP} \mathbf{p} = \hat{\mathbf{r}}_{\mathcal{R}} \\ & \text{with } \mathbf{p} > \mathbf{0}. \end{aligned} \tag{5.16}$$

where

$$\begin{aligned} \mathbf{f} &= [\mathbf{0}_{(m+\kappa) \times 1} | \mathbf{1}_{(4M_a-4) \times 1}]^T \in \mathcal{R}^{(m+\kappa+4M_a-4) \times 1} \\ \mathbf{D}_{LP} &= \begin{bmatrix} \mathcal{R}e \mathbf{D}_a(\hat{\boldsymbol{\theta}}) & | & 0 \cdots 0 & | & 0 \cdots 0 \\ \mathcal{I}m \mathbf{D}_a(\hat{\boldsymbol{\theta}}) & | & \mathbf{I}_{2(M_a-1)} & | & -\mathbf{I}_{2(M_a-1)} \end{bmatrix} \in \mathcal{R}^{(2M_a-1) \times (m+\kappa+4M_a-4)} \\ \hat{\mathbf{r}}_{\mathcal{R}} &= \begin{bmatrix} \mathcal{R}e \hat{\mathbf{r}}_a \\ \mathcal{I}m \hat{\mathbf{r}}_a \end{bmatrix} \in \mathcal{R}^{(2M_a-1) \times 1} \\ \mathbf{p} &\in \mathcal{R}_+^{(m+\kappa+4M_a-4)}. \end{aligned} \tag{5.17}$$

The number of columns of  $\mathcal{I}m \mathbf{D}_a(\hat{\boldsymbol{\theta}})$  and  $\mathcal{I}m \hat{\mathbf{r}}_a$  is  $M_a - 1$  since the single row containing zeroes has been deleted. Note that signal parameters,  $p_m$  or  $\mathbf{p}$ , and noise parameter,  $\eta$ , in (5.15) refer to positive power levels in this case. As a point of comparison, Pal and Vaidyanathan [99] noted that direct covariance matrix augmentation, (5.14), uses half of the degrees of freedom but it is clear from (5.17) that an alternative view is a splitting of real and imaginary numbers. However, circular symmetry of the received data restricts  $E[\mathbf{xx}^T] = \mathbf{0}$ , and the received data covariance matrix to be Hermitian. Thus the total degrees of freedom are limited by the distinct  $\tilde{\tau}$ 's as  $|m - n|$  for stationary, normally distributed data.

The model-fitting estimators do not require linear array assumptions as noted by [84, 100], but general arbitrary array analysis is difficult. The solution uses an  $l_1$  norm in order to reduce the false peaks that appear in subspace based estimates. In the presence of high SNR sources, the  $l_1$  norm may group low SNR sources with the noise, especially with a limited number of snapshots. This issue is raised by the same authors in [101], but they do not consider the problem in the context of a model-fitting estimator. This may be due to the fact that source detection is a highly related but different problem than localization. Direction of arrival algorithms sometimes over-estimate the number of signals in order to guarantee signals are not lost and then perform post-processing to reduce the number of signals, as suggested by Abramovich *et. al* [96].

#### 5.1.5 Source Detection with a NLA

Estimating the number of sources, often called source detection, with a NLA in a spatially stationary field, was addressed by Abramovich *et al.* [101] and is used for the following discussion. The Pisarenko and MUSIC methods require signals to be orthogonal to the noise eigenvectors. However, instead of peak-peaking, the work in [101] is based on a likelihood ratio or information theoretic approach. Assuming

a positive definite Toeplitz covariance matrix with  $Q$  signals, the  $M_a - Q$  smallest eigenvalues are equal. Wax and Kailath used this approach to determine the number of signals using minimum descriptive length (MDL) [102]. However, Abramovich *et al.* note that this requires the estimated covariance matrix  $\hat{\mathbf{R}}$  to be Toeplitz, which is not true in general. This also applies to the estimated co-array covariance matrix  $\hat{\mathbf{R}}_a$ . Noting that no optimal (or sub-optimal) closed-form estimate currently exists for  $\hat{\mathbf{R}}$  that ensures the matrix is positive definite Toeplitz, an iterative algorithm is given in [101] using multiple linear programs. The solution considers a constant false alarm rate when detecting sources.

An additional problem noted in [101] is the potential for signal subspaces to collapse. Array manifold ambiguities discussed in Section 5.1.3 is an example and may be avoided in  $\mathcal{A}_a$ . However, a detection will reach a limit (due to limited snapshot support) as signal power decreases to the noise floor. Assuming a finite amount of data, this creates a limit where the signal with the least power will collapse into the noise subspace. This will be a function of the other signals as well as the number of snapshots but is sometimes ignored in the context of NLAs and manifold ambiguities.

The previous techniques typically only consider  $0^\circ \leq \theta < 180^\circ$  because of ambiguities due to linear geometry. An analysis for planar linear arrays was conducted by RübSamen and Gershman [103], which focuses on array geometry design. These geometries allow estimation over  $0^\circ \leq \theta < 360^\circ$  and are based on the MRLA concept. Source localization is accomplished using a steering vector approximation based on manifold separation  $\mathbf{a}(\theta) \approx \mathbf{G}\hat{\mathbf{d}}(\theta)$  (see [104]), where  $\mathbf{G}$  is estimated via least squares and  $\hat{\mathbf{d}}(\theta)$  forms a column of a Vandermonde matrix. Subspace methods can be used with this approximation [105, 106].

## 5.2 Geometric Interpretation

Array manifold ambiguities and identifiability conditions can be interpreted geometrically. The treatment of array manifolds in terms of differential geometry was formalized by Manikas, who also wrote a textbook on the subject [107, 108]. The wavenumber,  $\mathbf{k}$ , is the vector in physical coordinates that describes wave propagation and is spatially invariant in homogeneous environments. The array is described using a vector in physical coordinates describing positions,  $\mathbf{r}_m$  for the position of the  $m$ th sensor. An array manifold vector relates  $M$  sensed locations and a single propagation vector  $\mathbf{k}_q$  to a single array manifold vector in  $\mathfrak{C}^M$  space, defined by (5.12) for a linear array in 2D space or (3.2) in general. The pictorial representation is shown in Figure 5.1. The array manifold is the locus of points in  $\mathfrak{C}^M$  space and therefore forms the curve shown in the figure. The resolvability of the array can be viewed as the separation of sources along the curve.

The concept of array manifold ambiguity can be interpreted in this context as well, as suggested by Manikas. Sources are non-identifiable when the array manifold “loops” back on itself, such that the array manifold vectors for two sources that are well separated in arc length down the array manifold point to equivalent locations in  $\mathfrak{C}^M$ , as shown in Figure 5.2(a). Rank deficient array manifolds occur when a “loop” does not cross in  $\mathfrak{C}^M$  space but does reside in a smaller subspace spanned by array manifold vectors of sources in the field. This is shown in Figure 5.2(b) where the subspace  $\mathfrak{C}^3$  is defined by the origin and two points on the manifold. If a third point crosses this subspace, then that third point will not increase the size of the subspace. Methods that search the array manifold for source detection using sub-space separation, such as MUSIC, will have a peak at these 3 locations whenever at least 2 of the sources are present. This also extends to larger subspace sizes and is guaranteed to occur when the average inter-element spacing exceeds a

half-wavelength. Note that the probability of a single source appearing at the exact point is 0 for uniformly distributed sources. However, as noted by Abramovich *et al.* [101] when the number of snapshots is limited then the signal subspace can collapse into the nearby smaller subspaces. In the geometric interpretation, noise results in uncertainty in array manifold vectors as a ball expanding around the point in  $\mathfrak{C}^M$ . Thus for limited number of snapshots or for sources with a low SNR, the chances of a rank deficient scenario increases.

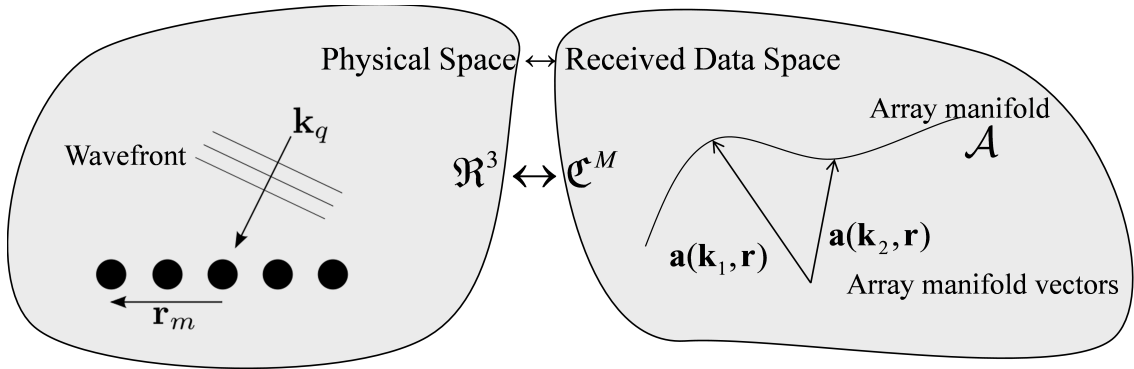
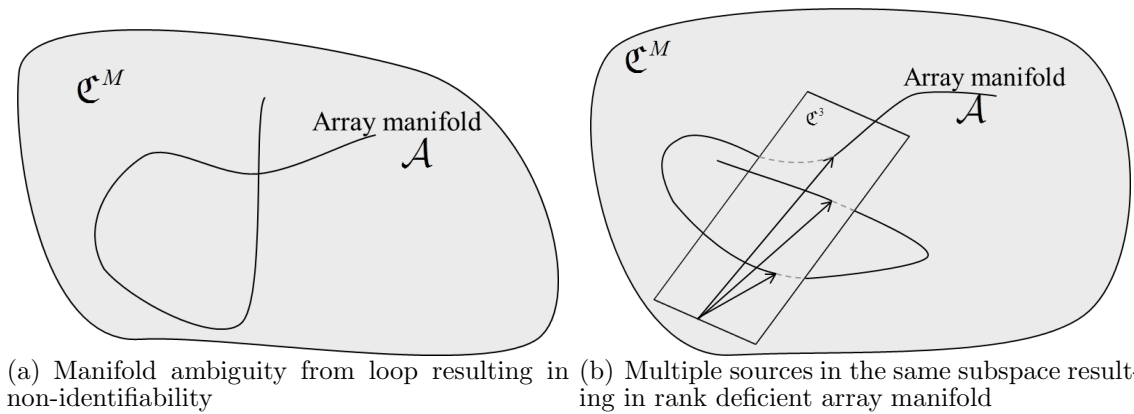


FIGURE 5.1: Pictorial relationship between physical vectors and array manifold vectors



(a) Manifold ambiguity from loop resulting in non-identifiability (b) Multiple sources in the same subspace resulting in rank deficient array manifold

FIGURE 5.2: Illustrative examples of array manifold ambiguities

### 5.3 Near-field Sources and Snapshot Deficient Processing

Near-field dynamic targets introduce a non-stationary component both spatially, through non-planewave propagation, and temporally, due to target motion. Near-field sources in the presence of far-field interference occurs in applications such as microphone array processing for speech, guidance systems for homing, and passive sonar. Non-adaptive solutions have focused on weight designs that jointly consider near-field and far-field beampatterns [109]. Adaptive techniques have been developed based on higher-order statistics, which require an order of magnitude of snapshots or more compared to second-order methods [110]. A mixed-order solution has also been developed for estimating bearing by applying MUSIC on the cumulants and estimating range using MUSIC on the covariance [111]. In passive acoustics, the problem of snapshot deficiency stems from the fact that the speed of propagation is quite slow. Analysis by Baggeroer and Cox [29] showed that the number of snapshots is limited by  $N < \frac{c\lambda}{8\dot{\theta}L^2}$  where  $\dot{\theta}$  is the bearing rate of the source,  $L$  is the length of the array, and a single snapshot is formed using the amount of time it takes for a wave to propagate across the array multiplied by 8. As an example, an array with 50 sensors at half-wavelength spacing,  $N < \frac{c}{3200\lambda\dot{\theta}}$ . Near-field targets make the problem worse by increasing the bearing rate,  $\dot{\theta}$ . Note that the speed of sound is significantly lower than the speed of light, thus for similar wavelengths the number of snapshots is much more limited in acoustics than electromagnetics.

Assuming the interference is wide sense stationary, the degrees of freedom available for interference suppression can be increased using second order statistics. Unlike previous approaches that use cumulants to adaptively separate near-field sources, the methods proposed here focus on the far-field interference. However, covariance matrix augmentation using the co-array increases the variance of the spectrum estimate and requires more snapshots to achieve the similar performance of a filled array. This

provides a second motivation to consider the limited data case.

Traditionally, rank reduced adaptive beamforming improves interference suppression when the number of snapshots is less than the number of sensors but greater than the number of discrete interferers. Partially adaptive or rank reduced algorithms lower computational complexity and sensitivity to model mismatch [112]. Instead of using physical constraints, such as the classical linearly constrained minimum variance approach [113], array structure independent processing has been developed using either the largest eigenvalues [114] or the subspace closest to the desired signal [115]. As a rule of thumb, twice as many snapshots as interferers are required when the sources movement is limited to a single beam-width during the observation time window [116]. Note that both reduced rank processing and diagonal loading (e.g. adding white noise) are used to mitigate the effects of limited snapshots. Due to the limited number of snapshots and increased variance of augmentation, a variation of dominate mode rejection (DMR) applied to the co-array is proposed. DMR assumes an interference environment that is louder than the source [31]. Augmented DMR, proposed here, allows the suppression of more interferers than sensors while mitigating the impact of snapshot deficiency.

The problem is illustrated in Figure 5.3, where an under-sampled array is used to null many far-field interferers in the presence of near-field sources. Note the assumption is that the interference is in the far-field and sources of interest are in the near-field. Additionally, the interference is assumed to be much louder than the near-field sources. However, the fundamental problem is of non-stationary sources in the presence of spatially stationary interference. The proposed solution is two-fold: exploiting the co-array to adaptively suppress more far-field interferers than sensors and near-field rank reduced beamforming to reduce the impact of snapshot deficiency and augmentation.

The concludes the review of related work in literature, and the rest of the chap-

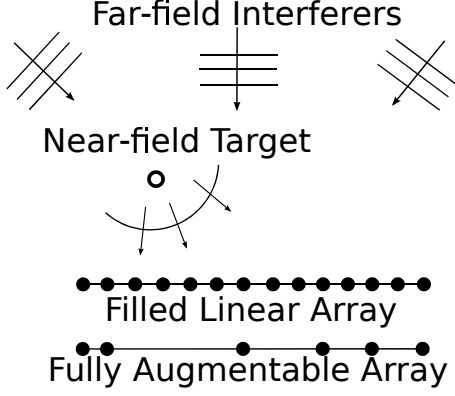


FIGURE 5.3: Example scenario of near-field target in far-field interference

ter is organized as follows. The signal model of the received data is described in Section 5.4. The method for data augmentation and modification for near-field processing are proposed in Section 5.5 with bounding analysis assuming a known data covariance. Reduced rank processing for finite data is derived and analyzed in Section 5.6. Monte Carlo simulation with more sources than sensors is given in Section 5.7 to demonstrate traditional dominate mode rejection processing compared to the augmented approach with a near-field target in an interference dominated environment.

#### 5.4 Far-field and Near-field Received Signal Model

Consider a linear passive array of  $M$  sensors with distance from the first element to the  $m$ th element given by  $d_m$ , where  $d_1 = 0$ . Interfering sources are assumed to be in the far-field such that the array manifold vector for the  $q$ th interferer in direction  $\theta_q$  is given by  $[\mathbf{a}(\theta_q)]_m = \exp(-jk d_m \cos(\theta_q))$ , where  $k$  is the magnitude of the wavenumber. The interference array manifold matrix is given by  $\mathbf{A}_I = [\mathbf{a}(\theta_1) \cdots \mathbf{a}(\theta_Q)]$ . The target or desired signals are assumed to be in the near-field where the array manifold vector,

$$[\mathbf{a}(\theta, r)]_m = \exp\left(-jk(d_m^2 + r^2 - 2d_m r \cos(\theta))^{1/2}\right) \quad (5.18)$$

is a function of both angle,  $\theta$ , and range,  $r$ . For passive array processing, the interference source signals,  $\mathbf{s}_I \sim \mathcal{CN}(\mathbf{0}, \mathbf{\Sigma}_I)$ , near-field signals  $\mathbf{s} \sim \mathcal{CN}(\mathbf{0}, \mathbf{\Sigma})$ , and noise,  $\boldsymbol{\eta} \sim \mathcal{CN}(\mathbf{0}, \sigma_\eta^2 \mathbf{I})$ , are zero-mean circularly symmetric complex normally distributed. All sources are assumed to be uncorrelated. The received signal is the sum of the statistically independent interference, near-field sources and noise given by

$$\mathbf{x} = \mathbf{A}_I \mathbf{s}_I + \mathbf{A} \mathbf{s} + \boldsymbol{\eta}, \quad (5.19)$$

where  $D$  near-field signals have locations such that  $\mathbf{A} = [\mathbf{a}(\theta_1, r_1) \cdots \mathbf{a}(\theta_D, r_D)]$ . Thus the received signal is distributed according to  $\mathbf{x} \sim \mathcal{CN}(\mathbf{0}, \mathbf{R})$  where the covariance matrix is given by

$$\mathbf{R} = \mathbf{A}_I \mathbf{\Sigma}_I \mathbf{A}_I^H + \mathbf{A} \mathbf{\Sigma} \mathbf{A}^H + \sigma_\eta^2 \mathbf{I}. \quad (5.20)$$

Let the covariance matrix be rewritten  $\mathbf{R} = \mathbf{R}_I + \mathbf{R}_D + \mathbf{R}_\eta$  corresponding to the three terms in (5.20). Note that the interference,  $\mathbf{R}_I$ , and noise,  $\mathbf{R}_N$ , are wide sense stationary, as required for increasing the degrees of freedom through covariance matrix augmentation.

## 5.5 Covariance Matrix Augmentation

Covariance matrix augmentation allows a fully augmentable, non-uniform array to be processed as a uniform linear array with the same total aperture. In this way, the number of degrees of freedom is increased, and far-field array manifold vectors from different directions are linearly independent. The received data covariance matrix estimate is given by  $\hat{\mathbf{R}} = \frac{1}{N} \sum_{n=1}^N \mathbf{x}(n) \mathbf{x}(n)$ , using  $N$  i.i.d. snapshots. Assuming wide sense stationarity, the autocorrelation is a function of the relative distance between sensors, which results in a Toeplitz covariance matrix where each diagonal is a constant term [91]. Additionally, all inter-element spacings are assumed to be a half-wavelength, such that  $d = \lambda/2$ . An augmented covariance matrix is formed by

averaging over each observation of the relative distance,  $d\tau$ , given by [101]

$$\hat{\mathbf{T}}(\tau) = \frac{\sum_{a,b=1}^M [\hat{\mathbf{R}}]_{ab} \delta(d\tau, d_a - d_b)}{\sum_{a,b=1}^M \delta(d\tau, d_a - d_b)}, \quad (5.21)$$

where  $\hat{\mathbf{T}}(\tau)$  refers to the  $\tau$ th diagonal of  $\hat{\mathbf{T}}$ ,  $\delta(a, b)$  is the Kronecker delta function, and  $d_a, d_b$  represent sensor locations. Note that  $\mathbf{T}$  is used instead of  $\mathbf{R}_\alpha$  since near-field sources are considered. Let the non-negative contiguous  $\tau$ 's be indexed from 0 to  $M_\alpha$ , which is assumed to be greater than the number of sensors,  $M$ . The increased size of the covariance matrix results in increased variance, on the order of twice the variance for conventional non-adaptive beamforming with MRLAs [91]. Note that augmented covariances formed using the direct approach of (5.21) may have negative eigenvalues, but positive definite matrix completion can be used to ensure all eigenvalues are positive iteratively (see [97]). The approach in [99] avoids negative eigenvalues but ignores multiple observations of the same lag, then averages along the diagonal through spatial smoothing. There is no known closed form maximum likelihood solution to the positive definite Toeplitz covariance matrix estimation problem.

Consider the case where the received data statistics are known,  $\mathbf{R}$  and  $\mathbf{T} = \text{E}[\hat{\mathbf{T}}]$ . Linear beamforming power is of the form  $\mathbf{w}^H \mathbf{R} \mathbf{w}$  or  $\mathbf{w}_\alpha^H \mathbf{T} \mathbf{w}_\alpha$  in the augmented domain. Note that  $\mathbf{R}_\alpha$  is treated as the covariance matrix of a filled ULA array of size  $M_\alpha$ . Data independent conventional weights, also known as delay-and-sum, are given by

$$\mathbf{w}_{\text{conv}} = \mathbf{a}_\alpha \quad (5.22)$$

where steering vector,  $\mathbf{a}_\alpha$ , is an assumed far-field or near-field array manifold vector. Minimum Variance Distortionless Response (MVDR) weights are the solution to

$$\mathbf{w}_{\text{MVDR},\alpha} = \arg \min_{\mathbf{w}} \mathbf{w}^H \mathbf{T} \mathbf{w} \text{ sub. to } \mathbf{w}^H \mathbf{a}_\alpha = 1. \quad (5.23)$$

When the interference and noise statistics are known, their sum can replace  $\mathbf{T}$  in

(5.23), but in both cases the solutions have been called MVDR and provide optimal output signal to interference and noise (SINR) with a unity gain constraint in the steering direction. The use of a signal free covariance matrix results in lowered sensitivity to signal mismatch, which occurs when the assumed and true array manifold vectors differ. Diagonal loading is typically used in order to reduce the impact signal mismatch by artificially increasing the white noise level [10]. The solution to (5.23) with diagonal loading is given by

$$\mathbf{w}_\alpha = \frac{(\mathbf{T} + \varepsilon\mathbf{I})^{-1}\mathbf{a}_\alpha}{\mathbf{a}_\alpha^H(\mathbf{T} + \varepsilon\mathbf{I})^{-1}\mathbf{a}_\alpha}. \quad (5.24)$$

However, the co-array manifold vector,  $\mathbf{a}_\alpha(\theta, r)$  is not sensed by the NLA for near-field sources. Therefore, a modification is proposed where the MVDR steering vector constraint uses only the sensed sensor locations. Consider the modified steering vector

$$\mathbf{v}_\alpha = \mathbf{J}\mathbf{a}_\alpha. \quad (5.25)$$

$\mathbf{J}$  is a square selection matrix with ones on the main diagonal locations corresponding sensor locations and zeros elsewhere such that  $\mathbf{J} = \sum_{m=1}^M \mathbf{e}_{\tau_m} \mathbf{e}_{\tau_m}^T$ , where  $\mathbf{e}_\tau$  is a  $M_\alpha \times 1$  unit vector with a one at the  $\tau$ th element and zeros elsewhere and  $\tau_m = d_m/(\lambda/2) + 1$ . Thus the modified weights are given by substituting (5.25) into (5.24) and given by

$$\mathbf{w}_{\alpha 2} = \frac{(\mathbf{T} + \varepsilon\mathbf{I})^{-1}\mathbf{v}_\alpha}{\mathbf{v}_\alpha^H(\mathbf{T} + \varepsilon\mathbf{I})^{-1}\mathbf{v}_\alpha}. \quad (5.26)$$

The performance of beamforming using (5.24) and (5.26) is derived in terms of array gain.

#### *Augmented Array Gain*

The array gain of augmentation is compared to the equivalent filled ULA assuming the received data statistics are known. Consider the case where the augmented

covariance matrix  $\mathbf{R}_\alpha$  is constructed from the received signal covariance matrix. Using (5.21), the augmented near-field covariance matrix is defined as  $\mathbf{T}_D$  using  $\mathbf{R}_D$  in (5.21). Note that the near-field source covariance is not assumed to be wide sense stationary and therefore may not be Toeplitz. Defining  $\mathbf{R}_{I,\alpha} = \mathbf{A}_{I,\alpha}\boldsymbol{\Sigma}_I\mathbf{A}_{I,\alpha}$  and  $\mathbf{R}_{N,\alpha} = \sigma_\eta^2\mathbf{I}$ , the augmented covariance matrix is given by  $\mathbf{T} = \mathbf{R}_{I,\alpha} + \mathbf{T}_D + \mathbf{R}_{N,\alpha}$ . Note that the interference, assumed to be planewaves, and the noise are unaffected by averaging along the diagonal. For array gain calculations, the array is assumed to be steered to a true source such that  $\mathbf{a}_\alpha$  is the array manifold vector for the desired signal. The array gain,  $A$ , for a single near-field source is defined for the equivalent ULA as

$$A_{ULA} = \frac{\mathbf{w}_\alpha^H \sigma^2 \mathbf{a}_\alpha \mathbf{a}_\alpha^H \mathbf{w}_\alpha}{\mathbf{w}_\alpha^H (\mathbf{R}_{I,\alpha} + \mathbf{R}_{N,\alpha}) \mathbf{w}_\alpha} \frac{\sigma_\eta^2}{\sigma^2} \quad (5.27)$$

and covariance matrix augmentation, (5.21), is given by

$$A = \frac{\mathbf{w}_\alpha^H \mathbf{T}_D \mathbf{w}_\alpha}{\mathbf{w}_\alpha^H (\mathbf{R}_{I,\alpha} + \mathbf{R}_{N,\alpha}) \mathbf{w}_\alpha} \frac{\sigma_\eta^2}{\sigma^2} \quad (5.28)$$

First, consider no interferers and white noise with no diagonal loading such that  $\mathbf{w}_\alpha = \mathbf{a}_\alpha/M_\alpha$  or  $\mathbf{w}_{\alpha 2} = \mathbf{v}_\alpha/M$ . In this case, the array gain of a ULA is the number of sensors,  $A_{ULA} = M_\alpha$ , and weights using (5.24) are denoted  $A_1 = \frac{\mathbf{a}_\alpha^H \mathbf{T}_D \mathbf{a}_\alpha}{\sigma^2}$  with weights from (5.26) given by  $A_2 = \frac{\mathbf{v}_\alpha^H \mathbf{T}_D \mathbf{v}_\alpha}{\sigma^2}$ . Note that  $\text{tr}(\mathbf{T}_D) = \sigma^2 M_\alpha$ ,  $\mathbf{a}_\alpha^H \mathbf{a}_\alpha = M_\alpha$ , and  $\mathbf{v}_\alpha^H \mathbf{v}_\alpha = M$ ; therefore, the maximum of  $A_1$  is  $M_\alpha$  and  $A_2$  is  $M$ . The specific array gain for a near-field source is a function of location.

Second, consider interferers and white noise with no diagonal loading. Extending the same argument for interferer free case, an upper bound is the maximum gain of the MVDR beamformer. Thus  $A_{ULA}$  and  $A_1$  are bounded by  $M_\alpha(1 + \text{tr}(\boldsymbol{\Sigma}_I)/\sigma_\eta^2)$  while  $A_2$  is bounded by  $M(1 + \text{tr}(\boldsymbol{\Sigma}_I)/\sigma_\eta^2)$  [5, p. 468].

## 5.6 Reduced Rank Adaptive Beamforming

In general, the received data statistics are not known and must be estimated. The problem of a finite number of snapshots is addressed in this section through reduced rank processing. First consider the MRLA without augmentation. MVDR weights with diagonal loading using finite snapshots are given by

$$\mathbf{w}_{MVDR} = \frac{\left(\hat{\mathbf{R}} + \varepsilon \mathbf{I}\right)^{-1} \mathbf{a}}{\mathbf{a}^H \left(\hat{\mathbf{R}} + \varepsilon \mathbf{I}\right)^{-1} \mathbf{a}}. \quad (5.29)$$

Note that diagonal loading is required for inversion when the number of snapshots is less than the number of sensors,  $N < M$ . Additionally, MVDR without diagonal loading requires  $N = 2M$  snapshots in order for the expected value of SINR to be within 3 dB of the optimal SINR without diagonal loading [30]. In order to reduce the number of required snapshots, Dominate Mode Rejection (DMR) was proposed where only the largest eigenvalues and corresponding eigenvectors are considered for inversion. Intuitively, most of the adaptive gain is provided by loud interference suppression and thus the largest eigenvalues. The smallest eigenvalues contribute only marginally to interference suppression but have the highest sensitivity for matrix inversion. Additionally, the smallest eigenvalues are also the most difficult to estimate so therefore DMR uses ensemble averaging across eigenvalues or forces a whitening condition to reduce sensitivity.

Consider the eigendecomposition of the estimated covariance matrix  $\hat{\mathbf{R}} = \mathbf{U}\mathbf{\Lambda}\mathbf{U}^H = \sum_{k=1}^N \lambda_k \mathbf{u}_k \mathbf{u}_k^H$ . Note that if  $\hat{\mathbf{R}}$  has rank  $K$  then  $\lambda_k = 0 \ \forall \ K < k \leq M$  and  $\lambda_k > 0 \ \forall \ 1 < k \leq K$ . In general, the maximum rank of  $\hat{\mathbf{R}}$  is at most the number of sensors or snapshots ( $K \leq M, K \leq N$ ), and  $\hat{\mathbf{R}}$  is positive semi-definite by construction. The inverse is given by  $\hat{\mathbf{R}}^{-1} = \sum_{k=1}^N \lambda_k^{-1} \mathbf{u}_k \mathbf{u}_k^H$ . Consider the low rank

approximation via decomposition

$$\hat{\mathbf{R}}_K = \sum_{k=1}^K \lambda_k \mathbf{u}_k \mathbf{u}_k^H + \sum_{k=1}^M \tilde{\lambda} \mathbf{u}_k \mathbf{u}_k^H \approx \hat{\mathbf{R}} \quad (5.30)$$

where  $\tilde{\lambda}$  is deterministic and known. Note that many decomposition methods, such as singular value decomposition (SVD), always provide a full column (or row) rank solution even if the matrix is not full rank. There are multiple forms of DMR and the one considered here is given by

$$\mathbf{w}_{DMR} = \frac{\left(\hat{\mathbf{R}}_K + \varepsilon \mathbf{I}\right)^{-1} \mathbf{a}}{\mathbf{a}^H \left(\hat{\mathbf{R}}_K + \varepsilon \mathbf{I}\right)^{-1} \mathbf{a}}. \quad (5.31)$$

Note that the form of DMR presented by [31] is obtained by setting  $\tilde{\lambda} = 0$ , and the inverse can be written as

$$\left(\hat{\mathbf{R}}_K + \varepsilon \mathbf{I}\right)^{-1} = \frac{1}{\varepsilon} \left( \mathbf{I} - \sum_{k=1}^K \frac{\lambda_k}{\lambda_k + \varepsilon} \mathbf{u}_k \mathbf{u}_k^H \right) \quad (5.32)$$

using the Woodbury matrix identity.

The concept of DMR is proposed here for augmented arrays to mitigate the effects of finites snapshot due to target motion and the increased snapshot sensitivity from augmentation. Eigendecomposition of the augmented covariance matrix is given by

$$\hat{\mathbf{T}} = \sum_{n=1}^K \lambda_n \mathbf{u}_n \mathbf{u}_n^H + \sum_{n=K+1}^{M_\alpha} \lambda_n \mathbf{u}_n \mathbf{u}_n^H \quad (5.33)$$

where the subspace of the  $K$  strongest interferers is approximated by the first term of (5.33). As in DMR, consider the approximation given by

$$\hat{\mathbf{T}}_K = \sum_{n=1}^K \lambda_n \mathbf{u}_n \mathbf{u}_n^H + \sum_{n=K+1}^{M_\alpha} \tilde{\lambda} \mathbf{u}_n \mathbf{u}_n^H. \quad (5.34)$$

Rank reduced weights of the same form as (5.31) are given by

$$\mathbf{w}_{ADMR} = \frac{\left(\hat{\mathbf{T}}_K + \varepsilon \mathbf{I}\right)^{-1} \mathbf{a}_\alpha}{\mathbf{a}_\alpha^H \left(\hat{\mathbf{T}}_K + \varepsilon \mathbf{I}\right)^{-1} \mathbf{a}_\alpha}. \quad (5.35)$$

The beamformed power output is then given by  $\mathbf{w}_{ADMR}^H \hat{\mathbf{T}} \mathbf{w}_{ADMR}$ .

Consider the effects of the estimate,  $\mathbf{T}$ , given by (5.21). In general,  $\hat{\mathbf{T}}$  is not an optimal estimate of an augmented covariance matrix,  $\mathbf{T}$ . Note that there will be some loss due to the non-stationarity of the near-field wavefront. Additionally, each of the diagonals of  $\hat{\mathbf{T}}$  are estimated using a different number of samples and that the samples will be dependent. Therefore, the distribution of the estimate  $\hat{\mathbf{T}}$  is quite complex and a function of higher order statistics, which require even an even greater number of snapshots to exploit. The simplest solution is to use only the observed sensor locations in the steering vector,  $\mathbf{a}$ . This is proposed as a second rank reduction where the augmented dimensions are projected out of the steering vector. In this case, covariance matrix augmentation is used to suppress interference but not enhance signal to white noise performance. The proposed operation is equivalent to the proposed method given in (5.25) for near-field sources.

Using the geometric approach suggested by Scharf and Tufts for the general rank reduction approach [112], the augmented dimensions in this case have a higher noise level than the non-augmented dimensions while the source level is assumed to be flat. Thus by discarding the areas with higher noise, a tradeoff in noise reduction (estimate variance) and signal loss (estimate bias) is formed. An optimal approach would require knowledge of the distribution of  $\hat{\mathbf{T}}$ , which is left as an open problem. Substituting the modified steering vector given by (5.25) into (5.35) results in weights

defined as

$$\mathbf{w}_{ADMR2} = \frac{\left(\hat{\mathbf{T}}_K + \varepsilon \mathbf{I}\right)^{-1} \mathbf{J} \mathbf{a}_\alpha}{\mathbf{a}_\alpha^H \mathbf{J}^T \left(\hat{\mathbf{T}}_K + \varepsilon \mathbf{I}\right)^{-1} \mathbf{J} \mathbf{a}_\alpha}. \quad (5.36)$$

*Partially Adaptive Array Gain*

The asymptotic performance of partially adaptive, or rank reduced, beamforming is considered as a function of the ratio of sensors to snapshots for case of  $\tilde{\lambda} = 0$  from (5.30). Note that covariance augmentation is ignored in this analytical analysis. Previous work has not provided analytical results for reduced rank processing as a function of diagonal loading and fewer snapshots than sensors. The input SINR is independent of processing and given by  $\frac{\sigma_s^2}{\sigma_\eta^2 + \sum_{q=1}^Q \sigma_q^2}$ . The output SINR for the partially adaptive solution is given by

$$\text{Output SINR} = \frac{\mathbf{w}^H \mathbf{R}_s \mathbf{w}}{\mathbf{w}^H \mathbf{R} \mathbf{w} - \mathbf{w}^H \mathbf{R}_s \mathbf{w}} \quad (5.37)$$

where the target signal covariance matrix is  $\mathbf{R}_s = \sigma_s^2 \mathbf{a} \mathbf{a}^H$ . Assuming that the steered direction is equal to the target direction, then

$$\text{Output SINR} = \frac{\sigma_s^2 |\mathbf{w}^H \mathbf{a}|^2}{\mathbf{w}^H \mathbf{R} \mathbf{w} - \sigma_s^2 |\mathbf{w}^H \mathbf{a}|^2}$$

The desired target power in the numerator reduces to  $\sigma_s^2 |\mathbf{w}^H \mathbf{a}|^2$ . The term of interest the power of the inner product of the weights with the target vector

$$|\mathbf{w}^H \mathbf{a}|^2 = \mathbf{a}^H (\hat{\mathbf{R}}_K + \varepsilon \mathbf{I})^{-1} \mathbf{a} \mathbf{a}^H (\hat{\mathbf{R}}_K + \varepsilon \mathbf{I})^{-1} \mathbf{a} / \kappa \quad (5.38)$$

$$= |\mathbf{a} (\hat{\mathbf{R}}_K + \varepsilon \mathbf{I})^{-1} \mathbf{a}|^2 / \kappa. \quad (5.39)$$

where  $\kappa$  represents the normalization from the unity gain constraint but does not effect array gain. Consider the random matrix  $\mathbf{W} = \frac{1}{N} \mathbf{\Xi} \mathbf{\Xi}^H$  where the  $N$  columns of are i.i.d. of size  $M \times 1$  and  $\mathbf{\Xi} \sim \mathcal{CN}(0, \mathbf{I})$ . Note that assuming  $\tilde{\lambda} = 0$  or  $\tilde{\lambda}$  is random

results in  $\hat{\mathbf{R}}_K = \mathbf{R}_K^{\frac{1}{2}} \mathbf{W} \mathbf{R}_K^{\frac{1}{2}}$  and  $\mathbf{R}_K = \mathbf{R}_K^{\frac{1}{2}} \mathbf{R}_K^{\frac{1}{2}}$ . The term within the absolute value in (5.39) is written as

$$\mathbf{a}^H \left( \hat{\mathbf{R}}_K + \varepsilon \mathbf{I} \right)^{-1} \mathbf{a} = \mathbf{a}^H \left( \mathbf{R}_K^{\frac{1}{2}} \mathbf{W} \mathbf{R}_K^{\frac{1}{2}} + \varepsilon \mathbf{I} \right)^{-1} \mathbf{a} \quad (5.40)$$

$$= \mathbf{a}^H \mathbf{R}_K^{-\frac{1}{2}} \left( \mathbf{W} + \varepsilon \mathbf{R}_K^{-1} \right)^{-1} \mathbf{R}_K^{-\frac{1}{2}} \mathbf{a} \quad (5.41)$$

where  $\mathbf{R}_K^{-\frac{1}{2}} = \lim_{\varepsilon \rightarrow 0^+} (\mathbf{R}_K + \varepsilon)^{-1} \mathbf{R}_K^{\frac{1}{2}}$  when  $\tilde{\lambda} = 0$ . Note that (5.41) is of same form used by [117] for full rank MVDR beamforming with diagonal loading. As summarized in Appendix C.1, an asymptotic, non-random form of (5.41) using  $\mathbf{v} = \mathbf{R}_K^{-\frac{1}{2}} \mathbf{a}$  and  $\mathbf{M} = \varepsilon \mathbf{R}_K^{-1}$  from (C.1) results in almost sure convergence given by

$$\mathbf{a}^H \left( \hat{\mathbf{R}}_K + \varepsilon \mathbf{I} \right)^{-1} \mathbf{a} \xrightarrow{as} \sum_{k=1}^M \frac{\mathbf{a}^H \mathbf{R}_K^{-\frac{1}{2}} \mathbf{u}_k \mathbf{u}_k^H \mathbf{R}_K^{-\frac{1}{2}} \mathbf{a} (1 + cb)}{1 + \lambda_k (\varepsilon \mathbf{R}_K^{-1}) (1 + cb)} \quad (5.42)$$

$$= \sum_{k=1}^M \frac{\mathbf{a}^H \mathbf{R}_K^{-\frac{1}{2}} \mathbf{u}_k \mathbf{u}_k^H \mathbf{R}_K^{-\frac{1}{2}} \mathbf{a} (1 + cb)}{1 + \varepsilon h_k^{-1} (1 + cb)} \quad (5.43)$$

$$(5.44)$$

where  $b = b(0)$  and defining

$$h_k = \begin{cases} \lambda_k & \text{if } k \leq K \\ \tilde{\lambda} & \text{if } K < k < M. \end{cases} \quad (5.45)$$

Thus using the eigenvalues of  $\mathbf{R}_K^{-\frac{1}{2}}$  as  $h_k^{-\frac{1}{2}}$

$$\mathbf{a}^H \left( \hat{\mathbf{R}}_K + \varepsilon \mathbf{I} \right)^{-1} \mathbf{a} \xrightarrow{as} \sum_{k=1}^M \frac{h_k^{-1} |\mathbf{a}^H \mathbf{u}_k|^2 (1 + cb)}{1 + \varepsilon h_k^{-1} (1 + cb)} \quad (5.46)$$

$$= \sum_{k=1}^M \frac{|\mathbf{a}^H \mathbf{u}_k|^2 (1 + cb)}{h_k + \varepsilon (1 + cb)}. \quad (5.47)$$

Substituting (5.47) into (5.39) provides an analytic, non-random form for desired signal power as

$$\sigma_s^2 |\mathbf{w}^H \mathbf{a}|^2 \xrightarrow{as} \sigma_s^2 \left| \sum_{k=1}^M \frac{|\mathbf{a}^H \mathbf{u}_k|^2 (1+cb)}{h_k + \varepsilon(1+cb)} \right|^2 / \kappa. \quad (5.48)$$

Now consider the received signal covariance matrix response given by

$$\mathbf{w}^H \mathbf{R} \mathbf{w} = \mathbf{a}^H \mathbf{R}^{\frac{1}{2}} \mathbf{R}_K^{-1} (\mathbf{W} + \varepsilon \mathbf{R}_K^{-1})^{-2} \mathbf{R}_K^{-1} \mathbf{R}^{\frac{1}{2}} \mathbf{a} / \kappa \quad (5.49)$$

with algebraic steps shown in Appendix C.2. Writing (5.49) in the form of (C.4) where  $\mathbf{a} = \mathbf{R}_K^{-1} \mathbf{R}^{\frac{1}{2}} \mathbf{a}_t$ ,  $\mathbf{M} = \varepsilon \mathbf{R}_K^{-1}$  results in

$$r'(z) = \mathbf{a}^H \mathbf{R}^{\frac{1}{2}} \mathbf{R}_K^{-1} (\mathbf{W} + \varepsilon \mathbf{R}_K^{-1} - z \mathbf{I})^{-2} \mathbf{R}_K^{-1} \mathbf{R}^{\frac{1}{2}} \mathbf{a} \quad (5.50)$$

which converges almost surely, see (C.5), to

$$\bar{r}'(z) = \sum_{k=1}^M \left| \mathbf{a}^H \mathbf{R}_K^{-1} \mathbf{R}^{\frac{1}{2}} \mathbf{u}_k \right|^2 \frac{(1+cb(z))^2 + cb'(z)}{\{(1 + (\lambda_k(\varepsilon \mathbf{R}_K^{-1}) - z)(1+cb(z))\}^2} \quad (5.51)$$

Thus using Appendix C.1 and (5.51) evaluated at  $z = 0$ , an asymptotic, non-random result for the power response is given by

$$\mathbf{w}^H \mathbf{R} \mathbf{w} \xrightarrow{as} \sum_{k=1}^M \left| \mathbf{a}^H \mathbf{R}_K^{-1} \mathbf{R}^{\frac{1}{2}} \mathbf{u}_k \right|^2 \frac{(1+cb)^2 + cb'}{\{1 + (\lambda_k(\varepsilon \mathbf{R}_K^{-1}) - z)(1+cb)\}^2} / \kappa. \quad (5.52)$$

Furthermore, (5.52) can be simplified using Appendix C.2 resulting in

$$\bar{r}'(z) = \sum_{k=1}^M |\mathbf{a}^H \mathbf{u}_k|^2 \lambda_k \frac{(1+cb)^2 + cb'}{\{h_k + \varepsilon(1+cb)\}^2}. \quad (5.53)$$

By substituting (5.52) and (5.48) into (5.37), the output SINR can be calculated analytically in terms of  $c$ . Note that a closed form solution of  $b$  only exists when  $c < 1$  [118] but this case is not the primary use for DMR beamformers.

## 5.7 Simulation Results

An interference dominated environment is simulated to demonstrate the performance of the proposed beamforming methods. In this section, a single near-field target is used. Consider a MRLA with 20 elements and effective aperture of a 126 element array at half-wavelength spacing (see [119]). The array configuration is shown in Figure 5.4, and the co-array is given in Figure 5.5 assuming weights equal to 1. Note that the maximum of the co-array is equal to the number of sensors, and the maximum lag is 125.

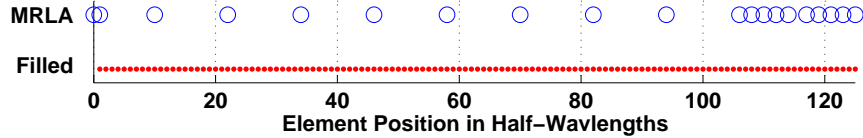


FIGURE 5.4: Array element positions for the MRLA and equivalent ULA

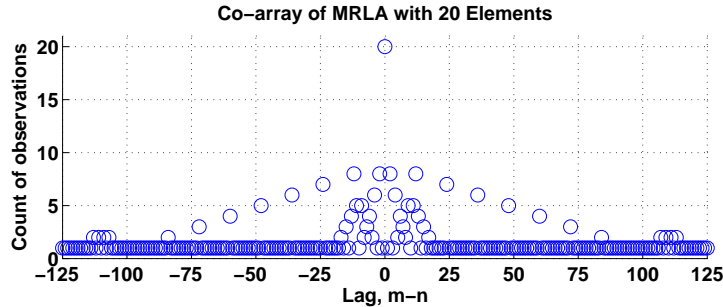


FIGURE 5.5: Co-array for 20 element MRLA

Interferers are assumed to be in the far-field randomly, uniformly distributed in bearing. The interference to noise ratio,  $[\Sigma]_{q,q}/\sigma_\eta^2$ , is assumed to be 20dB for each interferer. The signal to noise ratio for a single source,  $\sigma_s^2/\sigma_\eta^2$  is assumed to be 3 dB. Consider the beamformed output for a single realization of evenly spread interferers and target at  $110^\circ$  from endfire at a range of  $100\lambda$ . In this case, the received

data covariance matrix is assumed known. The case of 2 interferers is shown in Figure 5.6(a) for a filled 126 element ULA with conventional beamforming (5.22), the 20 element MRLA with MVDR weights ( $\tilde{\lambda} = \varepsilon = \sigma_\eta^2$ ) (5.29), and the modified augmented DMR weights from (5.36) using  $\tilde{\lambda} = \sigma_\eta^2$ . The interferer locations are denoted on the plots with a circle at the bottom of the plot. Conventional beamforming with uniform weighting has insufficient sidelobes in the far-field to suppress the interferers. The MRLA MVDR weights can adaptively null the interferers, and shows a source peak at the true location with power of 3 dB. The proposed weights, labeled Aug. DMR Mod., show increased sidelobes and reduced target peak compared to the ideal MVDR weights as a result of augmentation and reduced rank processing. The interference is expanded to 30 evenly spread point sources. Only the proposed method maintains performance in this case. Conventional processing with uniform weights has insufficient sidelobes, and MVDR processing only has 20 degrees of freedom for interference suppression. This results in high beamformer output regardless of steering direction, as shown in Figure 5.6(b). Note that MVDR beamforming with a known covariance for the MRLA array using augmentation also fails.

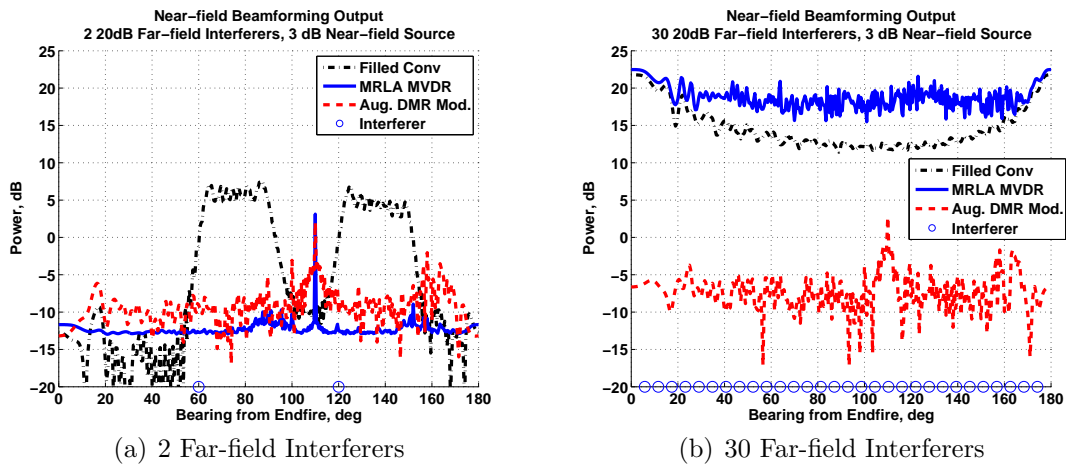


FIGURE 5.6: Near-field beamforming output with known covariance

Next the beamformer performance is considered for the case of a single interferer

and a far-field source with finite snapshots. The average array gain as a function of the number of snapshots,  $N$  is given by Figure 5.7. The MRLA MVDR beamformer weights are given by (5.29) using an estimated covariance matrix (equivalently (5.31) with  $K = M$ ) while the Aug. MVDR beamformer weights are given by (5.24). The MVDR RMT non-random result averaged over interferer/source locations is marked with triangles. For low number of samples, below 100, the Aug. MVDR approach has a higher average than the MRLA MVDR due to the averaging over spatial lags. The MRLA DMR approach, (5.31), performs better than either MVDR solution with limited snapshots. The RMT performance derived in Section 5.6 closely follows the MRLA DMR result but assumes  $\tilde{\lambda} = 0$ . The Aug. DMR approach, (5.35), closely approaches the upper bound given by  $M_\alpha(1 + \text{tr}(\Sigma_I)/\sigma_\eta^2) \approx 41$  dB. Additionally, 25th and 75th quantiles for the augmented approaches are given with thin dashed lines. The distribution of the Aug. DMR solution is tight around the mean. The distribution of the Aug. MVDR solution is not tight with 25th quantile at 15 dB, which is 15 dB below the mean of 30 dB.

Array Gain for 20 Element Array with 1 Far-field 20dB Interferer, Far-field 3 dB Source  
Average AG with 25% and 75% Quantiles

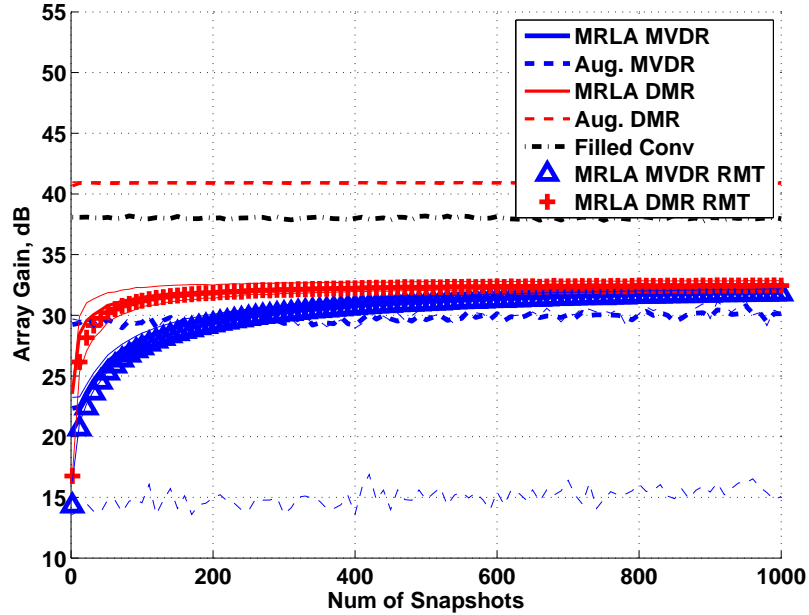


FIGURE 5.7: Average array gain with single far-field interferer and far-field source

Now consider the case of 30 far-field interferers and a far-field source given in Figure 5.8. In this case, the number of interferers exceeds the number of sensors of the MRLA. The array gain is only calculated when the number of snapshots is greater than the number of interferers. The MRLA MVDR and MRLA DMR weights are equivalent, since  $K = M$ , and the theoretical RMT predictions closely follow the simulated array gain converge. The MRLA non-augmented processing techniques have a maximum gain that is 13 dB below that of the filled array with conventional processing in this case. The augmented MRLA techniques result in a maximum of 126 degrees of freedom but only require 30 for interference suppression. The Aug. MVDR solution provides significant improvement over the non-augmented approaches, but the Aug. DMR weights provide an additional 10 dB in array gain. Neither method approaches the maximum  $M_\alpha(1 + \text{tr}(\Sigma_I)/\sigma_\eta^2) \approx 56$  dB using less than 1000 snapshots. The augmented methods have a large variance that is discussed later

but is not shown in the array gain plots for clarity. Note that array gain continues to increase with the number of snapshots for the range simulated. The traditional requirement for  $N = 2M$  or  $N = 2K$  snapshots for convergences does not apply to the proposed processing schemes due to augmentation.

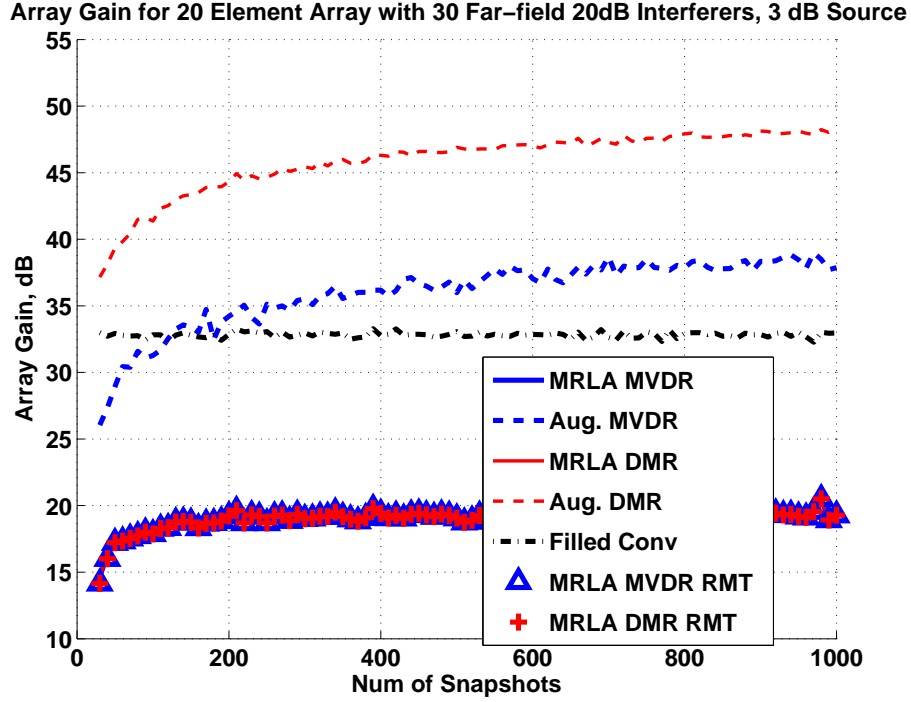


FIGURE 5.8: Average array gain with 30 far-field interferers and far-field source

The case of a single far-field interferer with a single near-field is considered in Figure 5.9. The non-augmented approaches, MRLA MVDR and MRLA DMR, do not exploit far-field assumptions and therefore have similar performance in the near-field and far-field cases. However, the augmented approaches have reduced performance compared to the far-field source case. The Aug. MVDR approach performs the worst and has lower array gain with more snapshots, which is a result of mismatch between the distorted near-field and the steering vector. The Aug. DMR method uses only the largest  $K$  eigenvalues. Assuming  $K$  strong interferers dominate the near-field sources, the near-field sources will not be in the dominate subspace and

self cancellation effects will be reduced. The 25th quantile in Figure 5.9 for MRLA DMR is lower than the non-augmented methods. Thus Aug. DMR has better average performance but greater probability of low array gain compared to conventional methods in this case.

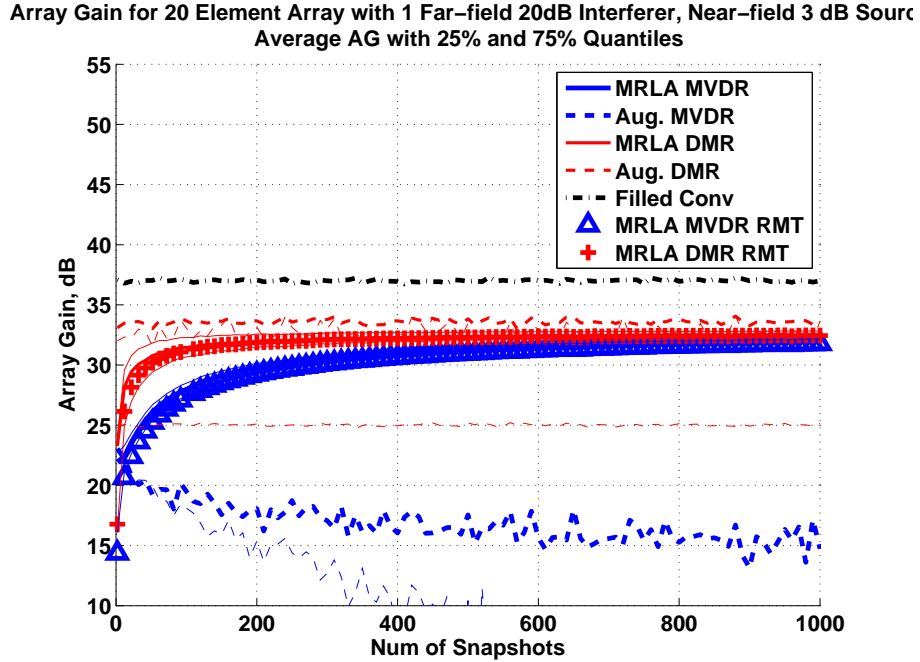


FIGURE 5.9: Average array gain with single far-field interferer and near-field source

The final configuration considered is 30 far-field interferers with a single near-field source, shown in Figure 5.10. Due to the large number of sources, the loss in signal power and mismatch is less than the suppression ability gained by augmentation. The MRLA MVDR and MRLA DMR methods are equivalent to each other and nearly equivalent to the gain in the far-field source case. The Aug. MVDR solution has an average that is consistently higher than the non-augmented solution. The Aug. DMR solution has an average array gain that is  $\approx 3$ dB higher than the Aug. MVDR solution. As also observed in the far-field case in Figure 5.8, the array gain for the adaptive augmented solutions increase even up to 1000 snapshots.

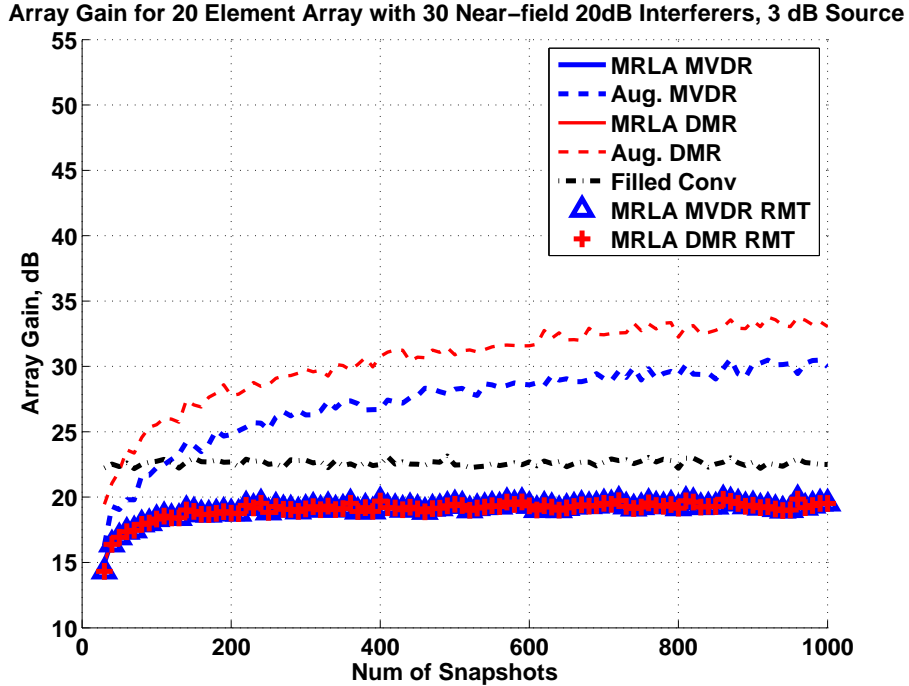


FIGURE 5.10: Average array gain with 30 far-field interferers and near-field source

In the previous plots, the average array gain was compared as a function of snapshots but the full distribution was not shown. The empirical cumulative distribution is calculated using Monte Carlo realizations as before. In order to compare the first proposed augmented DMR, (5.35) to the near-field modification, (5.36), the distribution is considered for a particular number of snapshots. Consider the single far-field interferer and near-field source case. The cumulative distribution function (CDF) of array gain from weights calculated using 10 snapshots is shown in Figure 5.11. The augmented DMR method shows a 20% probability of array gain of 25 dB or less. The maximum array gain of this method converges to the maximum array gain assuming infinite snapshots where the covariance matrix of a filled array  $\mathbf{R}_\alpha$  is assumed known, at  $M_\alpha(1 + \sigma_q^2/\sigma_\eta^2) \approx 41\text{dB}$ . Note that the array gain assuming a known covariance matrix is dependent on the interferer/source locations, which are random variables. The modified augmented DMR weights, from (5.36), have a maximum array gain of

$M(1 + \sigma_q^2 / \sigma_\eta^2) \approx 33$  that is less than the direct application of augmentation and DMR. However, the reduction in variance from ignoring the augmented dimensions in the steering vector is significant as 20% of the realizations have  $\approx 32$  dB or less compared to the original 25 dB. The trade-off between the original and modified processing is to increase the median performance (or lower variance) at the cost of the maximum performance. Note that the modified augmented DMR solution closely follows the solution when the signal covariance matrix is assumed known.

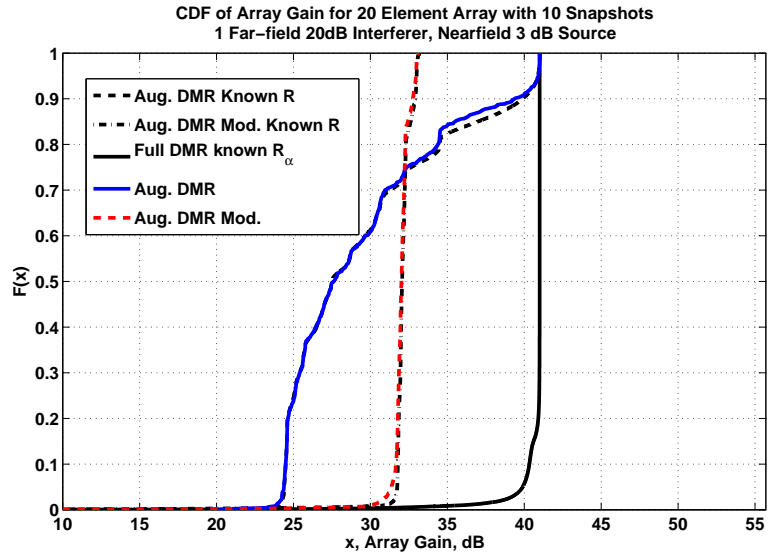


FIGURE 5.11: CDF of array gain with 1 far-field interferer and near-field source

The case of 30 far-field interferers and a single near-field source is considered in order to compare the original and modified augmented DMR solution. Unlike the single interferer case, the weights do not converge as quickly as a function of the number of snapshots. The augmented DMR and modified near-field weights are shown for 30, 100, and 1000 snapshots. Note that the median,  $F(x) = 0.5$ , is higher for the modified near-field approach, but the separation decreases with more snapshots in this range. Like the single interferer case, the modified approach shows a trade-off where the median and average performance is higher using the modified

steering vector, but the maximum array gain is reduced. The infinite snapshot case is also shown for both augmented DMR solutions as well as a filled array. Using 1000 snapshots, a significant gap (greater than 3dB typically used as a rule of thumb) still exists from the infinite snapshot case even though only 20 sensors and 30 degrees of freedom are used for interference suppression.

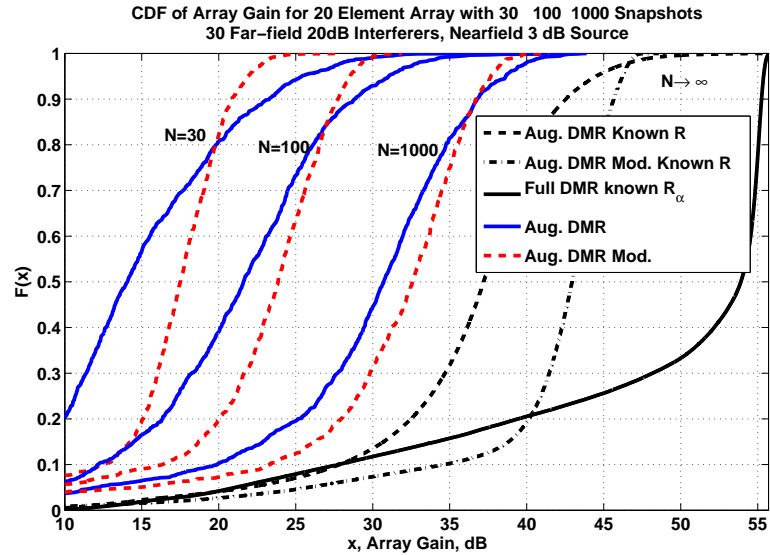


FIGURE 5.12: CDF of array gain with 30 far-field interferers and near-field source

## 5.8 Conclusion

Under-sampled linear arrays have an average inter-element spacing greater than a half-wavelength that results in array manifold ambiguities. Non-uniform spatial sampling is used to avoid spatial aliasing, and fully augmentable arrays are a class of NLAs that can be processed as a ULA with no manifold ambiguities through covariance matrix augmentation. The augmentation process can be used to detect the number of sources and estimate power, or source location, but does not allow the source signal waveform to be estimated. Additionally, the augmentation process increases the variance of source power estimates and thus requires more snapshots. In

order to reduce the sensitivity to the number of snapshots, rank reduced or DMR processing is proposed that increases array gain in interference dominated environments with limited number of snapshots. Near-field sources are considered and a modified steering vector is proposed in order to reduce the impact of augmentation on a non-stationary target. The modified, augmented DMR weights can suppress more interferers than the number of sensors and is more robust for near-field sources. Additionally, a method to analytically derive array gain performance for reduced rank processing schemes with diagonal loading is introduced.

# 6

## Concluding Remarks

Various problems in sensor array processing with omnidirectional elements are addressed in this work: spatial spectrum estimation with maneuvering arrays, array shape estimation during sharp turns, and fully augmentable static under-sampled arrays with limited snapshot support. Each of these problems have applications in underwater acoustic array signal processing, especially for towed hydrophone beamforming. While the problem of spatial spectrum estimation can be found in other sensing modalities, such as electromagnetics, the difficulties of dynamic array configurations is a focus of underwater acoustics where the speed of propagation is much slower.

Each of the particular problems addressed are briefly summarized in the context of array manifold ambiguities of nominally linear arrays. The most straight forward ambiguity for nominally linearly arrays in 3D space is the cone of angles/elevations with equivalent array manifold vectors. In 2D space, this corresponds to a left/right ambiguity for all angles  $\pm 180^\circ$  and can be resolved using either sufficient broadband temporal knowledge or time-varying array configurations. While recent literature considered spatial spectrum or field directionality mapping using time-varying array

shapes for pseudo-stationary fields, a formal framework is introduced here for a dynamic field using both stochastic and deterministic linear field directionality models. The field is approximated as sum of uncorrelated far-field sources at uniformly spaced grid points in bearing. For time-varying field parameters, the stochastic approach assumes a Gaussian noise model for changes in the field such that the previous time is used as a prior for the next update in a recursive manner. Both methods assume that the field changes slowly compared to the array shape/orientation and use an EM algorithm to calculate solutions. The deterministic solution models the changes in the field linearly but results in significant computational complexity as the solution is not recursive. The stochastic model is extended to the broadband case where the shape of the temporal spectrum is assumed known. This additional knowledge is shown to reduce the effects of spatial aliasing and results in significant detection gains for wideband signals. The principle idea is that the location of aliasing is dependent on temporal frequencies and uncertainty from aliasing can be reduced when knowledge of the (temporal) spectral shape is known.

The problem is then expanded to the case where the array shape is uncertain. The field directionality mapping algorithm is used in iteration with an acoustic-based array shape estimation technique that estimates the array shape by matching the received data with the previous field directionality map. In this case, the goal of the work is to form a robust array shape estimate that considers sources in the full  $360^\circ$ . Using the grid map field directionality model, ambiguities are resolved as the array shape or orientation changes allowing sources to be disambiguated, again assuming the field varies slowly compared to the array configuration. This solution can be physically motivated by exploiting the abundance of highly directional signals generated by shipping traffic on the edge of ocean basins. Such sources dominate ambient ocean noise at low frequencies across an ocean basin and form many peaks in bearing. Additionally, the acoustic-based array shape estimate is combined with

heading sensors located on the array and jointly filtered using dynamical motion models from literature. There appears to be no previous work in literature to statistically fuse organic positioning systems with in-band acoustic data for towed array shape estimation. The acoustic-based array shape estimate is more robust than previous approaches. Fusing heading data with the acoustic-based approach within the framework of a dynamical model provides a robust estimate that provides better performance than either approach individually.

Finally, the problem of manifold ambiguities for a static linear under-sampled array using only narrowband data is considered. While this problem is exacerbated in underwater acoustics due to the low sound speed, it also has applications for in-air acoustics and electromagnetics. The basic array processing problem is the trade-off between spatial resolution, which is only a function of aperture length, and maximum peak in the beampattern outside of the resolvable steered direction, which is a function of the number and placement of sensors. Note that the beampattern is also a function of the windowing technique. The more subtle issue of identifiability is considered where the rank of the interference subspace is less than the number of uncorrelated interferers. Previous literature has formally described identifiability but proposed complex iterative solutions for detecting sources. Fully augmentable arrays are used here, assuming wide sense stationary, in order to avoid manifold ambiguities. Methods based on fully and partially adaptive beamforming techniques are extended to the augmented domain. Additionally, interference dominated environments and snapshot limitation are considered. Reduced rank or partially adaptive algorithms are analyzed in snapshot deficient regime with diagonal loading. These algorithms are applied to augmented array data for MRLAs. The array gain performance for interference dominated environments is increased by suppressing more interferers than sensors as well as mitigating the impact of snapshot deficiency in the augmented domain. The case of a near-field source in far-field interference is also considered. A

modification of the steering vector is proposed in order to trade-off maximum array gain for a small variance. This is shown to improve average and median performance by weighting the augmented dimensions less.

## Future Work

The future work for the towed array shape estimation problem is considered:

### **3D case: elevation**

The dynamical model for the towed array shape extends to the 3D case. Tilt of the array causing an elevation component results in an other parameter that can be treated in the same way as  $\theta$ . However, organic positions sensors such as depth sensors do not directly measure elevation and therefore must be incorporated via the model. Additionally, the bearing grid can be extended to include elevation.

### **Array shape estimation bounds in wavelengths**

The bound of RMSE of hydrophone position appears to be near  $0.1 \lambda$  based on the Monte Carlo results. While the CRLB for array curvature was calculated, the bound as a function of hydrophone locations in Cartesian space was not calculated. Several members at GTRI, JHU/APL, and NRL have suggested that this empirical bound is common throughout array processing but no analytical proof has been derived. This should be investigated as a function of the number of array shape parameters and the directionality of the field.

### **Array gain from shape estimation**

The change in array gain for adaptive beamforming methods with and without array shape estimation should be studied. Assuming a lower bound for array shape estimation, the maximum achievable array gain should be found.

The under-sampled array work is a more basic problem that has significantly more work that can be done in the future:

### **Optimal diagonal loading factor**

An analytical result for array gain as a function of the number of snapshots and diagonal loading for partially adaptive processing was derived. However, the diagonal loading factor was assumed known. A method to estimate the optimal diagonal loading factor should be derived.

### **Near-field source steering vector modification**

In this work, a modification for steering vectors using the augmented covariance matrix resulted in higher average array gain by placing zeros in locations of the augmented dimensions. An approach that optimally determines the weighting for a source should be considered in order to exploitly trade-off between the maximum and variance of array gain. Consider optimal combination of augmented weights instead of selective zeroing.

### **Distributions for SINR or array gain for rank reduced algorithms**

Since the covariance matrix used for the rank reduced weights are not equivalent, or even converge in samples, to the data covariance matrix, the distribution of array gain is unknown. The statistics of array gain for a set array configuration using rank reduced methods should be derived using the central limit theorem or another asymptotic method. Hopefully, this will result in environment invariant statistics for array gain loss from optimal.

### **Analytical form of near-field source augmented covariance matrix**

A closed form solution for the near-field source augmented covariance matrix can be used to determine array gain as compared to the far-field case. Note that signal mismatch will result in a loss of signal power but provides a bet-

ter estimate of the interference and noise covariance matrix. This should be compared to spatial smoothing.

### **Interference subspace sensitivity**

In this work, the interference subspace size was assumed known. While estimating the subspace size of dominate interference has been solved, the sensitivity to under or over estimating the dimensionality of the interference should be investigated for the proposed methods.

### **Extensions to broadband case**

Augmentation for broadband data is not obvious but is an active area of research. The effects of isotopic noise must be considered in the wideband case. Augmentation over a wideband will result in over-sampling where isotopic noise will no longer appear white.

# Appendix A

## Second Order Expectation Approximation

Consider a function  $g(x)$  with parameter  $x$ . The first three terms in the Taylor's series expansion around  $\mu$  are  $g(x) = g(\mu) + g'(\mu)(x - \mu) + \frac{1}{2}g''(\mu)(x - \mu)^2$ . Assuming  $x$  has a mean  $\mu$  and variance  $\sigma^2$ , then  $E[g(x)] \approx g(\mu) + \frac{\sigma^2}{2}g''(\mu)$ . This is essentially a local approximation of  $g(x)$  assuming the pdf is tight around  $x$  near  $\mu$ . The multivariate equivalent for  $\mathbf{x}$  with mean  $\boldsymbol{\mu}$  and covariance  $\mathbf{R}$  is  $E[g(\mathbf{x})] \approx g(\boldsymbol{\mu}) + \frac{1}{2}\text{Tr}[\mathbf{R}H_{\boldsymbol{\mu}}g(\mathbf{x})]$ , where  $\text{Tr}$  is trace and  $H_{\mathbf{x}}$  is the Hessian with respect to  $\mathbf{x}$  evaluated at  $\boldsymbol{\mu}$ . The approximation applied to the term in brackets from (4.19) is analogous to assuming the field does not vary quickly between time instances. The joint pdf from (4.19) is written as

$$f(\mathcal{C}_N(n), \boldsymbol{\Sigma}(n)) = \alpha + f(\mathbf{s}(n), \boldsymbol{\eta}(n) | \boldsymbol{\Sigma}(n)) \prod_{k=n-N+1}^{n-1} G(\mathbf{s}(k); \mathbf{0}, \boldsymbol{\Sigma}(n)) + \frac{1}{2}\text{Tr}[\mathbf{R}H_{\boldsymbol{\Sigma}_n}G(\mathbf{s}(k); \mathbf{0}, \boldsymbol{\Sigma}(n))], \quad (\text{A.1})$$

where  $\alpha$  is not a function of  $\boldsymbol{\Sigma}(n)$  or  $\mathbf{x}_n$ . The covariance matrix of  $\boldsymbol{\Delta}$  is represented by  $\mathbf{R}$ . Let the diagonal of the covariance be denoted  $[\mathbf{R}]_{qq} = r_q^2$  for the  $q$ th element.

Taking the natural log of (A.1) results in

$$\ln f(\mathcal{C}_N(n), \mathbf{\Sigma}(n)) \propto \sum_{k=n-N+1}^n \ln G(\mathbf{s}(k); \mathbf{0}, \mathbf{\Sigma}(n)) + \sum_{k=n-N+1}^{n-1} l_k \quad (\text{A.2})$$

where

$$l_k = \ln \left[ 1 + \frac{1}{2} \text{Tr} \left[ \mathbf{S} \left( \mathbf{\Sigma}^{-1}(n) \mathbf{s}(k) \mathbf{s}(k)^H \mathbf{\Sigma}^{-1}(n) - \mathbf{\Sigma}^{-1}(n) \right) \right] \right] \quad (\text{A.3})$$

$$\approx \frac{1}{2} \sum_{q=1}^Q \frac{d_q^2 |s_q(k)|^2}{([\mathbf{\Sigma}]_{qq})^2(n)} - \frac{d_q^2}{[\mathbf{\Sigma}]_{qq}}. \quad (\text{A.4})$$

When the spectrum changes slowly, the standard deviation  $r_q$  and the resulting  $l_k$  are small and allows for the approximation of  $\ln$  given by (A.4).

# Appendix B

## Cramér-Rao Bounds

The Cramér-Rao bound on the spatial spectrum estimate given the model from Section 4.3 is in general expressed by (4.26). Defining a form of the parameter vector  $\bar{\sigma} = [\sigma_1^2(\omega_1), \dots, \sigma_Q^2(\omega_1), \sigma_1^2(\omega_2), \dots, \sigma_Q^2(\omega_B)]$ , with order sources then frequencies, creates a structured Fisher information matrix.

$$\mathbf{J} = \begin{bmatrix} \mathbf{J}(\omega_1) & & \mathbf{0} \\ & \ddots & \\ \mathbf{0} & & \mathbf{J}(\omega_B) \end{bmatrix}.$$

The full ML method estimates each frequency and then averages the estimates, thus the bound must introduce an additional parameter  $\sigma_q = \frac{1}{B} \sum_{b=1}^B \sigma_q^2(\omega_b)$ . The resulting Fisher information matrix is denoted  $\mathbf{J}_c$ .

$$[\mathbf{J}_c] = \begin{bmatrix} \mathbf{J} & \mathbf{J}_{\bar{\sigma}\sigma} \\ \mathbf{J}_{\sigma\bar{\sigma}} & \mathbf{J}_\sigma \end{bmatrix}$$

The inverse can be written in the form  $[\mathbf{J}_c]_\sigma^{-1} = \mathbf{H}^H \mathbf{J}^{-1} \mathbf{H}$  where  $[\mathbf{H}]_{ab} = \frac{\partial \sigma_b^2}{\partial \sigma_a^2}$ . [120, p. 230] The effect of  $\mathbf{H}$  in matrix form is to perform the addition on each estimate,

and the bound can be rewritten

$$\mathbf{J}_c^{-1} = \frac{1}{B^2} \sum_{b=1}^B \mathbf{J}^{-1}(\omega_b). \quad (\text{B.1})$$

The reduced ML method assumes a single parameter is used for each source and results in a parameter vector  $\bar{\boldsymbol{\sigma}} = [\sigma_1^2, \dots, \sigma_Q^2]$ . This broadband derivation uses only  $Q$  parameters with FIM denoted  $\mathbf{J}_B$ , resulting directly from (4.27) and inverse expressed as (B.2).

$$\begin{aligned} \mathbf{J}_B &= \sum_{b=1}^B \mathbf{J}(\omega_b) \\ \mathbf{J}_B^{-1} &= \left[ \sum_{b=1}^B \mathbf{J}(\omega_b) \right]^{-1} \end{aligned} \quad (\text{B.2})$$

It is useful to consider the partitioned case for a single variable without loss of generality

$$\mathbf{J}(\omega_b) = \begin{bmatrix} J_{11} & \mathbf{J}_{21}^T \\ \mathbf{J}_{21} & \mathbf{J}_{22} \end{bmatrix}$$

where all elements of  $\mathbf{J}$  are non-negative and  $\mathbf{J}_{22}$  is positive semidefinite. Note that the bound on the parameter is

$$\begin{aligned} J_{11} &= [J_{11} - \mathbf{J}_{21}^T \mathbf{J}_{22}^{-1} \mathbf{J}_{21}]^{-1} \\ J_{11} &\geq J_{11}^{-1} \\ [\mathbf{J}^{-1}]_{qq} &\geq \{[\mathbf{J}]_{qq}\}^{-1} \end{aligned} \quad (\text{B.3})$$

where the new bound is *looser* than the CRB but provides an approximation at least as low as the CRB.

# Appendix C

## Derivations for Asymptotic Performance Results

### C.1 Relevant Results from Random Matrix Theory

The following are the core results as summarized by Mestre and Lagunas [117]. Consider deterministic parameters  $\mathbf{M}$ ,  $z$ ,  $\mathbf{a}$ , and the random matrix  $\mathbf{W}$ , where  $\mathbf{W} = \frac{1}{N}\mathbf{\Xi}\mathbf{\Xi}^H$ ,  $\mathbf{\Xi}$  is  $M \times N$ ,  $\mathbf{\Xi} \sim \mathcal{CN}(\mathbf{0}, \mathbf{I})$ . Eigendecomposition given by  $\mathbf{M} = \sum_{k=1}^M \lambda_k(\mathbf{M})\mathbf{u}_k\mathbf{u}_k^H$ . Almost sure convergence,  $\xrightarrow{as}$ , means here that convergence occurs with probability 1 within the region of  $|z| < \lambda_K(\mathbf{M})/3$  in the limit as  $N, M \rightarrow \infty$  for  $c = \frac{M}{N}$  (assuming bounded, non-zero eigenvalues of  $\mathbf{M} + \mathbf{W}$  and bounded moments)

$$r(z) = \mathbf{v}^H (\mathbf{W} + \mathbf{M} - z\mathbf{I})^{-1} \mathbf{v} \xrightarrow{as} \bar{r}(z) \quad (\text{C.1})$$

$$\bar{r}(z) = \sum_{k=1}^M \frac{\mathbf{v}^H \mathbf{u}_k \mathbf{u}_k^H \mathbf{v} (1 + cb(z))}{1 + (\lambda_k(\mathbf{M}) - z)(1 + cb(z))} \quad (\text{C.2})$$

$$b(z) = \frac{1}{M} \sum_{k=1}^M \frac{1 + cb(z)}{1 + (\lambda_k(\mathbf{M}) - z)(1 + cb(z))} \quad (\text{C.3})$$

where  $b(z)$  solution must be positive. Note that

$$\frac{dr}{dz} = r'(z) = \mathbf{v}^H (\mathbf{W} + \mathbf{M} - z\mathbf{I})^{-2} \mathbf{v} \quad (\text{C.4})$$

$$\frac{d\bar{r}}{dz} = \bar{r}'(z) = \sum_{k=1}^M \mathbf{v}^H \mathbf{u}_k \mathbf{u}_k^H \mathbf{v} \frac{(1 + cb(z))^2 + cb'(z)}{\{1 + (\lambda_k(\mathbf{M}) - z)(1 + cb(z))\}^2} \quad (\text{C.5})$$

Since  $r(z) \xrightarrow{as} \bar{r}(z)$ , then  $r'(z) \xrightarrow{as} \bar{r}'(z)$ .

$$b'(z=0) = \left(1 - \frac{1}{M} \sum_{k=1}^M \frac{c\lambda_k^2}{(\lambda_k + \varepsilon(1 + cb))^2}\right)^{-1} \frac{1}{M} \sum_{k=1}^M \frac{\lambda_k^2(1 + cb)^2}{(\lambda_k + \varepsilon(1 + cb))^2} \quad (\text{C.6})$$

## C.2 Simplification of (5.49) and (5.52)

The following was used to simplify (5.49) and (5.52) The beamformed power output using weights from (5.31) and the ensemble received signal covariance matrix are given by

$$\mathbf{w}^H \mathbf{R} \mathbf{w} = \mathbf{a}^H \left(\hat{\mathbf{R}}_K + \varepsilon \mathbf{I}\right)^{-1} \mathbf{R} \left(\hat{\mathbf{R}}_K + \varepsilon \mathbf{I}\right)^{-1} \mathbf{a} \quad (\text{C.7})$$

$$= \mathbf{a}^H \left(\mathbf{R}_K^{\frac{1}{2}} \mathbf{W} \mathbf{R}_K^{\frac{1}{2}} + \varepsilon \mathbf{I}\right)^{-1} \mathbf{R} \left(\mathbf{R}_K^{\frac{1}{2}} \mathbf{W} \mathbf{R}_K^{\frac{1}{2}} + \varepsilon \mathbf{I}\right)^{-1} \mathbf{a} \quad (\text{C.8})$$

$$= \mathbf{a}^H \mathbf{R}_K^{-\frac{1}{2}} (\mathbf{W} + \varepsilon \mathbf{R}_K^{-1})^{-1} \mathbf{R}_K^{-\frac{1}{2}} \mathbf{R} \mathbf{R}_K^{-\frac{1}{2}} (\mathbf{W} + \varepsilon \mathbf{R}_K^{-1})^{-1} \mathbf{R}_K^{-\frac{1}{2}} \mathbf{a} \quad (\text{C.9})$$

$$= \mathbf{a}^H \mathbf{R}^{-\frac{1}{2}} \mathbf{R}_K^{\frac{1}{2}} \mathbf{R}_K^{-\frac{1}{2}} (\mathbf{W} + \varepsilon \mathbf{R}_K^{-1})^{-1} \mathbf{R}_K^{-\frac{1}{2}} \mathbf{R}_K^{\frac{1}{2}} \mathbf{R}_K^{-\frac{1}{2}} (\mathbf{W} + \varepsilon \mathbf{R}_K^{-1})^{-1} \mathbf{R}_K^{-\frac{1}{2}} \mathbf{R}_K^{\frac{1}{2}} \mathbf{R}^{-\frac{1}{2}} \mathbf{a} \quad (\text{C.10})$$

$$= \mathbf{a}^H \mathbf{R}^{-\frac{1}{2}} \left(\mathbf{R}_K^{\frac{1}{2}} \mathbf{R}_K^{-\frac{1}{2}} (\mathbf{W} + \varepsilon \mathbf{R}_K^{-1})^{-1} \mathbf{R}_K^{-\frac{1}{2}} \mathbf{R}_K^{\frac{1}{2}}\right)^2 \mathbf{R}^{-\frac{1}{2}} \mathbf{a} \quad (\text{C.11})$$

$$= \mathbf{a}^H \mathbf{R}_K^{\frac{1}{2}} \mathbf{R}_K^{-1} (\mathbf{W} + \varepsilon \mathbf{R}_K^{-1})^{-2} \mathbf{R}_K^{-1} \mathbf{R}_K^{\frac{1}{2}} \mathbf{a} \quad (\text{C.12})$$

Using the eigendecomposition of  $\mathbf{R}_K = \sum_{k=1}^M h_k \mathbf{u}_k \mathbf{u}_k^H$  and  $\mathbf{R} = \sum_{k=1}^M \lambda_k \mathbf{u}_k \mathbf{u}_k^H$  and exploiting the common eigenvectors,

$$\mathbf{R}_K^{-1} \mathbf{R}_K^{\frac{1}{2}} = \sum_{k=1}^M h_k^{-1} \lambda_k^{\frac{1}{2}} \mathbf{u}_k \mathbf{u}_k^H \quad (\text{C.13})$$

therefore

$$\left| \mathbf{a}^H \mathbf{R}_K^{-1} \mathbf{R}_K^{\frac{1}{2}} \mathbf{u}_k \right|^2 = \left| \mathbf{a}^H \mathbf{u}_k \right|^2 h_k^{-2} \lambda_k \quad (\text{C.14})$$

# Bibliography

- [1] H. Krim and M. Viberg, “Two decades of array signal processing research: the parametric approach,” *IEEE Signal Process. Mag.*, vol. 13, no. 4, pp. 67–94, 1996.
- [2] W. Hodgkiss, “The effects of array shape perturbation on beamforming and passive ranging,” *IEEE J. Ocean. Eng.*, vol. 8, no. 3, pp. 120–130, Jul. 1983.
- [3] B. D. Van Veen and K. M. Buckley, “Beamforming: a versatile approach to spatial filtering,” *IEEE ASSP Mag.*, vol. 5, no. 2, pp. 4–24, Apr. 1988.
- [4] W. S. Hodgkiss and L. W. Nolte, “Covariance between fourier coefficients representing the time waveforms observed from an array of sensors,” *J. Acoust. Soc. Am.*, vol. 59, no. 3, pp. 582–590, 1976.
- [5] H. L. Van Trees, *Optimum Array Processing*. John Wiley & Sons, Inc., 2002.
- [6] R. Wagstaff, “Iterative technique for ambient-noise horizontal-directionality estimation from towed line-array data,” *J. Acoust. Soc. Am.*, vol. 63, pp. 863–869, 1978.
- [7] N.-C. Yen and W. Carey, “Application of synthetic-aperture processing to towed-array data,” *J. Acoust. Soc. Am.*, vol. 86, no. 2, pp. 754–765, 1989.
- [8] S. Stergiopoulos and H. Urban, “A new passive synthetic aperture technique for towed arrays,” *IEEE J. Ocean. Eng.*, vol. 17, no. 1, pp. 16–25, 1992.
- [9] E. J. Sullivan, J. D. Holmes, W. M. Carey, and J. F. Lynch, “Broadband passive synthetic aperture: Experimental results,” *J. Acoust. Soc. Am.*, vol. 120, no. 4, pp. EL49–EL54, 2006.
- [10] H. Cox, “Resolving power and sensitivity to mismatch of optimum array processors,” *J. Acoust. Soc. Am.*, vol. 54, no. 3, pp. 771–785, 1973.
- [11] J. Capon, “High-resolution frequency-wavenumber spectrum analysis,” *Proc. IEEE*, vol. 57, no. 8, pp. 1408–1418, 1969.
- [12] R. Monzingo and T. Miller, *Introduction to Adaptive Arrays*. John Wiley & Sons, 1980.

- [13] A. Zeira and B. Friedlander, "Direction finding with time-varying arrays," *IEEE Trans. Signal Process.*, vol. 43, no. 4, pp. 927–937, Apr. 1995.
- [14] B. Friedlander and A. Zeira, "Eigenstructure-based algorithms for direction finding with time-varying arrays," *IEEE Trans. Aerosp. Electron. Syst.*, vol. 32, no. 2, pp. 689–701, Apr. 1996.
- [15] H. Wang and M. Kaveh, "Coherent signal-subspace processing for the detection and estimation of angles of arrival of multiple wide-band sources," *IEEE Trans. Acoust., Speech, Signal Process.*, vol. 33, no. 4, pp. 823–831, 1985.
- [16] J. Krolik and D. Swingler, "Multiple broad-band source location using steered covariance matrices," *IEEE Trans. Acoust., Speech, Signal Process.*, vol. 37, no. 10, pp. 1481–1494, Oct. 1989.
- [17] P. Gerstoft, W. Hodgkiss, W. Kuperman, H. Song, M. Siderius, and P. Nielsen, "Adaptive beamforming of a towed array during a turn," *IEEE J. Ocean. Eng.*, vol. 28, no. 1, pp. 44–54, 2003.
- [18] M. V. Greening and J. E. Perkins, "Adaptive beamforming for nonstationary arrays," *J. Acoust. Soc. Am.*, vol. 112, no. 6, pp. 2872–2881, 2002.
- [19] Y. Lee, W. Lee, and A. Lee, "Synthetic stationary array processing for a towed array in maneuver," *J. Acoust. Soc. Am.*, vol. 120, no. 5, pp. 3049–3049, 2006.
- [20] D. Fuhrmann, "Structured covariance estimation: Theory, application, and recent results," in *4th IEEE Workshop on Sensor Array and Multichannel Processing*, Jul. 2006, pp. 0–62.
- [21] J. P. Burg, D. G. Luenberger, and D. L. Wenger, "Estimation of structured covariance matrices," *Proc. IEEE*, vol. 70, no. 9, pp. 963–974, 1982.
- [22] J. Bohme, "Estimation of source parameters by maximum likelihood and non-linear regression," in *IEEE International Acoustics, Speech, and Signal Processing Conf.*, vol. 9, 1984, pp. 271–274.
- [23] A. P. Dempster, N. M. Laird, and D. B. Rubin, "Maximum likelihood from incomplete data via the EM algorithm," *J. Royal Statistical Soc. Series B (Methodological)*, vol. 39, no. 1, pp. 1–38, 1977.
- [24] M. Feder and E. Weinstein, "Parameter estimation of superimposed signals using the em algorithm," *IEEE Trans. Acoust., Speech, Signal Process.*, vol. 36, no. 4, pp. 477–489, Apr. 1988.
- [25] M. Miller and D. Fuhrmann, "Maximum-likelihood narrow-band direction finding and the em algorithm," *IEEE Trans. on Acoustics, Speech, and Signal Processing*, vol. 38, no. 9, pp. 1560–1577, 1990.

- [26] P. Chung and J. Bohme, “Experimental study of the EM and SAGE algorithms with application to sonar data,” in *IEEE Sensor Array and Multichannel Signal Processing Workshop Proc.*, 2002, pp. 77–81.
- [27] A. Lanterman, “Statistical radar imaging of diffuse and specular targets using an expectation-maximization algorithm,” in *SPIE Conf. Series*, vol. 4053, 2000, pp. 20–31.
- [28] —, “Statistical imaging in radio astronomy via an expectation-maximization algorithm for structured covariance estimation,” 2000, to appear in *Statistical Methods in Imaging: In Medicine, Optics, and Communication*, a festschrift in honor of Donald L. Snyder’s 65th birthday.
- [29] A. Baggeroer and H. Cox, “Passive sonar limits upon nulling multiple moving ships with large aperture arrays,” in *Conf. Rec. of the 33rd Asilomar Conf. on Signals, Systems, and Computers*, vol. 1, 1999, pp. 103–108.
- [30] J. Capon and N. Goodman, “Probability distributions for estimators of the frequency-wavenumber spectrum,” *Proc. IEEE*, vol. 58, no. 10, pp. 1785–1786, 1970.
- [31] D. Abraham and N. Owsley, “Beamforming with dominant mode rejection,” in *Conf. Proc. OCEANS*, Sep. 1990, pp. 470–475.
- [32] A. Kraay and A. Baggeroer, “A physically constrained maximum-likelihood method for snapshot-deficient adaptive array processing,” *IEEE Trans. Signal Process.*, vol. 55, no. 8, pp. 4048–4063, Aug. 2007.
- [33] J. Rogers and J. Krolik, “Time-varying spatial spectrum estimation with a maneuverable towed array,” *J. Acoust. Soc. Am.*, vol. 128, no. 6, pp. 3543–3553, 2010.
- [34] —, “An online method for time-varying spatial spectrum estimation using a towed acoustic array,” in *Conf. Rec. of the Forty Fourth Asilomar Conf. on Signals, Systems and Computers*, 2010, pp. 1837–1841.
- [35] I. Schurman, “Reverberation rejection with a dual-line towed array,” *IEEE J. Ocean. Eng.*, vol. 21, no. 2, pp. 193–204, 1996.
- [36] N. Owsley and G. Swope, “Time delay estimation in a sensor array,” *IEEE Trans. Acoust., Speech, Signal Process.*, vol. 29, no. 3, pp. 519–523, 1981.
- [37] B. Sotirin and J. Hildebrand, “Large aperture digital acoustic array,” *IEEE J. Ocean. Eng.*, vol. 13, no. 4, pp. 271–281, 1988.

- [38] D. Gray, B. Anderson, and R. Bitmead, "Towed array shape estimation using Kalman filters-theoretical models," *IEEE J. Ocean. Eng.*, vol. 18, no. 4, pp. 543–556, 1993.
- [39] Y. Rockah and P. Schultheiss, "Array shape calibration using sources in unknown locations—part I: Far-field sources," *IEEE Trans. Acoust., Speech, Signal Process.*, vol. 35, no. 3, pp. 286–299, Mar. 1987.
- [40] M. Viberg and A. Swindlehurst, "A bayesian approach to auto-calibration for parametric array signal processing," *IEEE Trans. Signal Process.*, vol. 42, no. 12, pp. 3495–3507, 1994.
- [41] M. Paidoussis, "Dynamics of flexible slender cylinders in axial flow," *J. of Fluid Mechanics*, vol. 26, pp. 717–736, 1966.
- [42] R. M. Kennedy, "Crosstrack dynamics of a long cable towed in the ocean," in *Proc. OCEANS 81*, 1981, pp. 966–970.
- [43] P. Tichavsky and K. Wong, "Quasi-fluid-mechanics-based quasi-bayesian crame acute;r-rao bounds for deformed towed-array direction finding," *IEEE Trans. Signal Process.*, vol. 52, no. 1, pp. 36–47, Jan. 2004.
- [44] J. Smith, Y. Leung, and A. Cantoni, "The Cramér-Rao lower bound for towed array shape estimation with a single source," *IEEE Trans. Signal Process.*, vol. 44, no. 4, pp. 1033–1036, 1996.
- [45] H.-Y. Park, C. Lee, H.-G. Kang, and D.-H. Youn, "Generalization of the subspace-based array shape estimations," *IEEE J. Ocean. Eng.*, vol. 29, no. 3, pp. 847–856, 2004.
- [46] H.-Y. Park, K.-M. Kim, H.-W. Kang, D.-H. Youn, and C. Lee, "A simplified subspace fitting method for estimating shape of a towed array," *IEEE J. Ocean. Eng.*, vol. 33, no. 2, pp. 215–223, 2008.
- [47] V. Varadarajan and J. Krolik, "Array shape estimation tracking using active sonar reverberation," *IEEE Trans. Aerosp. Electron. Syst.*, vol. 40, no. 3, pp. 1073–1086, Jul. 2004.
- [48] N. Owsley, "Shape estimation for a flexible underwater cable," *Proc. IEEE EASCON*, pp. 22–23, 1981.
- [49] B. Howard and J. Syck, "Calculation of the shape of a towed underwater acoustic array," *IEEE J. Ocean. Eng.*, vol. 17, no. 2, pp. 193–203, 1992.
- [50] B. Newhall, J. Jenkins, and J. Dietz, "Improved estimation of the shape of towed sonar arrays," in *Instrumentation and Measurement Technology Conference*, vol. 2. IEEE, 2004, pp. 873–876.

- [51] G. Wenz, “Acoustic ambient noise in the ocean: Spectra and sources,” *J. Acoust. Soc. Am.*, vol. 34, pp. 1936–1956, 1962.
- [52] W. M. Carey and R. B. Evans, *Ocean Ambient Noise Measurement and Theory: Measurement and Theory*. Springer, 2011.
- [53] R. Wagstaff, “An ambient noise model for the northeast pacific ocean basin,” *IEEE J. Ocean. Eng.*, vol. 30, pp. 286–294, 2005.
- [54] A. Weiss and B. Friedlander, “Array shape calibration using sources in unknown locations—a maximum likelihood approach,” *IEEE Trans. Acoust., Speech, Signal Process.*, vol. 37, no. 12, pp. 1958–1966, 1989.
- [55] A. J. Weiss and B. Friedlander, “Array shape calibration using eigenstructure methods,” *Signal Processing*, vol. 22, no. 3, pp. 251–258, 1991.
- [56] D. Wahl, “Towed array shape estimation using frequency-wavenumber data,” *IEEE J. Ocean. Eng.*, vol. 18, no. 4, pp. 582–590, 1993.
- [57] B. Ferguson, “Remedying the effects of array shape distortion on the spatial filtering of acoustic data from a line array of hydrophones,” *IEEE J. Ocean. Eng.*, vol. 18, no. 4, pp. 565–571, 1993.
- [58] L. C. Godara, “Application of antenna arrays to mobile communications. ii. beam-forming and direction-of-arrival considerations,” *Proc. IEEE*, vol. 85, no. 8, pp. 1195–1245, 1997.
- [59] B. Flanagan and K. Bell, “Array self-calibration with large sensor position errors,” *Signal Processing*, vol. 81, no. 10, pp. 2201–2214, 2001.
- [60] J. Goldberg, “Joint direction-of-arrival and array-shape tracking for multiple moving targets,” *IEEE J. Ocean. Eng.*, vol. 23, no. 2, pp. 118–126, 1998.
- [61] A. Weiss and B. Friedlander, ““Almost blind” steering vector estimation using second-order moments,” *IEEE Trans. Signal Process.*, vol. 44, no. 4, pp. 1024–1027, 1996.
- [62] P.-J. Chung and S. Wan, “Array self-calibration using SAGE algorithm,” in *IEEE Sensor Array and Multichannel Signal Processing Workshop*, 2008, pp. 165–169.
- [63] J. A. Fessler and A. O. Hero, “Space-alternating generalized expectation-maximization algorithm,” *IEEE Trans. Signal Process.*, vol. 42, no. 10, pp. 2664–2677, 1994.
- [64] P. Chung and J. Bohme, “Recursive EM and SAGE-inspired algorithms with application to DOA estimation,” *IEEE Trans. Signal Process.*, vol. 53, no. 8, pp. 2664–2677, 2005.

- [65] P. Stoica and A. Nehorai, “Performance study of conditional and unconditional direction-of-arrival estimation,” *IEEE Trans. Acoust., Speech, Signal Process.*, vol. 38, no. 10, pp. 1783–1795, 1990.
- [66] A. Paulraj and T. Kailath, “Direction of arrival estimation by eigenstructure methods with unknown sensor gain and phase,” in *IEEE International Conference on Acoustics, Speech, and Signal Processing, ICASSP ’85.*, vol. 10, Apr. 1985, pp. 640–643.
- [67] A. Jaffer, “Maximum likelihood direction finding of stochastic sources: a separable solution,” in *IEEE Int. Conf. on Acoustics, Speech, and Signal Processing*, vol. 5, Apr. 1988, pp. 2893–2896.
- [68] M. Pesavento, A. Gershman, and K. M. Wong, “Direction of arrival estimation in partly calibrated time-varying sensor arrays,” in *IEEE International Conference on Acoustics, Speech, and Signal Processing ICASSP ’01*, vol. 5, 2001, pp. 3005–3008.
- [69] L. Lei, J. Lie, A. Gershman, and C. See, “Robust adaptive beamforming in partly calibrated sparse sensor arrays,” *IEEE Trans. Signal Process.*, vol. 58, no. 3, pp. 1661–1667, Mar. 2010.
- [70] S. Wan, “Parameteric array calibration,” Ph.D. dissertation, University of Edinburgh, 2011.
- [71] W. Bangs, “Array processing with generalized beam-formers,” Ph.D. dissertation, Yale Univ., 1971.
- [72] J. Odom, “Spatial spectrum estimation with a maneuvering sensor array in a dynamic environment,” Master’s thesis, Duke Uni., Sept. 2011.
- [73] T. Wettergren, “Performance of search via track-before-detect for distributed sensor networks,” *IEEE Trans. Aerosp. Electron. Syst.*, vol. 44, no. 1, pp. 314–325, Jan. 2008.
- [74] S. Hayward, “Adaptive beamforming for rapidly moving arrays,” in *CIE Int. Conf. of Radar*, 1996, pp. 480–483.
- [75] C. W. Therrien, *Discrete Random Signals and Statistical Signal Processing*, A. V. Oppenheim, Ed. Prentice-Hall, 1992.
- [76] S. Smith, J. Krolik, and I. Bilik, “Theoretical passive sonar performance of a cluster of UUV towed line arrays employing orientation diversity,” in *OCEANS*, Oct. 2007, pp. 1–7.

- [77] H. Messer, “The potential performance gain in using spectral information in passive detection/localization of wideband sources,” *IEEE Trans. Signal Process.*, vol. 43, no. 12, pp. 2964–2974, 1995.
- [78] H. Cox, “Spatial correlation in arbitrary noise fields with applications to ambient sea noise,” *J. Acoust. Soc. Am.*, vol. 54, pp. 1289–1301, 1973b.
- [79] B. D. Carlson, E. D. Evans, and S. L. Wilson, “Search radar detection and track with the hough transform. iii. detection performance with binary integration,” *IEEE Trans. Aerosp. Electron. Syst.*, vol. 30, pp. 116–125, 1994.
- [80] R. Urick, “Ambient noise in the sea,” Catholic Univ. of America, Tech. Rep., 1984.
- [81] R. Burden and J. Faires, *Numerical Analysis*. Brooks/Cole, 2001.
- [82] A. Weiss and B. Friedlander, “On the Cramér-Rao bound for direction finding of correlated signals,” *IEEE Trans. Signal Process.*, vol. 41, no. 1, pp. 495–499, 1993.
- [83] A. Jakoby, J. Goldberg, and H. Messer, “Source localization in shallow water in the presence of sensor location uncertainty,” *IEEE J. Ocean. Eng.*, vol. 25, no. 3, pp. 331–336, July 2000.
- [84] Y. Abramovich, N. Spencer, and A. Gorokhov, “DOA estimation for noninteger linear antenna arrays with more uncorrelated sources than sensors,” *IEEE Trans. Signal Process.*, vol. 48, no. 4, pp. 943–955, 2000.
- [85] —, “Detection-estimation of more uncorrelated gaussian sources than sensors in nonuniform linear antenna arrays. II. Partially augmentable arrays,” *IEEE Trans. Signal Process.*, vol. 51, no. 6, pp. 1492–1507, 2003.
- [86] E. Tuncer, T. K. Yasar, and B. Friedlander, *Classical and Modern Direction-of-Arrival Estimation*. Academic Press, 2009, ch. Narrowband and Wideband DOA Estimation for Uniform and Nonuniform Linear Arrays, pp. 125–160.
- [87] D. Johnson and D. Dudgeon, *Array signal processing: concepts and techniques*. Simon & Schuster, 1992.
- [88] A. Manikas and N. Dowlut, “The use of differential geometry in array signal processing,” *Kybernetes*, vol. 27, pp. 251–263, 1998.
- [89] A. Moffet, “Minimum-redundancy linear arrays,” *IEEE Trans. Antennas Propag.*, vol. 16, no. 2, pp. 172–175, Mar. 1968.
- [90] V. Murino, A. Trucco, and C. Regazzoni, “Synthesis of unequally spaced arrays by simulated annealing,” *IEEE Trans. Signal Process.*, vol. 44, no. 1, pp. 119–122, 1996.

- [91] S. Pillai and F. Haber, “Statistical analysis of a high resolution spatial spectrum estimator utilizing an augmented covariance matrix,” *IEEE Trans. Acoust., Speech, Signal Process.*, vol. 35, no. 11, pp. 1517–1523, Nov. 1987.
- [92] P. Vaidyanathan and P. Pal, “Sparse sensing with coprime arrays,” in *Conf. Rec. of the Forty Fourth Asilomar Conf. on Signals, Systems and Computers (ASILOMAR)*, Nov. 2010, pp. 1405–1409.
- [93] —, “Theory of sparse coprime sensing in multiple dimensions,” *IEEE Trans. Signal Process.*, vol. 59, no. 8, pp. 3592–3608, Aug. 2011.
- [94] R. Schmidt, “Multiple emitter location and signal parameter estimation,” *IEEE Trans. Antennas Propag.*, vol. 34, no. 3, pp. 276–280, Mar. 1986.
- [95] C. Proukakakis and A. Manikas, “Study of ambiguities of linear arrays,” in *IEEE Inter. Conf. on Acoustics, Speech, and Signal Processing*, vol. 4. IEEE, 1994, pp. 549–552.
- [96] Y. Abramovich, N. Spencer, and A. Gorokhov, “Resolving manifold ambiguities in direction-of-arrival estimation for nonuniform linear antenna arrays,” *IEEE Trans. Signal Process.*, vol. 47, no. 10, pp. 2629–2643, 1999.
- [97] Y. Abramovich, D. Gray, A. Gorokhov, and N. Spencer, “Positive-definite Toeplitz completion in DOA estimation for nonuniform linear antenna arrays. I. Fully augmentable arrays,” *IEEE Trans. Signal Process.*, vol. 46, no. 9, pp. 2458–2471, 1998.
- [98] W.-K. Ma, T.-H. Hsieh, and C.-Y. Chi, “DOA estimation of quasi-stationary signals via Khatri-Rao subspace,” in *IEEE Int. Conf. Acoustics, Speech and Signal Processing*, 2009, pp. 2165–2168.
- [99] P. Pal and P. Vaidyanathan, “Nested arrays: A novel approach to array processing with enhanced degrees of freedom,” *IEEE Trans. Signal Process.*, vol. 58, no. 8, pp. 4167–4181, 2010.
- [100] J. Fuchs, “Extension of the Pisarenko method to sparse linear arrays,” *IEEE Trans. Signal Process.*, vol. 45, no. 10, pp. 2413–2421, 1997.
- [101] Y. Abramovich, N. Spencer, and A. Gorokhov, “Detection-estimation of more uncorrelated gaussian sources than sensors in nonuniform linear antenna arrays. I. Fully augmentable arrays,” *IEEE Trans. Signal Process.*, vol. 49, no. 5, pp. 959–971, 2001.
- [102] M. Wax and T. Kailath, “Detection of signals by information theoretic criteria,” *IEEE Trans. Acoust., Speech, Signal Process.*, vol. 33, no. 2, pp. 387–392, Apr. 1985.

- [103] M. RübSamen and A. Gershman, “Sparse array design for azimuthal direction-of-arrival estimation,” *IEEE Trans. Signal Process.*, vol. 59, no. 99, pp. 5957–5969, 2011.
- [104] M. Doron and E. Doron, “Wavefield modeling and array processing I. spatial sampling,” *IEEE Trans. Signal Process.*, vol. 42, no. 10, pp. 2549–2559, Oct. 1994.
- [105] F. Belloni, A. Richter, and V. Koivunen, “DoA estimation via manifold separation for arbitrary array structures,” *IEEE Trans. Signal Process.*, vol. 55, no. 10, pp. 4800–4810, Oct. 2007.
- [106] M. RübSamen and A. Gershman, “Direction-of-arrival estimation for nonuniform sensor arrays: from manifold separation to Fourier domain MUSIC methods,” *IEEE Trans. Signal Process.*, vol. 57, no. 2, pp. 588–599, 2009.
- [107] A. Manikas and C. Proukakis, “Modeling and estimation of ambiguities in linear arrays,” *IEEE Trans. Signal Process.*, vol. 46, no. 8, pp. 2166–2179, 1998.
- [108] A. Manikas, *Differential Geometry in Array Processing*. Imperial College Press, 2004.
- [109] D. B. Ward and G. Elko, “Mixed nearfield/farfield beamforming: a new technique for speech acquisition in a reverberant environment,” in *IEEE ASSP Workshop on Applications Signal Processing to Audio and Acoustics*, 1997, pp. 1–4.
- [110] J. Liang and D. Liu, “Passive localization of mixed near-field and far-field sources using two-stage MUSIC algorithm,” *IEEE Trans. Signal Process.*, vol. 58, no. 1, pp. 108–120, Jan. 2010.
- [111] B. Wang, Y. Zhao, and J. Liu, “Mixed-order MUSIC algorithm for localization of far-field and near-field sources,” *IEEE Signal Process. Lett.*, vol. 20, no. 4, pp. 311–314, 2013.
- [112] L. Scharf and D. Tufts, “Rank reduction for modeling stationary signals,” *IEEE Trans. Acoust., Speech, Signal Process.*, vol. 35, no. 3, pp. 350–355, 1987.
- [113] O. Frost, “An algorithm for linearly constrained adaptive array processing,” in *Proc. IEEE*, vol. 60, no. 8, Aug 1972, pp. 926–935.
- [114] A. Haimovich, “The eigencanceler: adaptive radar by eigenanalysis methods,” *IEEE Trans. Aerosp. Electron. Syst.*, vol. 32, no. 2, pp. 532–542, 1996.
- [115] J. S. Goldstein and I. S. Reed, “Reduced-rank adaptive filtering,” *IEEE Trans. Signal Process.*, vol. 45, no. 2, pp. 492–496, 1997.

- [116] H. Cox, “Adaptive beamforming in non-stationary environments,” in *Conf. Rec. 36th Asilomar Conf. Signals, Systems and Computers*, vol. 1, 2002, pp. 431–438.
- [117] X. Mestre and M. Lagunas, “Finite sample size effect on minimum variance beamformers: optimum diagonal loading factor for large arrays,” *IEEE Trans. Signal Process.*, vol. 54, no. 1, pp. 69–82, 2006.
- [118] M. Pajovic, J. Preisig, and A. Baggeroer, “Analytical characterization of the mpdr-based power estimators in snapshot scarce regime,” in *IEEE Statistical Signal Processing Workshop (SSP)*, 2012, pp. 808–811.
- [119] M. Ishiguro, “Minimum redundancy linear arrays for a large number of antennas,” *Radio Science*, vol. 15, no. 6, pp. 1163–1170, 1980.
- [120] L. L. Scharf, *Statistical Signal Processing*, R. Roberts, Ed. Addison-Wesley, 1991.
- [121] J. Odom and J. Krolik, “Microphone array beamforming with near-field correlated sources,” in *Proc. of ASA*, May 2009.
- [122] —, “Time-varying spatial spectrum estimation using a maneuverable sonar array,” in *Proc. of ASA.*, Oct. 2011.
- [123] —, “Time-varying array shape estimation by mapping acoustic field directionality,” in *OCEANS*, Oct. 2012.
- [124] —, “Broadband field directionality mapping with spatially-aliased arrays,” in *IEEE 7th Sensor Array and Multichannel Signal Processing Workshop (SAM)*, 2012, pp. 449–452.
- [125] —, “Heading and hydrophone data fusion for towed array shape estimation,” in *Proc. Meeting Acoustics*, vol. 19, no. 1. ASA, Jun. 2013.
- [126] —, “Adaptive beamforming with augmentable arrays in non-stationary environments,” in *IEEE Workshop on Computational Advances in Multi-Sensor Adaptive Processing (IEEE CAMSAP)*, Dec. 2013.
- [127] —, “Near-field beamforming with augmentable non-uniform arrays for far-field interference suppression,” in *Proc. of ASA*, Dec. 2013.
- [128] J. Odom, J. Krolik, and J. Rogers, “Maximum-likelihood spatial spectrum estimation in dynamic environments with a short maneuverable array,” *J. Acoust. Soc. Am.*, vol. 133, pp. 311–322, 2013.
- [129] J. Odom and J. Krolik, “Passive towed array shape estimation using heading and acoustic data,” *IEEE J. Ocean. Eng.*, Sep. 2013, submitted.

# Biography

Jonathan Lawrence Odom was born on Feb. 23rd, 1987 in Hickory, NC. He received the B.S.E degree from Duke University during 2009 in Durham, NC, majoring in electrical and computer engineering and computer science with a minor in religion and graduating magna cum laude as well as with distinction. He received the M.S. and Ph.D. degrees in electrical and computer engineering, in 2011 and 2013 respectively, from Duke University. While at Duke, he received the Braxton-Craven Scholarship as well as the Pratt-Gardner and James B. Duke fellowships. From 2009 to 2013, he was a Research Assistant in the Sensor Array and Multipath Lab at Duke under the supervision of Jeffrey Krolik. He spent the summer of 2012 at The Johns Hopkins Applied Physics Laboratory with Bruce Newhall. In 2014, he will be an Adjunct Assistant Professor at Duke. After finishing his time at Duke, he will join the research faculty at Georgia Tech Research Institute. His research interests include sonar, radar, array signal processing and statistical signal processing.

While at Duke, he published the following conference papers: [121–127]. The field directionality mapping work in Chapter 4 has been published in the *Journal of the Acoustical Society of America* [128], and the array shape estimation work has been submitted to *IEEE Journal of Oceanic Engineering* [129]. The work in Chapter 5 will be submitted to *IEEE Transactions on Signal Processing*.